

Thermal and magnetoelastic effects in magnetic tunnel junction

von der Fakultät für Mathematik und Physik
**der Gottfried Wilhelm Leibniz Universität
Hannover**

zur Erlangung des Grades

Doktor der Naturwissenschaften

Dr. rer. nat.

genehmigte Dissertation

von

Hangfu Yang

geboren am 07.01.1986 in Taizhou

2018

Keywords: spin caloritronics; spin straintronics; MTJ; femtosecond laser pulse

Referent: PD Dr. rer. nat. Hans W. Schumacher

Korreferent: Prof. Dr. Michael Oestreich

Gutachter: Dr.-Ing. Mark Bieler

Tag der Disputation: 27.08.2018

Abstract

Heat dissipation in spintronic devices is currently a limiting factor for their further miniaturization, spurring scientists on seeking for more energy friendly mechanisms to manipulate spin. In this work, two new approaches for stimulating local spin or magnetization in a magnetic tunnel junction (MTJ), being a very important and industrially relevant device, are presented. The studies are based on thermal and magnetoelastic effects on the local spin of MTJs with the stimulus of heat pulses and acoustic pulses generated by femtosecond laser pulses.

The information of the local spin, being included in the spin dependent electric conductance or resistance of the MTJ, is studied by time resolved and static resistance detection methods. Thereby, optically generated temperature and temperature gradient effects on the spin are considered separately. For the study of temperature effects, the temperature dependence of the resistance of the MTJ is employed. The measured resistance and temperature traces reveal that the resultant resistance change after laser excitation mainly results from temperature effects, which is supported by finite element simulations. Still, the local spin is also influenced by a temperature gradient effect. Based on the intrinsic magnetic properties of the MTJ, the temperature and temperature gradient effects can even be separated.

The thermal effect on the magnetization can only be observed when the laser beam is focused directly on the MTJ, while the magnetization dynamics can be excited by acoustic pulses (surface acoustic waves) when the laser pulse hits the surface several μm away from the MTJ. The excited magnetization dynamics due to the magnetoelastic effect strongly depends on the laser heating position and applied magnetic field. Comparing the acoustic wave induced precession frequencies with precession induced by charge currents and with micromagnetic simulations, we identify spatially non-uniform magnetization modes localized close the edge regions as being responsible for the optically induced magnetization dynamics. Two acoustic pulses created by the laser even allow us to coherently control the magnetization precession.

The study presented in the thesis shows that the manipulation of spins can be achieved with femtosecond laser pulse heating in a straightforward way. Additionally,

the techniques employed in the study enable the use of MTJs for novel applications such as temperature and strain sensors with a large dynamic range.

Zusammenfassung

Die Hitzeentwicklung in Spintronik-Bauelementen beeinträchtigt heutzutage deren weitere Miniaturisierung. Dadurch widmen sich viele Wissenschaftler der Suche nach energiefreundlicheren Mechanismen um Spin zu manipulieren. In dieser Arbeit werden zwei neue Ansätze vorgestellt, um lokalen Spin oder Magnetisierung in magnetischen Tunnelbarrieren (MTJ) anzuregen. Die Untersuchungen beruhen auf den thermischen und magnetoelastischen Auswirkungen auf den lokalen Spin der MTJ, durch die Anregung von Wärmeimpulsen und Schallimpulsen, die durch Femtosekundenlaser induziert werden.

Die Information des lokalen Spins, die in der spinabhängigen elektrischen Leitfähigkeit beziehungsweise im Widerstand der MTJ enthalten ist, wird durch zeitaufgelöste und statische Widerstandsmessungen bestimmt. Dabei werden Effekte aufgrund von optisch erzeugten Temperatur und Temperaturgradienten getrennt betrachtet. Die Untersuchung von Temperatureffekten basiert auf dem temperaturabhängigen Widerstand der MTJ. Die gemessenen Widerstands- und Temperaturkurven zeigen, dass die Widerstandsänderung nach der Laseranregung hauptsächlich durch einen Temperatureffekt verursacht wird. Finite-Elemente-Simulationen verifizieren dieses Ergebnis. Dennoch wird der Lokale Spin auch vom Temperaturgradienten beeinflusst. Basierend auf den intrinsischen magnetischen Eigenschaften der MTJ, können die Temperatur- und Temperaturgradient-Effekte sogar voneinander getrennt werden.

Der thermische Effekt auf die Magnetisierung kann nur beobachtet werden, wenn der Laserstrahl direkt auf den MTJ fokussiert wird. Im Gegensatz kann die Magnetisierungsdynamik durch die Schallimpulse (akustische Oberflächenwellen) angeregt werden, auch wenn der Laserimpuls mit einem Abstand zu den MTJ auf die Oberfläche trifft. Die aufgrund des magnetoelastischen Effekts angeregte Magnetisierungsdynamik hängt stark von der Position des Lasers und dem angelegten Magnetfeld ab. Beim Vergleich von Präzessionsfrequenzen, die durch akustische Wellen induziert werden, mit einer durch Ladungsströmen induzierten Präzession sowie mit mikromagnetischen Simulationen, wird eine räumlich inhomogene Magnetisierungsmode identifiziert, die nahe den Randregionen lokalisiert ist und für die optisch induzierte Magnetisierungsdynamik verantwortlich ist. Zwei durch den Laser erzeugte akustische Impulse ermöglichen sogar

eine kohärente Steuerung der Magnetisierungspräzession.

Die vorliegende Arbeit zeigt, dass Heizen durch Femtosekunden-Laserpulse einen einfachen Weg zur Spinmanipulation darstellt. Außerdem ermöglichen die hier vorgestellten Techniken die Verwendung von MTJ für neuartige Anwendungen wie zum Beispiel als Temperatur- und Dehnungssensoren mit einem großen Dynamikbereich.

Contents

1	Introduction	1
2	Background	5
2.1	Magnetic tunnel junction (MTJ)	5
2.1.1	Tunneling magnetoresistance	5
2.1.2	Voltage and temperature dependencies of tunnel resistance . . .	8
2.1.3	Magnetization reversal curve	11
2.2	Magnetization dynamics in MTJs	13
2.2.1	Landau-Lifshitz-Gilbert equation	13
2.2.2	Charge spin transfer torque	14
2.2.3	Thermal spin transfer torque	16
2.2.4	Magnetoelastic effects	16
2.2.5	Thermal effects	18
2.3	Laser excitation	18
2.3.1	Optically induced heat currents in MTJs	18
2.3.2	Optically induced surface acoustic waves	20
3	Experimental details	23
3.1	Samples	23
3.2	All optical pump-probe setup.	24
3.2.1	Time domain thermoreflectance method	24
3.2.2	Beam distortion detection technique for surface acoustic waves .	28
3.3	Electrical resistance measurement setup	30
3.3.1	Static resistance measurement	31
3.3.2	Time resolved resistance measurement	32
4	Thermal effects in MTJs induced by femtosecond laser pulse excitation	35
4.1	Introduction	35
4.2	Experimental basics	36
4.3	Voltage and temperature dependence of tunnel resistance	37
4.4	Time-integrated and time-resolved temperature measurements in MTJs	38

4.5	Heat transport simulations	42
4.5.1	Time and spatially resolved temperature variations	42
4.5.2	Time resolved spatial temperature gradients	44
4.6	Temperature gradient effects	47
4.7	Conclusions	52
5	The MTJ as a temperature sensor	53
5.1	Introduction	53
5.2	Experimental basics	54
5.3	Temperature sensor based on the tunnel resistance	55
5.4	Temperature sensor based on the coercivity of the free layer	56
5.5	Temperature sensor based on the coercivity of the synthetic antiferromagnet	59
5.6	Comparison of the three methods and conclusions	62
6	Magnetoelastic effects in MTJs induced by femtosecond laser pulse excitation	65
6.1	Introduction	65
6.2	Experimental basics	66
6.3	Surface acoustic wave induced magnetization dynamics in MTJ	68
6.3.1	Position dependent measurement	70
6.3.2	Magnetic field dependent measurement	72
6.3.3	Laser power dependent measurement	74
6.4	Magnetization dynamics driven by charge spin transfer torque	76
6.5	Simulation of magnetization dynamics driven by surface acoustic waves	77
6.6	Coherent control of SAW induced magnetization dynamics	78
6.7	Conclusions	79
7	Summary and outlook	81
	Bibliography	85
	Own publications	109
	Acknowledges	111
	Curriculum vitae	112

1 Introduction

Intense studies of spintronics have been triggered by the discovery of the giant magnetoresistance (GMR) effect thirty years ago. Owing to this finding, Albert Fert and Peter Grünberg were awarded the 2007 Nobel prize in physics [1, 2]. The GMR effect refers to a large resistance difference in exchange coupled multilayers composed of alternating ferromagnetic and non-magnetic conductive layers when the magnetizations of the ferromagnetic layers possess a parallel (low resistance: P state) and antiparallel (high resistance: AP state) alignment. The resistance difference is greatly enhanced in a magnetic tunnel junction (MTJ) when a thin insulator layer is used between two ferromagnetic layers. The effect is referred to as tunneling magnetoresistance (TMR) [3]. The resistance switching in the MTJ with the reversal of the magnetic state achieved by manipulating the spin or magnetization of the magnetic layer is used in non-volatile magnetic random access memory (MRAM), where high resistance means ‘1’ and low resistance means ‘0’. The modern data storage requires not only a high density of bit cells but also a high writing speed, which depends on how fast one can reverse the magnetization. Nowadays, magnetization switching can be realized by a magnetic field, or by a charge current induced spin transfer torque (STT) [4, 5]. Recently, a significant achievement has been reported that the magnetization of an MTJ with a size of 10 nm is switched by a current of $7.5 \mu\text{A}$ within 10 ns. However, such a high current density leads to significant energy waste and also might damage the MTJ cell. Therefore, it is necessary to investigate energy friendly methods for fast magnetization switching.

The manipulation of spin or magnetization can be achieved by different physical effects, such as, electrons, heat flux, THz radiation, as well as phonons [6]. The interaction of heat with the spins created a new active research area called ‘spin caloritronics’, boosted by the discovery of the spin-Seebeck effect by Uchida in 2008 [7]. The development of this area gives a new choice for magnetization manipulation with heat currents. The relevant effect is the thermal spin transfer torque (T-STT). In the metallic spin valve, T-STT results from the spin-dependent Seebeck effect [8]. The accumulated spins at the interface of a magnetic layer diffuse through a thin metallic separation layer due to the temperature gradient in the layer, exerting a torque on the second magnetic layer. In an MTJ, the T-STT effect also refers to the Seebeck spin tunneling [9]. A spin accumulation is created at the interface of the magnetic layer due to a flow of

heat current through the insulator layer. Such T-STT is believed to be more efficient than charge induced STT for manipulating magnetization [10]. The study of T-STT has a great significance for applications in spintronics and may also boost the study of nanoscale heat transport.

Meanwhile, the combination of strain with spintronics may generate the research area ‘spin straintronics’. Some pioneering work found that static strain has a great influence on the spin dependent electric transport [11]. Strain sensors based on the GMR and TMR effect have recently been developed. They are based on the magnetoelastic effect, i.e., the interaction between the local spin or magnetization and strain, which has been known for a long time. But the manipulation of magnetization on the nanosecond and picosecond time scale has only been achieved recently thanks to optically generated short acoustic pulses [12]. Such pulses can be used to excite magnetization dynamics in magnetic thin films, and even coherent control of magnetization dynamics has been realized. Thus, the study of the interaction between acoustic pulses and spin may give us another choice for fast magnetization manipulation.

This thesis focuses on the active fields of spin caloritronics and spin straintronics with the MTJ (CoFeB/MgO/CoFeB), as important spintronic device. The center of attention in this work lies on magnetization dynamic and magnetization reversal in an MTJ excited with femtosecond laser generated heat pulses and acoustic pulses (surface acoustic waves, SAW). To achieve this goal, a comprehensive experimental system is designed and built in the lab. This system fulfills the abilities of optically generation of heat current and SAW, temperature characterization, excitation and control of magnetization dynamics, and detection of magnetization dynamics.

As shown in Fig. 1.1, the main results of this thesis are:

- Measurement of average temperature and temperature transients in an MTJ induced by the laser pulse generated heat pulse.
- Excitation and coherent control of the magnetization dynamics in an MTJ induced by the laser pulse generated SAWs.

The outline of this thesis is organized as following:

In chapter 2, we introduce the background and motivation of our work. It starts with the description and discussion of the basic properties of the MTJs, including TMR effect and the dependence of tunnel resistance on the voltage and temperature. Subsequently, a static Stoner-Wohlfarth model is used to address the coherent magnetization rotation of single-domain particles which are subjected to an external magnetic field. In the second section, the discussion is extended to the fast magnetization dynamics based

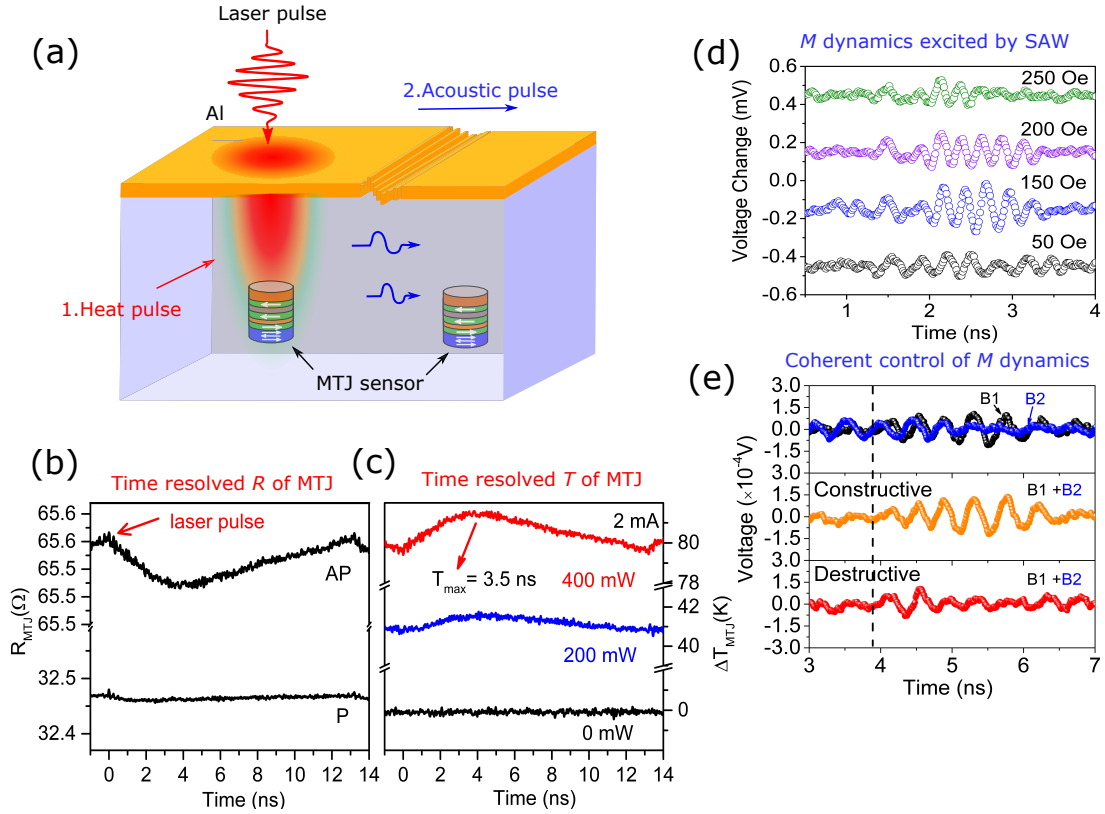


Figure 1.1: Main results. (a) A schematic viewgraph of the interaction of the MTJ with the laser pulses. The study contains two relevant excitation source: heat pulses and acoustic pulses. (b) The measured time resolved resistance traces of MTJs for the case in which heat transport from the surface to the MTJ takes place after the laser pulses. A large difference has been found when the MTJ is the AP and P states, which is due to the temperature dependence of resistance of the MTJ in the two states. (c) The time resolved temperature of the MTJ for different laser heating powers converted from (b). (d) Magnetization dynamics traces at various external magnetic fields excited by the SAWs. (e) Coherent control of magnetization dynamics with two laser pulses.

on Landau-Lifshitz-Gilbert equation, various driving forces (like STT and SAW) are introduced in the equation. In the third section, the mechanism of laser generated heat currents and SAWs is presented.

In chapter 3, the experimental setups and measurement methods are described. In the first section, we introduce details of the composition of the MTJ samples. In the second section, the purely optical pump and probe setups for detection of surface temperature change (TDTR method) and measurement of SAWs are presented. In the third section, we describe the electric detection techniques based on spin dependent resistance for measuring static magnetization reversal and magnetization dynamics induced with different driving forces.

In chapter 4, the work focuses on the thermal effect on the MTJ. In the first section, we provide a new scheme for the time resolved measurement of local temperature of the MTJ after laser pulse heating. Based on heat diffusion mechanism, the thermal transport through the layers of the MTJ is also simulated with a COMSOL simulation and the temperature and the temperature gradient are extracted from the simulation. In the next section, the temperature gradient effect or heat current effect on the magnetization reversal of the MTJ is presented and discussed.

In chapter 5, the MTJ is used as a temperature sensor. The sensor is based on three intrinsic properties of MTJs : tunnel resistance, coercivity of the free layer and coercivity of the synthetic antiferromagnet (SyAF). The temperature dependence of the MTJ is calibrated with an electric heating stage. After calibration, the average temperature of the MTJ for various laser heating powers can be determined with all three different methods.

In chapter 6, we investigate SAW induced magnetization dynamics of MTJs with laser pulse excitation. A systematic study of the magnetization dynamics and its dependence on the magnetic field, laser heating position and laser power is presented. We experimentally clarify the magnetization dynamics mode driven by the SAW with a comparison of the mode driven by charge induced STT, which is supported by a micromagnetic simulation. At the end of this chapter, the coherent control of excited magnetization dynamics with two laser pulses is presented.

2 Background

2.1 Magnetic tunnel junction (MTJ)

Magnetic tunnel junctions (MTJ) are one of the fundamental devices in spintronics. Since the realization of the first MTJ operating at room temperature in 1995 [3], it has received a great deal of attention from industry and fundamental research due to its high tunneling magnetoresistance (TMR). At that time, the reported TMR of an MTJ with AlO_x barrier was about 12 %, which was a great breakthrough compared with GMR. The most important step was made when MgO was used as a tunnel barrier. The obtained TMR value could be increased up to 600 % [13]. Nowadays, MTJs are the basic components of magnetic memory called STT-MRAM (spin transfer torque magnetic random access memory), which has already been put onto the market [14,15]. Also profiting from high TMR, MTJs have been widely used in the field of sensors.

2.1.1 Tunneling magnetoresistance

A sandwich-structured MTJ consists of two ferromagnetic layers (FM) separated by a thin nonmagnetic insulator (NI) barrier. The NI layer is typically a few atomic layers thick, so that electrons can tunnel through the barrier. The tunneling process is spin dependent, the conductance of electrons is dependent on its spin polarity and the magnetic orientation of the two ferromagnetic electrodes. An MTJ has a low resistance when the magnetizations of FM1 and FM2 are parallel (P state) and a high resistance when the magnetizations are antiparallel (AP state). The phenomenon is known as TMR effect.

In 1975, Julliere proposed a simple two current model to describe this effect [16]. In his model, the total current (I) tunneling through the MTJ is the sum of two independent current channels ($I^\uparrow + I^\downarrow$) of spin up (\uparrow : majority spin) and spin down (\downarrow : minority spin). As shown in Fig. 2.1, when the magnetic orientations of the two electrodes FM1 and FM2 are in the P state, electrons in both spin channels can easily tunnel through the barrier, resulting in a large electric conductance (G_P). While the MTJ is in the AP state, the FM2 layer blocks both current channels, resulting in

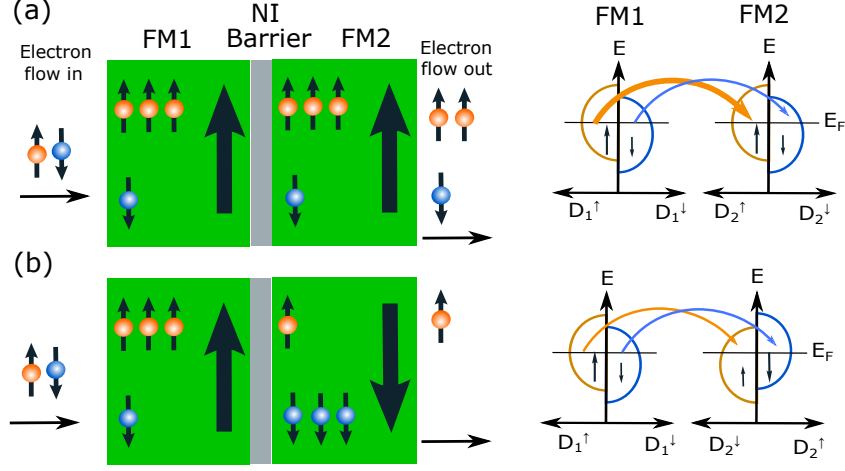


Figure 2.1: A schematic of the two current model for spin dependent transport in MTJs for (a) the P state and (b) the AP state. Electrons can only tunnel to the sub-band of the same spin direction. With the same bias voltage, more electrons can tunnel through the barrier in the P state than in the AP state (left side of the figure). The conductance of the MTJ is proportional to the product of the electron density of states (DOS) of the FM1 and FM2 layers, see right side of the figure.

a small electric conductance (G_{AP}). In Julliere's model, the interface contribution is not taken into account. The conductance is simply proportional to the product of the electron density of state (DOS) of the two electrodes and can be written as

$$G_P \propto D_1^\uparrow D_2^\uparrow + D_1^\downarrow D_2^\downarrow, \quad (2.1)$$

$$G_{AP} \propto D_1^\uparrow D_2^\downarrow + D_1^\downarrow D_2^\uparrow, \quad (2.2)$$

where D^\uparrow and D^\downarrow are the DOS near the Fermi energy level E_F for the majority spin (up) and minority spin (down), respectively. Therefore, we can calculate the TMR ratio:

$$\text{TMR} = \frac{G_P - G_{AP}}{G_{AP}} = \frac{R_{AP} - R_P}{R_P} = \frac{2P_1 P_2}{1 - P_1 P_2}, \quad (2.3)$$

where P_1 and P_2 are the spin polarizations ($P \equiv \frac{D^\uparrow - D^\downarrow}{D^\uparrow + D^\downarrow}$) for FM1 and FM2, respectively.

Julliere's model well explains the tunneling conductance of the MTJ in the AP and P state, where the angle (φ) between the two magnetizations of FM1 and FM2 is 180° or 0° . However, the model can not address the angle dependence of the conductance between 180° and 0° . Additionally, Slonczewski considered the TMR effect quantum mechanically. The interfacial exchange-bias coupling has been taken into account in

his model [17, 18]. The conductance of the MTJ depends linearly on the cosine of the angle of magnetization between the two electrodes, and it is written as

$$G(\varphi) = \frac{1}{2}(G_P + G_{AP}) + \frac{1}{2}(G_P - G_{AP})\cos\varphi. \quad (2.4)$$

This model reproduces the angle dependence of the conductance of MTJs.

Based on Julliere's model, researchers were experimentally seeking for MTJs with high TMR ratio either by using magnetic electrodes with higher spin polarization or by improving fabrication techniques to get a better quality of the MTJ structure. With all the improvements, the maximum TMR value for MTJs with amorphous AlO_x barrier was achieved up to 80 % at room temperature. Besides the development of fabrication techniques, the theoretical investigations were going on to better understand the spin dependent tunneling mechanism, and show also potential ways for the experimental research to enhance the TMR effect in MTJs. In 2001, by replacing the amorphous AlO_x barrier with crystalline MgO, Butler calculated the tunneling conductance of MTJ in a bcc Fe(001)/MgO(001)/Fe(001) trilayer system by using first principle calculations and demonstrated that the tunneling conductance is strongly dependent on the decay rate of the Bloch states in the barrier [19].

As shown in Fig. 2.2, there are a variety of Bloch states with different symmetries in the Fe electrode, referring to different Bloch waves or channels when electrons travel through the barrier. The Bloch states have different decay rates in the barrier, depending on the symmetry of the Bloch states in two electrodes and the symmetry of the barrier. In the P state, Δ_1 symmetry for the majority spin shows a slow decay rate due to the symmetry matching of the Bloch states in the Fe electrode and the symmetry in the barrier, leading to a high conductance in this channel. In contrast, Δ_2 and Δ_5 symmetries have a fast decay in the barrier and make a small contribution to the conductance. However, in the AP state, the decay rates of the Bloch states for the majority spin and the minority spin are all very fast, leading to a low conductance. Therefore, MTJs with a high quality of the MgO barrier can effectively filter the Bloch states which gives rise to high TMR ratios. Such a tunneling process is called coherent tunneling. In contrast, in MTJs with AlO_x barrier, the conductance is dependent on the spin dependent diffusion. All the Bloch states have the same decay rate in the barrier, leading to a low TMR ratio. In 2004, shortly after crystalline MgO was used as a barrier, the TMR reached a value of up to 200 % at room temperature [20, 21].

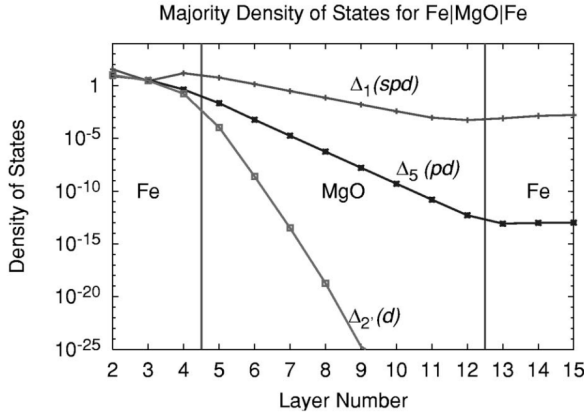


Figure 2.2: Tunneling density of state (DOS) for the majority spin when the Fe(001)/MgO(001)/Fe(001) junction is in the P state. Δ represents different symmetries of Bloch states. The Bloch state with Δ_1 symmetry shows a very slow decay in the MgO barrier. The figure is from reference [19]. ©American Physical Society

2.1.2 Voltage and temperature dependencies of tunnel resistance

The tunnel probability in MTJs is dominated by the DOS of the ferromagnetic electrodes. The energy dependence of the DOS indicates that the conductance also relies on the bias voltage (V) and temperature (T).

Voltage dependence. An applied voltage (V) across the barrier will shift the relative position of the Fermi levels ($E_F \pm eV/2$) between the two magnetic electrodes, leading to a change in the conductance of the MTJ in both AP and P states, according to Eq. 2.1. The height of the barrier can be extracted from fitting Brinkman's formula with the measured current-voltage ($I - V$) curve [22]. Moodera studied the TMR as a function of dc bias voltage at different temperatures [23]. Figure 2.3(a) shows plots of the conductance (dI/dV) versus bias voltage V of a Co/Al₂O₃/Ni₈₀Fe₂₀ junction measured at room temperature (295 K) and low temperature (1 K) [23]. When the bias voltage is larger than 200 mV, the conductance gradually increases in both, AP and P states with the bias voltage. But the conductance in the AP state changes faster than in the P state, which results in a reduction of the TMR ratio. A dip [24] in the curve occurs when a small bias voltage is applied to the MTJ. Such a feature is significant at low temperature and is known as 'zero bias anomaly'.

The widely accepted explanation of such voltage dependence of the conductance was given by the Moodera and Zhang [23, 24]. Their model is based on the DOS of the electrodes and the incoherent tunneling process in the barrier. They attributed the reduction of TMR with voltage to the magnon excited by the 'hot electron' (electrons with excess energy above the Fermi level) at the interface between the magnetic electrode and barrier. In the MTJ, the excited magnon randoms the tunnel electron spins and increases the total conductance in both states. Since the increase of conductance is proportional to the expression $D_1^\uparrow D_2^\uparrow + D_1^\downarrow D_2^\downarrow$ for the AP state and $D_1^\uparrow D_2^\downarrow + D_1^\downarrow D_2^\uparrow$ for

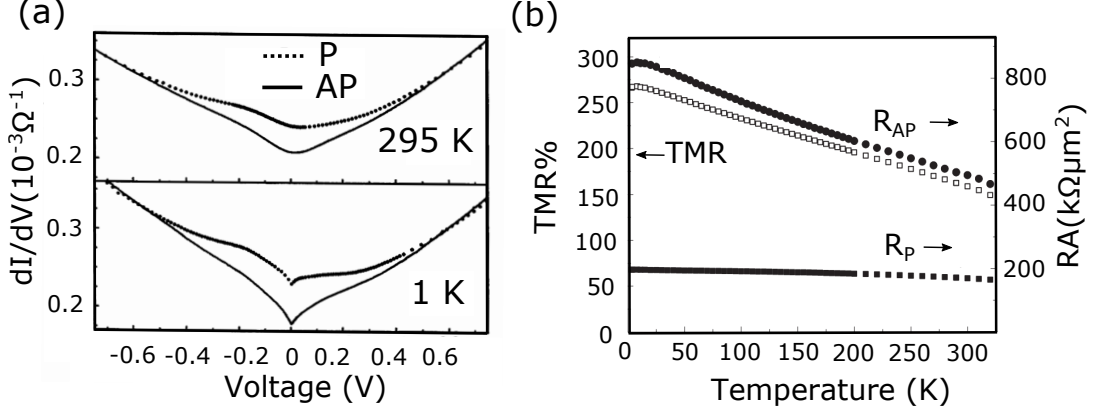


Figure 2.3: (a) Conductance versus bias voltage measured at room temperature and low temperature for a $\text{Co}/\text{Al}_2\text{O}_3/\text{Ni}_{80}\text{Fe}_{20}$ junction. The figure is from reference [23]. ©American Physical Society (b) Temperature dependence of R_{AP} and R_{P} for $\text{Co}_{70}\text{Fe}_{30}/\text{MgO}/\text{Co}_{84}\text{Fe}_{16}$. The figure is taken from reference [20]. ©2004, Springer Nature

the P state [24], the G_{AP} increases faster than the G_{P} , which results in the reduction of the TMR ratio. The model can explain the bias voltage dependence of the conductance including the zero bias anomaly for MTJs with AlO_x barriers and also MgO barriers.

Temperature dependence. The temperature (T) dependence of the conductance is quite different for MTJs with AlO_x barriers and MgO barriers. For the MTJ with AlO_x barriers, G_{P} and G_{AP} show a comparable increase with the temperature. Zhang’s magnon assisted inelastic tunneling model can also explain such temperature dependence of conductance $G(T, V = 0)$ at zero bias V . It is expressed as [24–26]:

$$G_{\text{P}} = G_{\text{P}}(0, 0) \left[1 + \xi Q \frac{2S'}{E_m} k_{\text{B}} T \ln\left(\frac{k_{\text{B}} T}{E_c}\right) \right], \quad (2.5)$$

$$G_{\text{AP}} = G_{\text{AP}}(0, 0) \left[1 + \frac{1}{\xi} Q \frac{2S'}{E_m} k_{\text{B}} T \ln\left(\frac{k_{\text{B}} T}{E_c}\right) \right], \quad (2.6)$$

where $\xi = \frac{2D^{\uparrow}D^{\downarrow}}{(D^{\uparrow})^2 + (D^{\downarrow})^2} = 2/(\frac{1-P}{1+P} + \frac{1+P}{1-P})$ is the ratio of the products of the DOS in the P and AP states (assuming the two electrodes are identical). For typical $\text{Co}_{70}\text{Fe}_{30}$ electrodes with spin polarization $P \approx 0.7$, ξ is about 0.34. Q is the tunneling probability of magnons, S' and k_{B} are the spin parameter and Boltzmann constant, respectively. $E_m = 3k_{\text{B}}T_{\text{C}}/(S' + 1)$ is the energy related to the Curie temperature (T_{C}), and E_c is the magnon cutoff energy which determines the excited number of magnons. The conductance G is proportional to the expression $T \ln T$ for both AP and P states, see Eqs. 2.5 and 2.6, but G_{AP} changes faster than G_{P} , giving rise to the reduction of TMR with the temperature. This model can explain the temperature dependence of

conductance for an MTJ with AlO_x barriers, in which conductances in both states increase with the temperature.

However, the inelastic tunneling model can not address the temperature dependence of the conductance for MgO-based MTJs with a high TMR ratio. In such MTJs, G_P is almost independent of temperature, as shown in Fig. 2.3(b). As mentioned above, the coherent tunneling process dominates the conductance of MTJ with an MgO barrier. Drewello modified Zhang's inelastic tunneling model into a magnon assisted coherent tunneling model by considering magnons for the tunneling process [25]. Taking into account the thermal smearing effect on the tunneling electron energy, he was able to reproduce the temperature dependence of the conductance.

Meanwhile, Shang developed a spin-polarized direct elastic tunneling model following Julliere [16, 27]. They attributed the temperature dependence of conductance to the temperature dependence of the spin polarization between two ferromagnetic electrodes. The conductance is expressed as:

$$G_{P/AP}(T) = G_0(T) \left\{ 1 \pm P(T)^2 \right\} + G_{SI}, \quad (2.7)$$

where $+$ and $-$ correspond to the P and AP states, respectively. $G_0(T) = G_0CT/\sin(CT)$ is the prefactor for the direct elastic tunneling which is dependent on the temperature due to the thermal smearing effect, where G_0 is the conductance at $T = 0$ K and C is a constant. G_{SI} is the conductance from unpolarized electrons, $P(T)$ is the temperature dependent spin polarization for two identical electrodes and it can be written as: $P(T) = P_0(1 - \alpha T^{3/2})$, where P_0 is the spin polarization at 0 K and α is a constant, depending on material properties. In the Eq. 2.7, for the P state, $G_0(T)$ increases with the temperature, leading to a positive contribution to G_P , while $P(T)$ makes an opposite contribution since $P(T)$ decreases with T due to the thermally excited spin waves. The competition of two contributions gives rise to the T -independent behavior of G_P [28, 29]. The large temperature dependence of G_{AP} is due to the sum of two contributions with the same sign. This model well explains the temperature dependence of the TMR for MgO-based MTJs with a high TMR ratio.

Combining the above mentioned models or taking into account other models, the temperature dependence of the TMR can also be explained by several different contributions, like magnons and phonons assisted tunneling [30, 31] or magnon and spin-polarized direct elastic tunneling [32]. The study of the voltage and temperature dependence of the TMR has practical significance, especially for the MTJ based STT-MRAM where a large bias voltage is applied to switch the magnetization. In any case, by using the large temperature dependence of the resistance in the AP state, as shown in Fig. 2.3(b), it is possible to use the MTJ as a temperature sensor.

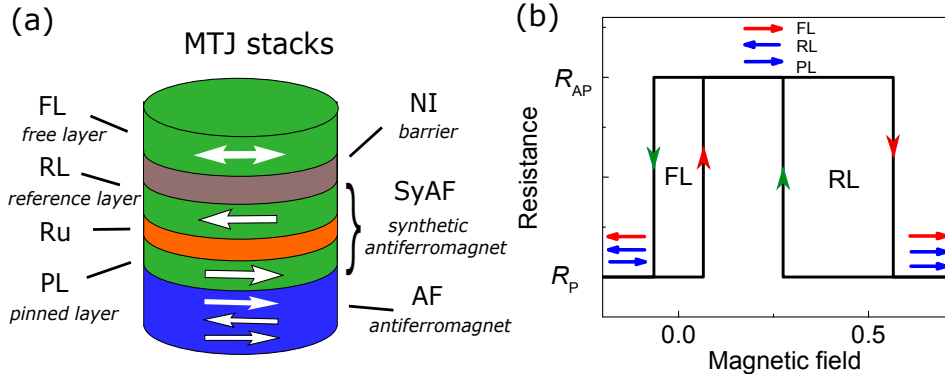


Figure 2.4: (a) Typical MTJ stack. (b) Easy axis magnetoresistance (MR) loop due to magnetization reversal of the FL and the RL layer with uniaxial anisotropy. The minor MR loop results from the FL and the major loop refers to the RL.

2.1.3 Magnetization reversal curve

The basic structure of the MTJ is an FM1/NI/FM2 trilayer system. The magnetization of an FM layer has a preferential alignment direction which is called easy axis arising from the shape and magnetocrystalline uniaxial anisotropy. The external magnetic field needed for a magnetization reversal along the easy axis is called the coercivity (H_C). Since the coercivity is different for FM1 and FM2, one can rotate the magnetization orientations of the two layers with an external magnetic field and let them align parallel or antiparallel. The corresponding resistance as a function of magnetic field is called magnetoresistance (MR) loop, see Fig. 2.4(b). Usually FM1 with a small coercivity is referred to as free layer (FL) and FM2 refers to as a reference layer (RL) with a high coercivity.

In the trilayer system, the FL is not completely free since the stray field from the RL acts on the magnetization of the FL. To compensate this bias field, an artificial synthetic antiferromagnet (SyAF) replaces the RL in the system, as shown in Fig. 2.4(a). The SyAF is made of three layers, two ferromagnetic layers (the reference layer (RL) and the pinned layer (PL)) separated by a non-magnetic metal layer (NM: usually Ru). RL and PL have an inter-layer exchange coupling, so called RKKY coupling [33]. The coupling oscillates between ferromagnetic and antiferromagnetic with the thickness of NM. With a proper thickness of the NM, RL and PL have a strong antiferromagnetic coupling, so that no stray field from the SyAF can influence the FL.

In a practical application, it is better to have a FL in which the magnetization can be easily switched with a small magnetic field, and in which the RL shows no sensitivity to the external magnetic field. Therefore, the anisotropy of the RL needs

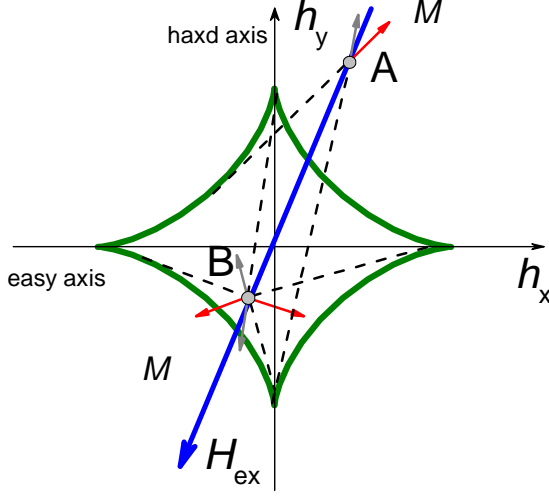


Figure 2.5: The Stoner-Wohlfarth astroid. When the applied magnetic field H_{ex} sweeps from the right to the left (blue arrow), the magnetization orientation (red arrows) of the particle for each magnetic field value (A and B are representative values of H_{ex} being applied outside and inside of the astroid) can be extracted from the astroid.

to be enhanced which is achieved by using an additional antiferromagnet (AF) layer. The PL is exchange coupled to the AF, leading to a large bias field (several 10^3 Oe) of the PL [34]. The direction of the bias field can be defined during the preparation by applying an external magnetic field. Therefore, in most cases, the FL and RL have a large difference in coercivities and only the magnetization of the FL is switchable with a reasonable small magnetic field amplitude. Figure 2.4(b) shows the magnetization switching of the FL by a small magnetic field (minor MR loop). Further increasing the magnetic field, the magnetization of the RL can also be switched (major loop).

The Stoner-Wohlfarth model is one of the simplest models for the description of the switching behavior for an ideal single domain magnetic particle with in-plane uniaxial anisotropy [35, 36]. The magnetic orientation of the particle is determined by minimizing the total energy of the system including Zeeman energy (applied external magnetic field) and magnetic anisotropy energy. The magnetization reversal of the particle characterized by the model is called Stoner-Wohlfarth (SW) astroid, as shown in Fig. 2.5. Mathematically the astroid is calculated as:

$$h_x^{2/3} + h_y^{2/3} = 1, \quad (2.8)$$

where h_x and h_y refer to as the easy and hard axis components of the applied external magnetic field H_{ex} which is scaled to the anisotropy field H_K . So, $h_x = \frac{H_{\text{ex}} \cos \theta}{H_K}$ and $h_y = \frac{H_{\text{ex}} \sin \theta}{H_K}$ and $H_K = \frac{2K_u}{\mu_0 M_s}$, where K_u is the uniaxial anisotropy constant, μ_0 is the vacuum permeability and M_s is the saturation magnetization. The magnetization orientation of the particle in a certain magnetic field can be easily extracted from the astroid by making tangents to the astroid that go through H_{ex} . The magnetization aligns along one of the tangents. For example, when an applied magnetic field is located out of the astroid, such as point A in Fig. 2.5, one can make two tangents to

the astroid, as indicated by the dashed lines. Only the one which is close to the easy axis is stable for the magnetization. So the magnetization aligns along the tangent (dashed line) and towards H_{ex} , as indicated by the red arrow at point A. When the magnetic field is applied inside of the astroid (point B), we can make four tangents to the astroid. Here two of them, which are closed to the easy axis, are stable. In this case, the actual magnetization orientation is determined by the sweeping direction of the field. When the field is swept from the first quadrant to the third quadrant, the red arrow pointing to the right is stable and vice versa.

Note that when the switching of the magnetization is achieved by a sub-nanosecond field pulse or current pulse [37], the Stoner-Wohlfarth model is not valid because the magnetization reversal is dominated by the magnetization precession and the astroid needs to be modified accordingly [38]. But for the case where the magnetic field changes slowly enough so that the magnetization is nearly stable before the magnetic field is changed, this model can well address such quasi-static magnetization reversal behavior.

2.2 Magnetization dynamics in MTJs

A large effort has been made into seeking methods to manipulate magnetization faster, more efficiently and less energy consuming in the last two decades. The studies of magnetization dynamics have moved from the quasi-static regime (above nanoseconds) to the fast (a few picoseconds to several nanoseconds) or even ultrafast (femtoseconds to a few picoseconds) time regime [39]. A variety of excitation sources including field pulse, current pulse, phonon pulse and laser pulse have been used to excite the magnetization dynamics in magnetic thin films, spin valves, magnetic nanodots, domain walls and MTJs.

2.2.1 Landau-Lifshitz-Gilbert equation

Similar to the Stoner-Wohlfarth model, the magnetization dynamics of the magnetic layer can be expressed by a macrospin model known as Landau-Lifshitz-Gilbert (LLG) equation [40]:

$$\frac{\partial M}{\partial t} = \gamma_0 M \times H_{\text{eff}} - \frac{\alpha}{M_s} \left(\frac{\partial M}{\partial t} \times M \right), \quad (2.9)$$

where M is the total dipole moment per unit volume, γ_0 is the gyromagnetic factor and α is the phenomenological damping constant.

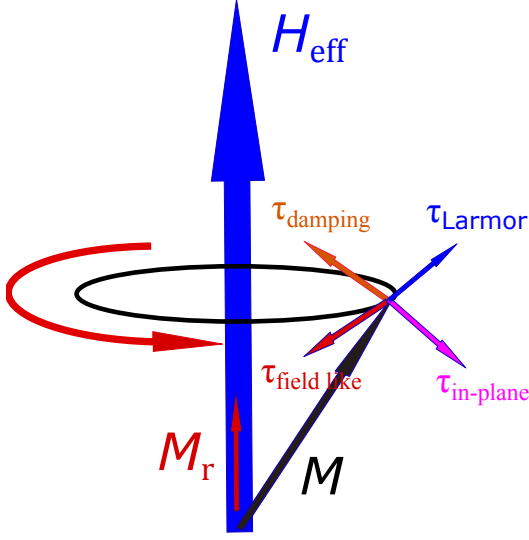


Figure 2.6: Magnetization dynamics described by the Landau-Lifshitz-Gilbert-Slonczewski equation.

In an MTJ, the effective magnetic field H_{eff} is the sum of the single domain anisotropy field H_K (only anisotropy of the FL is under consideration) and the external field H_{ex} :

$$H_{\text{eff}} = H_{\text{ex}} + H_K, \quad (2.10)$$

where H_K may result from magnetocrystalline anisotropy K_{mc} , magnetoelastic anisotropy K_{σ} , shape anisotropy K_{d} and interfacial anisotropy K_{s} [41].

In physics, the rate of change in angular momentum ($\frac{\partial L}{\partial t}$) is related to a torque (τ) on the object. The dynamics described in Eq. 2.9 is recognized as the change of angular momentum (left side, the magnetic moment has a relation with the angular momentum $\frac{\partial M}{\partial t} = \gamma_0 \frac{\partial L}{\partial t}$) with different torques (right side). The first term on the right side of Eq. 2.9 is the Larmor torque (τ_{Larmor}) which describes undamped magnetization precession around H_{eff} with the Larmor frequency $\tau_{\text{Larmor}}^{-1} = \gamma_0 H_{\text{eff}}$, as shown in Fig. 2.6. The second term is the Gilbert damping torque (τ_{damping}), leading to decay of the precession and alignment of the magnetization along H_{eff} .

Eq. 2.9 can well describe the magnetization relaxation after a stimulus. The magnetization precession or reversal can be driven by a magnetic field. However, in some cases, other driving forces can be more efficient and faster than the magnetic field.

2.2.2 Charge spin transfer torque

The development of STT-MRAM is based on the prediction of spin transfer torque (STT) by Berger and Slonczewski in 1996 [4,5]. They predicted that the local spin can be switched by simply sending a spin polarized charge current through the magnetic

layer. Here, I give a simple explanation of STT effect. The flow of angular momentum is equal to a spin current I_s , which can be created when itinerant electrons flow through a ferromagnetic layer $I_s = PI_c$, where I_c is the charge current and P is the spin polarization depending on the ferromagnetic material. The created spin current interacts with the local magnetization of the second magnetic thin layer when spin polarized itinerant electrons flow through it. To conserve of the angular momentum, a change in the direction of the spin angular momentum of the itinerant electrons results in a torque $\tau = (\frac{\partial M}{\partial t})_{\text{STT}}$ on the local magnetization of the magnetic thin layer [42]. The torque can be in the plane of the magnetic layer or perpendicular to the plane. The former one refers to in-plane spin transfer torque $\tau_{\text{in-plane}}$, the latter one is named out of plane spin transfer torque or field-like torque $\tau_{\text{field like}}$. The first experimental observation of STT driven magnetization reversal was reported in Co/Cu/Co pillars in 2000 [43]. A few years later, the STT effect in an MTJ was observed [44–49].

The LLG equation is modified when the STT is included:

$$\frac{\partial M}{\partial t} = \gamma_0 M \times H_{\text{eff}} - \frac{\alpha}{M_s} \left(\frac{\partial M}{\partial t} \times M \right) - \frac{\gamma_0 \hbar}{2eM_s V} (M \times (M \times I_s)) - \frac{\gamma_0 \hbar \beta_s}{2eM_s V} (M \times I_s), \quad (2.11)$$

where V is the volume of the magnetic layer, \hbar is the Planck constant, β_s gives the relative strength of the field like torque with respect to the in plane torque. The third and the last terms in the equation represent $\tau_{\text{in-plane}}$ and $\tau_{\text{field like}}$, respectively, as shown in Fig. 2.6. Depending on the polarity of I_s , $\tau_{\text{in-plane}}$ can enhance either the damping or the precession. In the latter case, a large enough STT can lead to a magnetization reversal.

The STT driven magnetization switching in MTJs is realized as following. When the MTJ needs to be switched from the AP state to the P state, a charge current is sent from the FL to the RL while spin polarized electrons flow from the RL to the FL. The majority spin angular momentum carried by the electrons has the same direction as the magnetization orientation of the RL and exerts a torque on the FL which has an opposite magnetization orientation with respect to the RL. With a certain amount of electrons, the magnetization orientation of the FL switches and the MTJ changes from the AP to the P state. Similarly, an opposite direction of the charge current is used to switch the MTJ from the P to the AP state. In this case, electrons with majority spin angular momentum go from the FL to the RL and electrons with minority spin angular momentum are scattered back to the FL, generating a torque on the FL and ultimately switching the magnetization orientation of the FL.

2.2.3 Thermal spin transfer torque

The spin current I_s can be generated not only by a charge current I_c , but also by a heat currents I_q . The spin transfer torque induced by heat currents is referred to as thermal spin transfer torque (T-STT), which was first predicted by Hatami in magnetoelectronic devices [50]. In a metallic spin valve without bias voltage, the thermal spin transfer torque is proportional to the temperature difference ΔT between the two magnetic layers [50]:

$$\tau \propto P'S\Delta T, \quad (2.12)$$

where S is the Seebeck coefficient and $P' = \frac{\partial(D^\uparrow - D^\downarrow)}{\partial(D^\uparrow + D^\downarrow)}$. Since the value of $P'S$ is restricted, the T-STT can be very large.

Theoretically, the magnetization precession and reversal in an MTJ can be realized by a heat current instead of a charge current. In ferromagnet/oxide/silicon tunnel junctions, researchers already found a spin accumulation in the silicon when one side of the junction was heated up [9]. Jia and Xia performed a first principle calculation on the Fe/MgO/Fe junction with different thicknesses of the barrier [10] by taking T-STT into account. They found that the T-STT decreases quickly with increasing thickness of the barrier. For an MTJ with a three-monolayers MgO barrier, the required temperature difference between two electrodes for MTJ switching from the AP to the P state is $\Delta T_{\text{MgO}}^{\text{AP-P}} = 6.5$ K, while from the P to the AP state it needs $\Delta T_{\text{MgO}}^{\text{P-AP}} = 56.5$ K. The large difference between the two cases is related to the nature of the coherent tunneling process in MgO barriers.

So far, the observation of T-STT on MTJs is indirect. Pushp *et al.* found that a temperature gradient can reduce the switching field from the AP to the P state but not for the P to the AP state [51], which agrees with the calculation of the T-SST effect in the MTJ [10]. Similar results are also obtained from two other groups [52, 53]. However, Michel *et al.* found a change in the switching field of a magnetic nanowire with an applied temperature gradient, and attributed it to a stress induced magnetoelastic effect due to the temperature gradient [54]. In any case, the study of T-STT effect on MTJ is still in progress.

2.2.4 Magnetoelastic effects

According to the LLG equation, the magnetization precession can also be excited by a sudden change of the anisotropy field $H_K = \frac{2K_u}{\mu_0 M_s}$, see Eq. 2.10, where $K_u = K_a + K_\sigma$ is the total magnetic anisotropy of the magnetic layer. Here, K_a contains all the other

magnetic anisotropy contributions except for the magnetoelastic anisotropy K_σ . The magnetoelastic effect is known as the inverse magnetostrictive effect or Villari effect, in which the magnetization of materials changes when they are subjected to a mechanical stress. The effect originates from the spin-orbit interaction. It can be described by a magnetic anisotropy field H_σ induced by a stress σ as follow [55]:

$$H_\sigma = \frac{3\sigma\lambda}{M_s} = \frac{3\lambda}{M_s} \frac{\varepsilon Y}{1 - \nu^2}, \quad (2.13)$$

where the magnetostriction constant λ characterizes the change in the magnetization by the stress, ε is the uniaxial strain induced by the stress, and in general, it is considered positive for a tensile stress and negative for a compressive stress, Y is Young's modulus and ν is the Poisson ratio. In the static case, one can use stress-induced H_σ to rotate and reverse the magnetization similar to a magnetic field. The MTJ is highly sensitive to the strain. A change in the strain $\Delta\varepsilon$ on the order of 4×10^{-4} leads to a change in the tunnel resistance of 24% [11], which makes the MTJ a good candidate for strain sensors [56].

The strain can be produced by mechanical stress, oscillating electric fields on a piezoelectric material, or optical excitation. To excite magnetization precession and induce a fast reversal, the strain pulse should be short enough which is possible using femtosecond lasers [57–60]. Femtosecond laser pulse can generate different acoustic pulses. Two representatives of them are the picosecond strain pulse and the nanosecond surface acoustic wave (SAW).

The acoustic pulse induced magnetization dynamics results from the magnetoelastic effect, and Eq. 2.13 can be modified with specific strain tensors corresponding to various acoustic waves. The dynamic magnetoelastic field can be calculated via the variational derivative of the magnetoelastic energy E_{mel} and is written as [61]:

$$H_{\sigma(\text{dyn})} = -\frac{\delta E_{\text{mel}}}{\delta M}, \quad (2.14)$$

where E_{mel} is expressed as:

$$E_{\text{mel}} = \frac{b_1}{M_s^2} \sum_i M_i^2 \varepsilon_{ii} + \frac{b_2}{M_s^2} \sum_i \sum_{j \neq i} M_i M_j \varepsilon_{ij}, \quad (2.15)$$

where $i, j = 1, 2, 3$ are referred to as the Cartesian coordinates. M_i, M_j are the magnetization components along the axes i, j , respectively; b_1, b_2 are the magnetoelastic constants [61, 62]. $\varepsilon_{ij}(r, t) = (\partial u_i / \partial x_j + \partial u_j / \partial x_i) / 2$ are the components of the strain tensor, where u_i is the displacement vector. Since the picosecond strain pulse is a longitudinal wave, it only has the displacement normal to the plane. In contrast, the SAW has both, normal and transverse displacements simultaneously on the surface.

Magnetization dynamics have been observed in the ferromagnetic thin films and ferromagnetic semiconductors excited by acoustic pulses [12, 63, 64]. The amplitude of the magnetization precession both experimentally and theoretically strongly depends on the resonant interaction between the magnetic and the elastic modes [65, 66]. An analytical and numerical approach has been developed to study the switching of magnetization in magnetic semiconductors with SAWs. It was found that SAWs could be a more promising way for magnetization switching than picosecond acoustic pulses [67]. Still, the study of acoustic pulse induced magnetization dynamics and magnetization reversal in spintronic devices like MTJs is lacking.

2.2.5 Thermal effects

Thermal effects are not included in the LLG equation (only implicitly in the temperature dependent M_s), since the equation describes the magnetization dynamics at a certain temperature and assumes that there is no change in the magnitude of magnetic moments. But thermal effects are critical for laser induced ultrafast magnetization dynamics [39], which is addressed by the Landau-Lifshitz-Bloch (LLB) model [68] or the 3 temperature model. However, the ultrafast time regime (≤ 100 ps) is beyond the scope of this thesis. Another important thermal effect is thermal noise. In MTJs, when the magnetizations of the FL and the RL are collinear, it is impossible to switch the magnetization with a spin polarized charge current, since STT is zero in this case. But due to the thermal noise, the magnetization randomly deviates from its minimum energy direction, so that magnetization switching can be realized with nonzero STT.

2.3 Laser excitation

2.3.1 Optically induced heat currents in MTJs

Heat can be carried by electrical carriers (electrons or holes), lattice waves (phonons), spin waves, or other carriers. In metallic materials, the majority of the heat is transmitted by electrons, while in insulators, heat transport by the lattice is dominant. With femtosecond laser pulse excitation, photons are used to impose heat to the MTJ. Different processes occur during the time scale of heat transport.

When a laser pulse hits the surface of the MTJ (covered with 300 nm Al layer on the surface, as shown in Fig. 2.7.), firstly, electrons in the Al layer below the Fermi surface interact with the photon field and are excited out of the equilibrium within the laser pulse width. This time regime is called non-thermal regime since electrons can

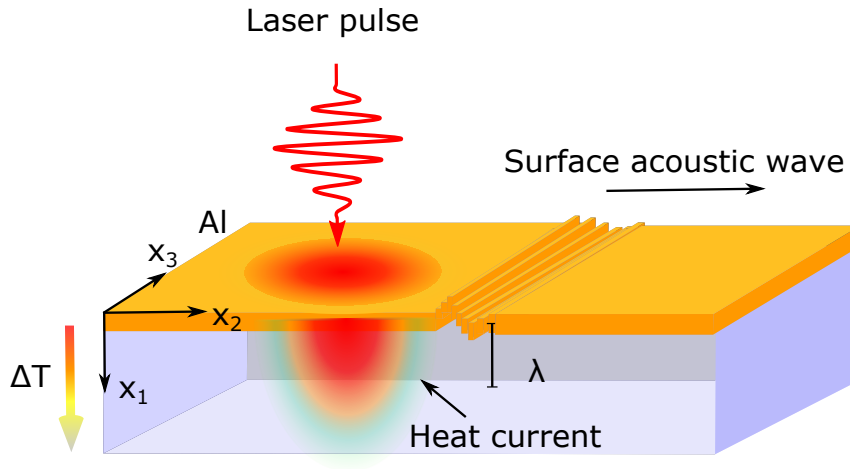


Figure 2.7: A schematic of femtosecond laser pulse generated heat current and SAW.

not be characterized with a certain temperature. Following this regime, electrons are thermalized to a high temperature (up to 10^3 K) due to electron-electron coupling. The excited electrons are called ‘hot electrons’. Since there is a large temperature difference between the electrons and the lattice, the heat energy transfers into the lattice due to the electron-phonon coupling. The temperatures of electrons and the lattice are going to reach an equilibrium in the next tens of picoseconds. Finally, the heat diffuses from the surface into the substrate of the MTJ. Heat transport in the time regime is following Fourier’s Law, $q = -\kappa\Delta T$, where q is the heat flux, κ is the thermal conductivity and ΔT is the temperature difference, this process takes several nanoseconds. For the study of thermal effects in MTJs, two time regimes are relevant: the hot electron regime and the heat diffusion regime. In the former regime, a large temperature difference can be created between layers due to a difference of the electron-phonon coupling coefficients of the layers, which results in a large heat current in the first tens of picoseconds. The T-STT effect has been observed in spin valves due to the spin-dependent Seebeck effect in this time regime [69], as described in Eq. 2.12. In the heat diffusion regime, the created temperature difference (heat current), which depends on the heat source and the thermal conductivity of the layers, is one or two orders of magnitude smaller.

Our MTJ sample is a buried structure with the MTJ stack far away from the surface. The MTJ stack is covered by 150 nm thick cap layers, above this, there is an additional 300 nm thick Al layer serving as the heat absorber. The optical penetration depth in the Al layer is only 80 nm for our laser beam, thus, the hot electrons are mostly

confined to the surface layer. In this case, the heat current is determined by the heat diffusion through the MTJ.

To precisely characterize the temperature of nanoscale multilayers and the temperature drop between layers is a big challenge. In general, the heat transport in nanoscale structure is simulated by means of COMSOL Multiphysics simulation [70]. The time resolved temperature of each layer and the temperature difference between the layers can be extracted from the simulation. However, the simulation requires a good knowledge of the thermal conductivity of each layer and, in particular, of the interface thermal conductances between the layers, which is critical for nanoscale heat transport and have not been well studied till now. The calculated time dependent temperature gradients depend on whether the interface thermal conductance is taken into account and the obtained temperature drop across the barrier show a huge difference in the MTJ, details of the simulation are discussed in chapter 4. Thus, it is necessary to develop a method which can validate the COMSOL simulation.

2.3.2 Optically induced surface acoustic waves

Surface acoustic waves (SAW), usually also called Rayleigh waves, were discovered in 1885 by Lord Rayleigh. SAWs propagate along the surface with a combination of longitudinal motion and transverse motion, penetrating to about one wavelength in depth, as shown in Fig. 2.7. Laser generated SAWs have been intensively studied since the 1980s. They can be generated with focused laser pulses [71], transient optical gratings [72] or periodic patterned transducer illuminated with a laser pulse [73]. SAWs generated by focused laser pulses are due to thermo-elastic coupling. When an optical pump pulse is absorbed in the sample, a sudden rise of local temperature induces a thermal dilatation which leads to the generation of elastic waves.

The whole process can be expressed by two interrelated equations in a transversely isotropic system. The incident laser pulse being focused on the surface $x_1 = 0$ in cartesian coordinates (x_1, x_2, x_3) . The temperature $T(x_1, x_2, t)$ satisfies the heat diffusion equation:

$$\rho c_p \frac{\partial T}{\partial t} = \nabla \cdot (\boldsymbol{\kappa} \nabla T) + Q, \quad (2.16)$$

where c_p is the heat capacity, ρ is the density, $\boldsymbol{\kappa}$ stands for the tensor of heat conductivity and Q is the time and space dependent energy from a Gaussian laser pulse and given by [74, 75].

$$Q(x_1, x_2, t) = \beta A_0 (1 - R) G(x_2) F(t) e^{-\beta x_1}, \quad (2.17)$$

where A_0 is the optical incident energy, β stands for the optical absorption coefficient, R is the optical reflectivity. Here the authors assume that the absorbed energy will not change with the increase of the pulse intensity. $G(x_2)$ and $F(t)$ are the lateral Gaussian distribution intensity and the laser pulse intensity in time, respectively.

The acoustic wave equation due to the thermoelastic effect can be written as

$$\rho \frac{\partial^2 \mathbf{u}}{\partial t^2} = \nabla \cdot (\mathbf{C} : \nabla \mathbf{u}) - (\mathbf{C} : \boldsymbol{\zeta}) \nabla T, \quad (2.18)$$

where \mathbf{u} is the displacement field at any time and position, $\boldsymbol{\sigma}$ is the stress tensor, \mathbf{C} is the fourth order stiffness tensor and $\boldsymbol{\zeta}$ is the thermal expansion tensor of the material.

Higuet provided a method to calculate spatial and temporal evolution of the normal displacement u_1 in the frequency-wavelength domain [76]. The solution of Eq. 2.16 can be found in the dual space (ω, k_2) by taking into account the Neumann boundary condition and it is written as

$$T(x_1) = \frac{\beta A_0 (1 - R)}{\kappa (j\omega \frac{\rho c_p}{k} + k_2^2 - \beta^2)} e^{-\beta x_1} + \frac{\beta A_0 (1 - R)}{\kappa (j\omega \frac{\rho c_p}{k} + k_2^2 - \beta^2)} \frac{-\beta}{\sqrt{\kappa (j\omega \frac{\rho c_p}{k} + k_2^2)}} e^{-\sqrt{\kappa (j\omega \frac{\rho c_p}{k} + k_2^2)} x_1}. \quad (2.19)$$

Using Eq. 2.19 as source term for Eq. 2.18, both longitudinal and transverse bulk waves can be extracted from the solution of Eq. 2.18 in the (ω, k_2) space. By using the inverse Fourier transform, the spatial and temporal evolution of the normal displacement u_1 is calculated from the amplitude of bulk waves, u_1 also can be measured experimentally with the beam distortion detection technique, which will be described in chapter 3. The obtained u_1 can be used as a driving force for the magnetization dynamics simulation described by Eq. 2.15.

3 Experimental details

3.1 Samples

In this thesis, CoFeB/ MgO/CoFeB based MTJ samples are used. They were fabricated in a Timaris Singulus tool at the International Iberian Nanotechnology Laboratory (INL) [77]. The MTJ stack is deposited on a Si wafer covered by a 100 nm thick Al₂O₃ layer serving as an isolating bottom layer. The sample is finally covered with 300 nm Al layer on the surface. Upon deposition, the wafers are annealed for 2 h at 330 °C and cooled down under a magnetic field of 1 T along the easy axis to maximize the TMR ratio. The MTJ stacks were patterned into elliptical and rectangular pillars with lateral dimensionless from 0.02 to 0.55 μm . The pillars were contacted by lithographically defined top (TC) and bottom (BC) contacts as shown in Fig. 3.1. The patterning was performed at INL.

Table 3.1 describes the whole stack sequence of the MTJ samples in detail. Two series of MTJ samples have been used. Despite other differences in the stack, the main difference between the two deposited wafers concerns the FL thickness: for sample type A, $t_{\text{CoFeB}} = 2.6$ nm and for sample type B, $t_{\text{CoFeB}} = 1.2$ nm. In the samples A, the FL has an in plane uniaxial magnetic anisotropy, while in the samples B, the FL has an out of plane anisotropy and it is more sensitive to the STT. For the samples A, the FL (red) is above the RL (blue) while the FL is underneath the RL for the sample B. The high TMR ratio of 100 % to 120 % speaks for the good quality of the samples A. A general cross section of the layer structure of the patterned samples is schematically shown in Fig. 3.1 (a).

Figure 3.1(b) gives the top view of the MTJ sample. The MTJ is located at the point indicated by the yellow dot in the center of the microscope image. The maximal size of the MTJ is about 550×200 nm, while the width of a used laser spot in the thesis is about 7 - 10 μm . The lateral temperature distribution for the MTJ stack under illumination of the laser beam can be considered homogeneous.

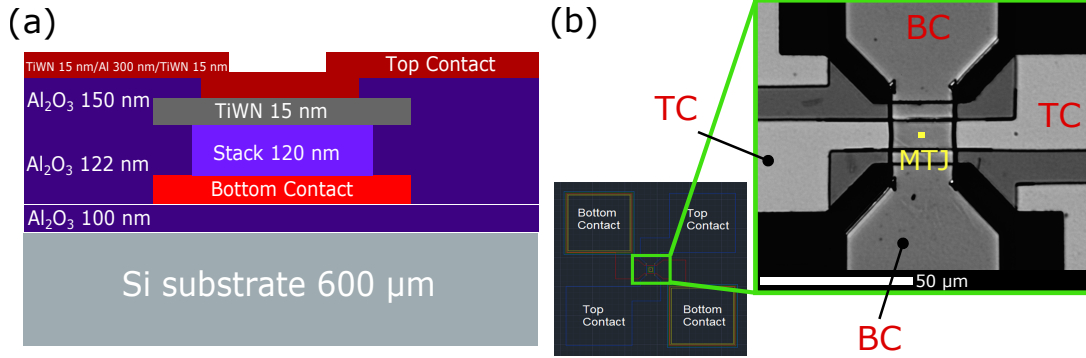


Figure 3.1: (a) A schematic of cross section for the layer structure of the MTJ nanopillars fabricated at INL. (b) Microscope image of one MTJ sample. The yellow dot marks the position of the MTJ nanopillar.

3.2 All optical pump-probe setup.

3.2.1 Time domain thermoreflectance method

Time domain thermoreflectance (TDTR) is an optical pump and probe technique, which has been extensively used to study thermal transport phenomena in bulk materials or nanostructures, and to characterize thermal conductivities and interface thermal conductances in super-lattice structures due to its high spatial and temporal resolution by utilizing femtosecond laser pulses [78–80]. In a TDTR measurement, as shown in Fig. 3.2(a), a pump pulse is focused on the surface and heats up the material. The temperature variation of the material results in a change in the optical properties, e.g. reflectance. Following the pump pulse, a time delayed probe pulse detects the temperature dependent reflectance. By tuning the time delay with a delay stage which changes the difference of the optical path length between pump and probe pulses, the reflectance at various times after the pump pulse can be recorded. A heat transport model in the system under study is usually required. By fitting the measured data with the model, the unknown parameters like thermal conductivity of the layer or interface thermal conductance between the layers can be extracted.

Figure 3.2(b) shows the schematics of the TDTR setup. The laser pulse is obtained from a Ti: Sapphire laser with repetition rate of 76 MHz at a center wavelength of 790 nm, the pulse width is about 100 fs. The output laser beam is split into two arms (pump and probe beams) by a polarized beam splitter (PBS). To tune the power of pump and probe beams, a half-wave plate is placed before the PBS. The pump beam is modulated at 1 MHz by an acoustic optic modulator (AOM) to enable Lock-in detection. After the modulation, the second harmonic of the pump beam (blue light with $\lambda_{\text{pump}} \approx 400$

Table 3.1: The basic properties and details of the composition of the MTJ samples. The layer structure is described from top to the bottom. The FL (red color) and the RL (blue color) are made of $\text{Co}_{40}\text{Fe}_{40}\text{B}_{20}$ and the pinned layer PL is made of $\text{Co}_{70}\text{Fe}_{30}$.

Samples	MTJ	
	A	B
$H_K(\text{FL})$	in plane	out of plane
Shape	rectangular	elliptical
TMR	100-120 %	10-70 %
$R \times A$	$1.8 \Omega \mu\text{m}^2$	$3 \Omega \mu\text{m}^2$
	Layer (nm)	Layer (nm)
Surface and top contact	Al (300) TiWN (30)	
cap layers	Al (74)	Ru (30)
	Ru (7)	Cu (100)
	Ta (10)	Ru (45)
FL	CoFeB (2.6)	IrMn (20)
Barrier	MgO (0.8)	CoFeB (2)
	CoFeB (2.6)	Ru (0.85)
SyAF	Ru (0.85)	CoFe(2.2)
	CoFe (2)	MgO (0.8)
AF	IrMn (20)	CoFeB (1.2)
bottom contact	Ru (20)	
	CuN (50)	
	Ru (10)	Ta (50)
	CuN (50)	
Isolator layer	Ta (5)	
	AlO (100)	
Wafer	Si	

nm) is generated in a Beta-Barium borate (BBO) crystal. The fundamental component of the pump beam (red light with $\lambda_{\text{pump}} \approx 790$ nm) is blocked when the pump beam goes through a short pass filter (cut-off wavelength: 550 nm). The probe beam goes through a 0.6 m long mechanical delay stage, corresponding to 8 ns delay time (beam goes towards delay stage twice). The pump and probe beams are collinearly focused on the sample by an $10 \times$ or $20 \times$ objective or comparable lens. The reflected probe and pump laser beams are monitored on a CCD camera, thus, the position of two laser

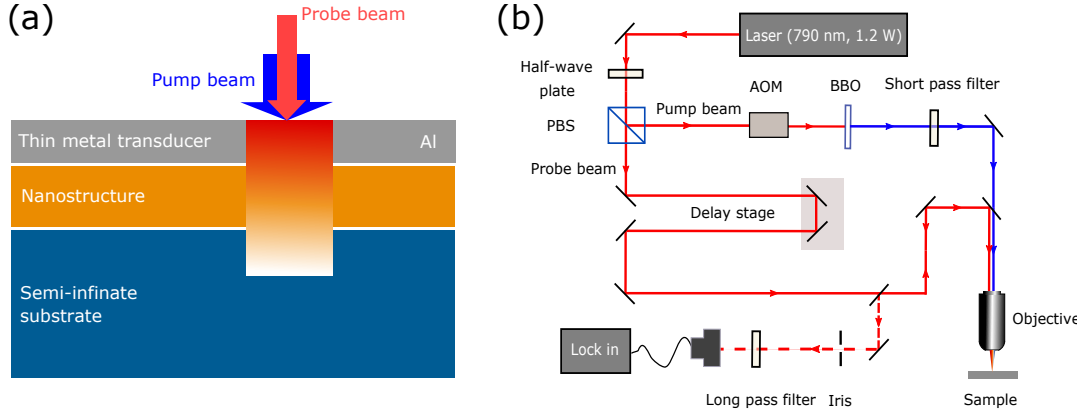


Figure 3.2: (a) Optical pump and probe technique. The Al layer on the surface serves as a transducer. (b) A schematic of pump and probe setup for TDTR and BDD. PBS : polarized beam splitter, BBO: Beta-Barium borate, AOM: acoustic optic modulator

beams can be easily adjusted. A long pass filter (cut-off wavelength: 700 nm) is placed before the detector to block the reflected pump beam going into the photodiode. The intensity change of the probe beam due to temperature rise and subsequent cooling of the surface of the sample is recorded by a lock-in amplifier set to the frequency of the AOM.

In the TDTR measurement, a thin Al layer is commonly coated on the surface. Due to its high thermorefectance, this layer serves as a transducer to absorb the energy from the pump beam and convert the surface temperature change into the intensity change of the reflected probe beam. Our MTJ samples are coated with a 300 nm thick Al layer. This avoids that any light directly interacts with the magnetic layer in the MTJ sample. The spot size of the laser beam on the surface is measured by a knife edge method. For the $10\times$ objective and a lens with a focus length of 12 mm, the $1/e^2$ radii of beam is about $8\ \mu\text{m}$.

The ratio of the in-phase (V_{in}) to the out-of-phase (V_{out}) signals of the lock-in amplifier is fitted to a numerical solution of the thermal transport model, which is provided by Cahill [79]. In his model, for a pump beam with a Gaussian spatial distribution, the weighted average of the temperature distribution on the surface measured by the probe beam is expressed as [79]:

$$\Delta T = 2\pi A \int_0^\infty G(k) \exp(-\pi^2 k^2 (w_0^2 + w_1^2) k) dk, \quad (3.1)$$

where A is the heat absorbed by the sample, w_0 and w_1 are the $1/e^2$ radius of the pump and probe beam, respectively. $G(k)$ is the frequency domain solution of the one dimensional heat diffusion equation. The upper limit of the integral is set to

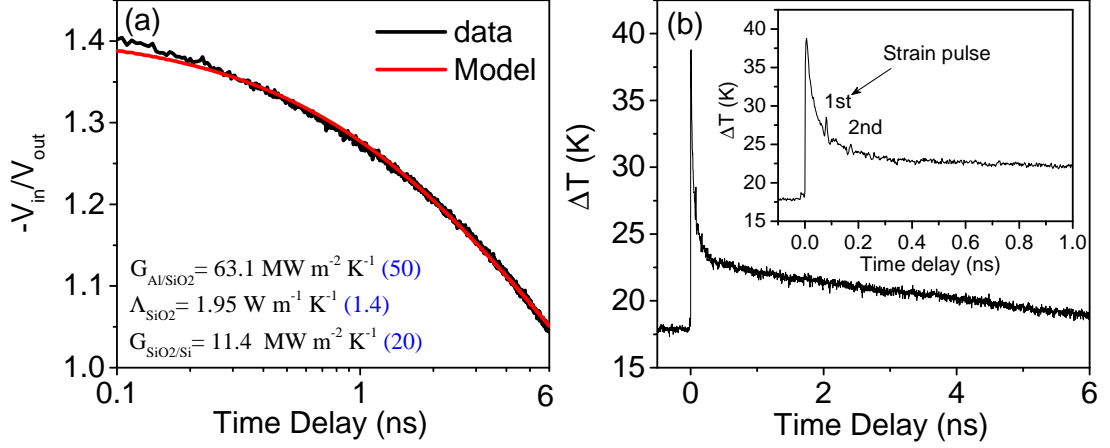


Figure 3.3: (a) Illustration of the fitting algorithm using measurement data obtained from the multilayer (100 nm Al/ 600 nm SiO₂ / Si substrate) at a modulation frequency of 1 MHz. The fit starts 0.1 ns after the pump pulse hit the surface. At this time, electrons and phonons have the same temperature. The obtained interface thermal conductances and thermal conductivity are shown in the figure, values in the brackets are taken from literature [81]. (b) Surface temperature changes after femtosecond laser excitation extracted from the TDTR method. Inset: The peaks occurring after the maximum are reflections of the strain pulse.

$$2/(w_0^2 + w_1^2)^{1/2}.$$

The parameters needed for the model include thickness, heat capacity, thermal conductivity of each layer and interface thermal conductance between the layers. The unknown parameters of the layers are determined from a best fit with the experimental data by adjusting unknown parameters in the model. Figure 3.3(a) shows an example of fitting results for the multilayer Al/SiO₂/Si. The unknown fitting parameter like interface thermal conductance $G'_{\text{Al/SiO}_2}$ and thermal conductivity of SiO₂ can be extracted from the fit. The deviations of the obtained values from the literature is might due to the non-symmetric laser beams. The sample is used to validate the TDTR setup due to well known thermal properties of the layers.

The measured voltage V_t is directly related to the temperature change $\Delta T(t)$ of the surface. $\Delta T(t)$ is determined from the following relation [80, 82]:

$$\Delta T(t) = \sqrt{2} \left(\frac{V_t}{V_0} \right) \left(\frac{R}{dR/dT} \right), \quad (3.2)$$

where t is the delay time between pump and probe pulses, V_0 is the dc voltage in the photodiode, R (0.87) is the reflectivity of Al for the probe beam and dR/dT ($2.1 \times 10^{-4} \text{ K}^{-1}$) is the thermoreflectance coefficient of Al. We can estimate a steady temperature rise

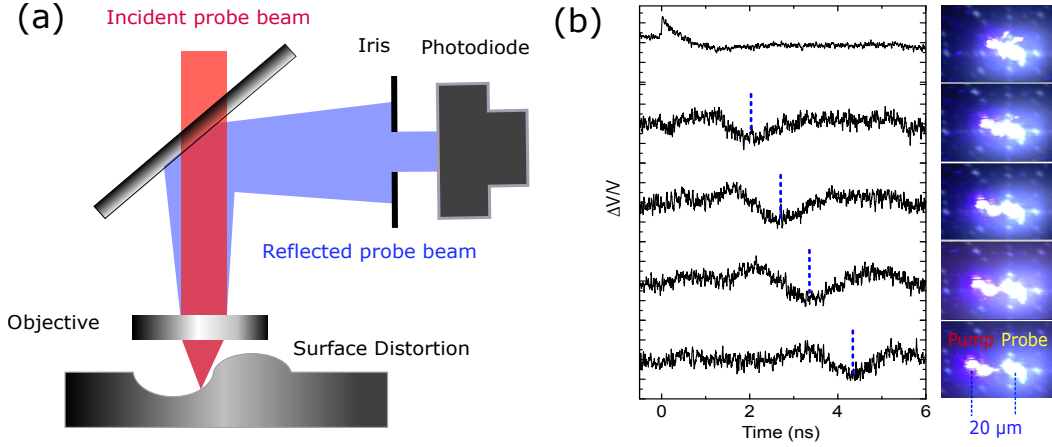


Figure 3.4: (a) Mechanism of beam distortion detection technique (BDD). (b) The left side of the figure shows the measured SAWs as a function of distance between pump and probe beam (0, 5.3, 8.9, 13.4 and 14.7 μm). The right side of the figure shows the image of the pump and probe spots from the CCD camera.

due to heat accumulation, as shown in Fig. 3.3(b). The peak temperature in the figure results from thermalized electrons before they transfer energy to the lattice, which occurs in the hot electron time regime. But we are more interested in the subsequent heat diffusion regime where electrons and the lattice have the same temperature. The peaks shown in the inset of Fig. 3.3(b) correspond to laser generated ballistic phonon pulses, which propagate into the sample and get reflected back and forth between the Al/SiO₂ interface and surface due to acoustic impedance mismatch. The strain pulse has a velocity of sound (6.42 nm ps^{-1}) in the Al layer, from which we calculate the thickness of the Al layer. The measured thickness of the Al layer is 295 nm being in a very good agreement with the nominal thickness of 300 nm.

3.2.2 Beam distortion detection technique for surface acoustic waves

Based on the pump-probe technique, laser-induced SAWs as described in chapter 2 can be measured by inserting an additional iris in the TDTR setup before the detector in Fig. 3.2(b). This technique is referred to as beam distortion detection technique (BDD) [76, 83].

A pump laser pulse with a power of 2 mW ($\lambda_{\text{pump}} \approx 400 \text{ nm}$) is focused with a $10\times$ objective on the sample surface and generates SAWs due to thermoelastic coupling. Such a propagating SAW, results in a local change of surface curvature. When a probe beam with a power of 0.5 mW reaches the surface, the surface displacement modifies

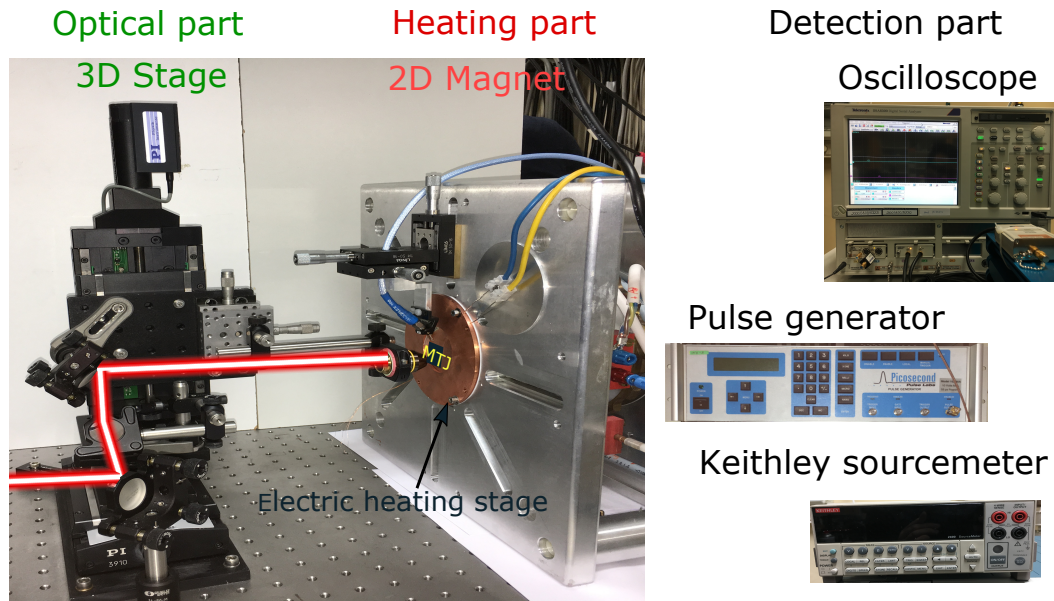


Figure 3.5: Setup used for electrical resistance measurement. It mainly consists of three parts. From left to the right, they are the optical part, the heating part and the detection part.

the probe beam radius after the reflection from the surface as shown in Fig. 3.4(a). The modified probe beam transmits through an iris and the intensity change of the probe beam is detected by the photodiode. The change of the probe beam after the iris is proportional to the normal displacement of the surface. In practice, the iris is centered on the probe beam, and the transmission of the power is set to 50 % to get a maximal sensitivity with respect to the changes of the reflected probe beam.

To study the SAW propagation, the distance of pump and probe beams was increased stepwise. The positions of pump and probe beam were monitored by a CCD camera. Figure 3.4 (b) shows the measured SAW traces as a function of distance between pump and probe beams. When the spots of the pump and probe beams partially overlap (nearly same position), the setup is the same as in the TDTR experiment. So the measured signal $\Delta V/V$ shows a sudden change at the delay time of $\Delta t = 0$ following by a slow decay. After pump laser excitation, the electron temperature reaches on the ps time scale, followed by nanosecond time scale heat diffusion from the surface to the underneath substrate. A detailed analysis of the measured SAWs is presented in chapter 6.

3.3 Electrical resistance measurement setup

The setup for resistance measurement is shown in Fig. 3.5. It consists of three main parts.

- The optical part is on the left-hand side of the Fig. 3.5, consisting of the laser system, a 3D moveable stage, a CCD camera, a photodiode and all the optical components. Two femtosecond laser systems have been used: One is a Ti: Sapphire laser with a repetition rate of 76 MHz, a center wavelength of 790 nm, a pulse width of about 100 fs, and a maximum pulse energy of $P_{\text{pulse}} \approx 15$ nJ. The other one is a Yb doped fiber laser with a variable repetition rate from 300 kHz to 24 MHz, a center wavelength of 1050 nm, a pulse width of about 300 fs, and a maximum pulse energy of about $P_{\text{pulse}} \approx 20$ μ J. Limited by the low melting point of the Al layer on the surface, the applied laser pulse energy should not exceed 15 nJ with an $10 \times$ objective. The CCD camera was used for imaging the sample surface and the laser heating position. The 3D moveable stage with a travel range of several cm was used to change the heating position. A part of the laser beam excited a fast photodiode and the measured voltage $V_{\text{photodiode}}(t)$ was used as the trigger signal for the sampling oscilloscope.
- In the middle of the figure is the heating part of the setup. The main modules include a 2D magnet and an electric heating stage. The in-plane magnetic field (H_{ex}) can be applied in an arbitrary angle with a pair of magnetic fields (H_x and H_y in the Cartesian coordinate system) generated by a 2D magnet system. On the surface of the magnets, there is a resistance heater line isolated by a Teflon layer and it is covered by a layer of copper. The temperature of the copper can be heated up to 65 °C with a dc voltage of 2 volts through the heater line. The temperature of the copper is measured with a resistance temperature sensor Pt100. Since the structure of the heater line is well designed, the maximum magnetic stray field created by the heater line is less than 1 Oe and can be neglected for the data analysis. The MTJ sample is fixed to the heating stage through a vacuum tube. Prior to each electric heating measurement, the temperature is stabilized by waiting for 1 hour at the nominal temperature.
- The last part of figure is the detection part. A Keithley sourcemeter (2400) is used as a current source and also to measure the static resistance of the MTJ. A sampling oscilloscope (Tektronix: DSA8300) is used to measure the time resolved resistance change of the MTJ with a maximum bandwidth of 20 GHz. A pulse generator is used to generate short voltage pulses with a pulse width down to tens of picoseconds, which are used to induce precessional dynamics in the MTJ.

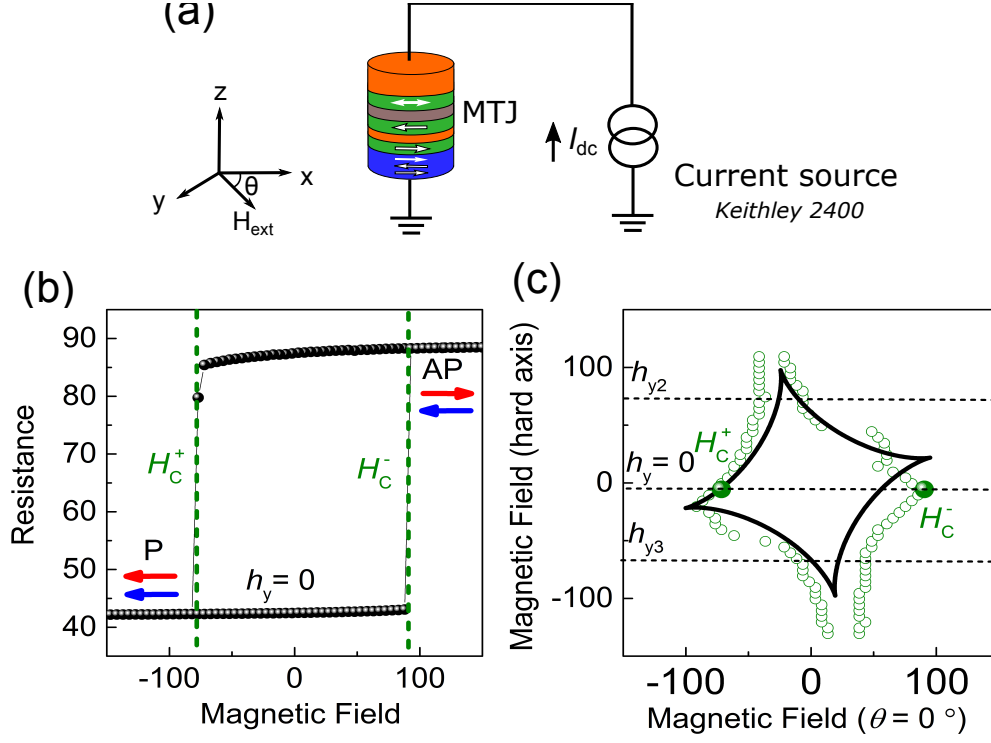


Figure 3.6: (a) Setup used for magnetoresistance (MR) measurement. (b) Typical MR loop measured when the magnetic field sweeps along the nominal easy axis ($\theta = 0^\circ$) of the MTJ without bias magnetic field. H_C^+ and H_C^- are the coercivity field of the FL when its magnetization switches from the high resistance state (AP state) to the low resistance state (P state) and vice versa, respectively. (c) Extracted astroid (hollow green circles) extracted from MR loops, which are measured at bias magnetic fields along the nominal hard axis. The filled green circles represent the switching points extracted from the figure (b).

3.3.1 Static resistance measurement

A four-wire sensing method is employed for the static magnetoresistance (MR) measurement. The resistance is measured with a Keithley 2400 by sending a small dc current $I_{dc} \leq 100 \mu\text{A}$ through the MTJ as shown in Fig. 3.6(a). Figure 3.6(b) shows a typical plot of a measured MR loop of the FL when the magnetic field is swept along the nominal easy axis of the MTJ ($\theta = 0^\circ$). The switching fields H_C^+ and H_C^- can be extracted from the MR loop when the magnetization of the FL switches from the AP state to the P state and from the P state to the AP state, respectively.

To get the Stoner-Wohlfarth astroid curve of the MTJ, a series of MR loops are measured by sweeping the magnetic field (h_x) along the nominal easy axis at a variety of bias magnetic fields (h_y) in the 2D field system. The extracted H_C^+ and H_C^- from each

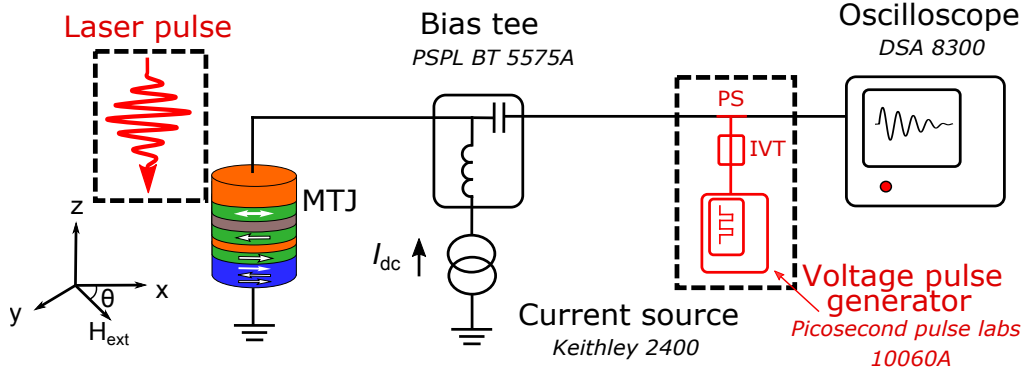


Figure 3.7: Schematic of the setup used for time resolved resistance measurement. Two excitation sources: laser pulse or voltage pulse. For laser pulse excitation, the pulse generator is not connected. With voltage pulse excitation, a power splitter (PS) is inserted between the bias tee and the oscilloscope so that half of the generated voltage goes into MTJ and the other half to oscilloscope. A voltage inverter (IVT) is used to change the polarity of the voltage pulse.

MR loop are plotted as a function of h_x and h_y as shown schematically in Fig. 3.6(c). The measured astroid is not perfect, most likely, because the MTJ does not have an ideal shape due to the lithography. The Stoner-Wohlfarth astroid curve characterizes the magnetization reversal of the FL in applied magnetic fields and can well describe the angular dependence of the switching field of the FL with uniaxial anisotropy by a uniform macrospin model. By fitting the experimental switching points with a Stoner-Wohlfarth model, the anisotropy field of sample can be obtained.

3.3.2 Time resolved resistance measurement

In the thesis, the magnetization dynamics is excited either by thermal and magnetoelastic effect with a laser pulse or by the STT with a voltage pulse. To measure time resolved resistance change which result from magnetization dynamics of the MTJ, we use a sampling oscilloscope (DSA8300) with 50Ω input impedance and 20 GHz bandwidth. The setup is shown in Fig. 3.7. For the laser excitation, the system consists of the MTJ, a bias tee with dc current source and the oscilloscope. For excitation by electric STT with voltage pulses, additional electric components are needed, i.e. a power splitter and a voltage inverter.

For measuring magnetization dynamics upon STT excitation, a weak dc detection current ($I_{dc} = 0.2 \text{ mA}$ or 0.4 mA) is applied through a bias tee and fed into the MTJ. Additionally, a voltage pulse with a duration of a few ns is generated by the pulse

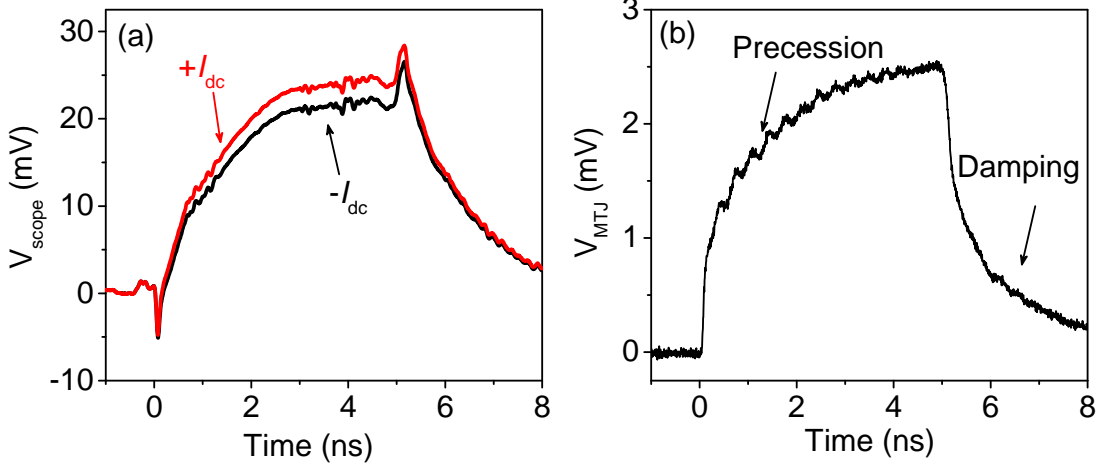


Figure 3.8: (a) Voltage traces $V_{\text{scope}}(t)$ measured by a sampling oscilloscope when $\pm I_{\text{dc}}$ are applied through the MTJ with a 5 ns voltage pulse excitation. (b) The obtained voltage trace $V_{\text{MTJ}}(t)$ of the MTJ after subtraction of the two voltage traces $V_{\text{scope}}(t)$ shown in figure (a).

generator. The pulse is split at the power splitter, travels to the MTJ, and excites the precession. Due to impedance mismatch, a part of voltage pulse is reflected back and travels to the oscilloscope. A resistance change of the MTJ excited by the voltage pulse in combination with the dc bias current results in a high frequency signal, which is generated by the MTJ and detected by the sampling oscilloscope. The voltage $V_{\text{scope}}(t)$ displayed by the oscilloscope can be written as

$$V_{\text{scope}}(t) \approx V_{\text{MTJ}}(t) + V_{\text{bg}}(t), \quad (3.3)$$

where $V_{\text{bg}}(t)$ is the background voltage mainly due to the back reflected voltage pulse which is independent on the polarity of I_{dc} . In contrast, the sign of $V_{\text{MTJ}}(t)$ is dependent on the polarity of I_{dc} . According to Ohm's law, the voltage $V_{\text{MTJ}}(t)$ across the MTJ is proportional to the resistance $R_{\text{MTJ}}(t)$ of the MTJ and the dc current I_{dc} . A large dc current should also be avoided due to the self heating and spin transfer torque effect in the MTJ. To get rid of the background signal, we make a subtraction of the measured $V_{\text{scope}}(t)$ for positive and negative I_{dc} . Figure 3.8(a) shows the measured voltage traces with a 5 ns step-like voltage pulse for $+I_{\text{dc}}$ and $-I_{\text{dc}}$, respectively. To improve the signal to noise ratio, the measured $V_{\text{scope}}(t)$ traces are usually averaged 2000 - 4000 times. After the subtraction of the two traces, the obtained $V_{\text{MTJ}}(t)$ is shown in Fig. 3.8(b). The signal of $V_{\text{MTJ}}(t)$ changes slowly during the voltage pulse which results from self heating, due to the temperature dependence of the MTJ resistance. During the voltage pulse, a clear oscillating signal due to STT induced magnetization precession can be found in the signal. After the voltage pulse, the excited nonequilibrium orientation of

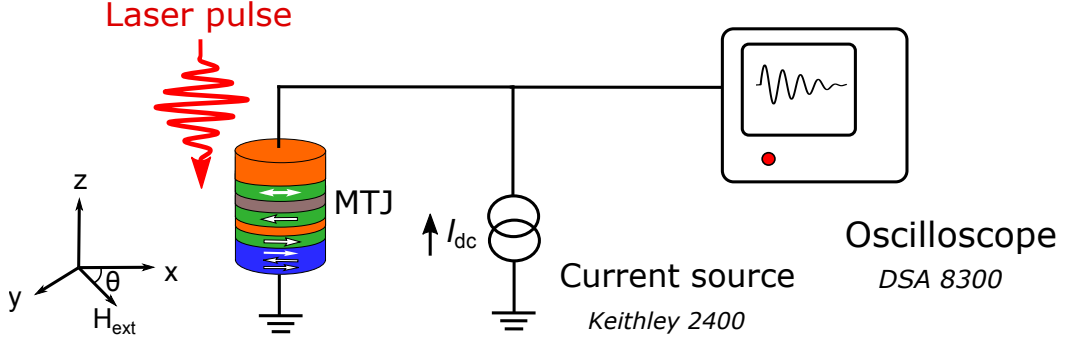


Figure 3.9: Setup used for time resolved resistance measurement results from temperature effects in the MTJ.

the magnetization slowly relaxes to the equilibrium state and a damping or ringing like behavior can be observed in the trace.

The setup shown in Fig. 3.7 is used to measure the magnetization dynamics of the MTJ due to STT (including charge current and heat current) and magnetoelastic effects.

With a laser pulse excitation, there is also a strong temperature effect on the resistance of the MTJ. To measure time resolved resistance change caused by the temperature effect due to laser pulse heating, the Keithley sourcemeter and the oscilloscope are connected in parallel to the MTJ with two picoprobes, as shown in Fig. 3.9. In this case, a large I_{dc} can be applied to have a better signal to noise ratio. For the four wire sensing, resistance change of the MTJ $R_{\text{MTJ}}(t)$ can be calculated from the following relation:

$$I_{\text{dc}} = \frac{V_{\text{scope}}(t)}{R_{\text{scope}}} + V_{\text{scope}}(t) \frac{R_{\text{scope}} + R_{\text{contact}}}{R_{\text{scope}} \times R_{\text{MTJ}}(t)}, \quad (3.4)$$

where $R_{\text{scope}} \approx 50 \Omega$ is the input impedance of oscilloscope, R_{contact} is the resistance of the wires, the picoprobes and the contacts. It is different from sample to sample and can be determined by a subtraction of the measured resistances with two wires and four wires sensing methods. For sample B, R_{contact} has a comparable resistance with R_{MTJ} , but for sample A, R_{contact} is almost zero which simplifies the calculation.

4 Thermal effects in MTJs induced by femtosecond laser pulse excitation

4.1 Introduction

The heat transport is critical in nanoscale electronic devices. Although the miniaturization from microscale to nanoscale has brought many advantages, the increased heating resulting from high current densities is still one of the drawbacks. An insufficient heat dissipation might alter or even destroy nanoscale devices. This problem is more important on the nanoscale than on the microscale since heat dissipation is different if the scale of an object is of the order of the carrier's mean free path. Meanwhile, thermal effects in spintronic devices, the field of spin caloritronics, are in current focus of worldwide research. This includes not only the spin-Seebeck effect [7, 84, 85], but also a thermally driven spin transfer torque (T-STT) effect [50], where a temperature gradient is used to switch magnetization. It may provide an alternative and more practical solution for harvesting the heat dissipated in spintronic devices.

The experimental studies on T-STT have provided first evidence in spin valve [86–88]. However, since the prediction in 2011 [10] that magnetization reversal by T-STT could be realized in an MTJ, only a few evidences of the T-STT effect in an MTJs have been reported [51–53]. One problem of these studies is the lack of knowledge of the underlying heat transport processes, resulting in a difficulty to distinguish the temperature and the temperature gradient effects on the magnetization. Thus, to better understand thermally induced magnetization reversal and heat dissipation in nanoscale structures, it is important to develop techniques capable of measuring absolute temperatures and temperature evolutions in buried nanoscale objects [89, 90], and more importantly, to separately extract the temperature gradient effect and temperature effect on the magnetization of the MTJ.

In this chapter, we first present a simple approach for the measurement of the absolute temperature in nanoscale structures with sub-nanosecond time resolution (from section 4.3 to 4.5). For this purpose, we take advantage of the temperature dependence of the MTJ resistivity. After calibrating this resistivity dependence using an

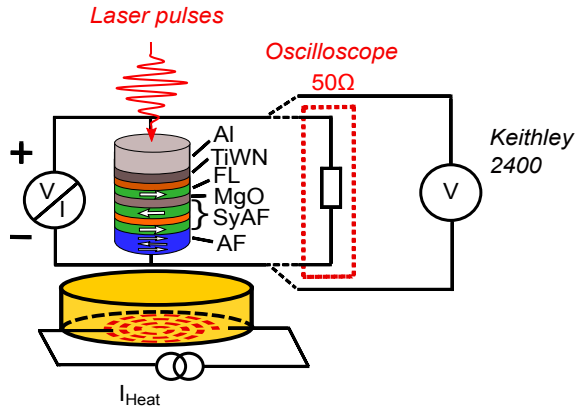


Figure 4.1: Schematic sketch of the experimental setup and MTJ sample. FL: free layer, SyAF: synthetic antiferromagnet, AF: antiferromagnet.

electric heating stage, we employ time-resolved resistivity measurements with a fast sampling oscilloscope to quantify the temperature evolution upon heating the metal contact above the MTJ by femtosecond laser pulses. The measured time dependence fits well to simulations. Furthermore, we find that our approach can also be used for the study of the tunnel magnetothermopower (TMTP). In the section 4.6, we study the temperature gradient effect on the magnetization reversal of the MTJ. We use the SyAF layer for the temperature probing. After calibrating the temperature dependence of the SyAF switching field with a heating stage, we can extract the temperature and the temperature gradient effect on the magnetization reversal of the FL during laser heating. We also estimate the magnitude of the temperature gradient effect by comparing the measurements with charge-current-induced STT.

4.2 Experimental basics

The measurement of time resolved resistivity or temperature in an MTJ after laser heating are performed on sample A, while sample B is used to study the temperature gradient effect on the MTJ. The details of the samples are described in the chapter 3.

The laser pulses used in this chapter are generated by a femtosecond Ti:sapphire oscillator with a repetition rate of 76 MHz and focused to a $1/e^2$ diameter of $8 \mu\text{m}$ on the Al layer above the MTJ. The resistance of the MTJ was characterized by the four-wire sensing method as shown in Fig. 4.1. In this scheme dc currents, I_{dc} , were supplied by a current source (Keithley 2400), which simultaneously measured the voltage for the case of time-integrated measurements. For time-resolved measurements a sampling oscilloscope (Tektronix DSA 8200, 50Ω characteristic impedance) replaced the voltmeter. All temperature calibrations of the MTJ samples were performed by an electrical heater being placed right underneath the samples allowing a temperature variation of up to 30 K above room temperature.

4.3 Voltage and temperature dependence of tunnel resistance

Figure 4.2(a) shows typical magnetoresistance loops at room temperature ($T_0 = 32.7$ °C) for different dc currents. The loops show a TMR ratio of approximately 120 % with a multi-step switching from the P to the AP state, which is due to multiple domains in the FL. The resistance in the AP state (R_{AP}) decreases with increase of bias voltage, while the resistance in the P state (R_P) shows an almost negligible bias voltage dependence (smaller than 0.1 Ω). The conductance of the AP state as a function of the applied bias voltage is plotted in Fig. 4.2(b). The fit to the curve reveals a slight asymmetry, which could result from asymmetric potentials due to surface roughness or organic impurities trapped in the MTJ [22]. It should be noted that with the model of [22], the conductance as a function of bias voltage is calculated at a certain temperature. The model does not take the influence of current-induced heating on the conductance into account. To estimate this effect we compare the sample size and dc current applied to the sample with the previous results on current-induced self heating [86]. From this comparison we estimate a constant temperature rise in our MTJ of ≈ 2 K for a current of 2 mA. For a current of 0.2 mA the self heating is expected to be reduced by a factor of 100. We will show below that such self-heating-induced temperature changes are very small compared to the constant temperature increase due to laser heating and can be neglected.

Similar TMR loops were also taken at different temperatures for $I_{dc} = 0.2$ mA, see Fig. 4.3(a). The resistance in the AP state decreases with increasing temperature. This behavior agrees well with results of MgO and AlO_x-based MTJs reported by other groups [20, 25] and can be explained by several phenomenological models, such as magnon [24, 25] and phonon [30, 91] assisted tunneling, temperature-dependent spin-polarized tunneling in combination with hopping through localized states [4, 27] or misalignment of magnetic moments in the electrodes [16, 29]. The very weak temperature dependence of the P state (changes less than 0.1 Ω) together with the bias-voltage independence of the conductance at low voltages speaks for the high quality of the MgO barriers as employed in this study [29].

The resistance differences between the P and AP states at -50 Oe and +250 Oe, respectively, as a function of the temperature for different bias currents are plotted in Fig. 4.3(b). Here, we define the resistance change as $\Delta R(T) = (R_{AP} - R_P)_T - (R_{AP} - R_P)_{T_0}$ and plot $-\Delta R$ for visualization purpose. It should be emphasized that using this difference technique, ΔR only depends on temperature-induced resistance changes in the tunnel junction, but not on resistance changes in other layers. From the data of Fig. 4.3(b), it becomes obvious that ΔR depends linearly on temperature. For different bias currents a different slope of the ΔR versus ΔT curve is obtained,

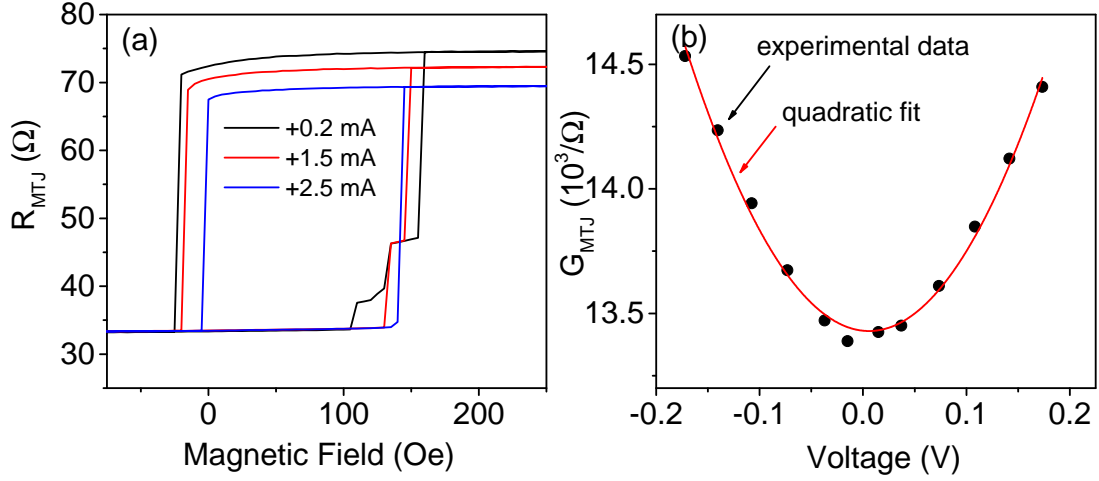


Figure 4.2: (a) MR loops measured at different currents at $T_0 = 32.7$ °C. (b) Conductance in the AP state as a function of the bias voltage. The red curve is a quadratic fit.

i.e., at a certain temperature, $-\Delta R$ is larger for $I_{\text{dc}} = 0.2$ mA (black) than for $I_{\text{dc}} = 2$ mA (red). We attribute this feature to the nonlinear dependence of the conductance on voltage as shown in Fig. 4.2(b). Linear fits to the data shown in Fig. 4.3(b) yield temperature coefficients of the resistance change of 66.3 m Ω /K and 46.8 m Ω /K for 0.2 mA and 2 mA, respectively. These coefficients are important values as they will be used to calibrate the temperature changes of the MTJ resulting from laser heating.

4.4 Time-integrated and time-resolved temperature measurements in MTJs

The laser pulses not only generate a time-dependent temperature increase across the MTJ sample, but also increase the average temperature of the MTJ due to the heat accumulation from subsequent laser pulses being separated by 13.16 ns. Figure 4.4(a) shows MR loops measured at different laser powers. The curves behave in a similar way at different temperatures as shown in Fig. 4.3(a). We note that the resistance in P state slightly decreases with increasing laser power for $+I_{\text{dc}}$ and increases with increasing laser power for $-I_{\text{dc}}$ (shown in the insets of Fig. 4.4(a)). This difference results from the thermovoltage induced by the spatial temperature gradient which occurs when the laser heats the sample from the top [92, 93]. Taking into account the contribution of the thermovoltage, the measured total voltage is given as $\pm\Delta V_{\text{C}} + \Delta V_{\text{S}}$ for $\pm I_{\text{dc}}$. Here ΔV_{C} is the potential difference resulting from the applied current and ΔV_{S} arises from the thermovoltage. We obtain a thermovoltage ΔV_{S} across the whole stack of

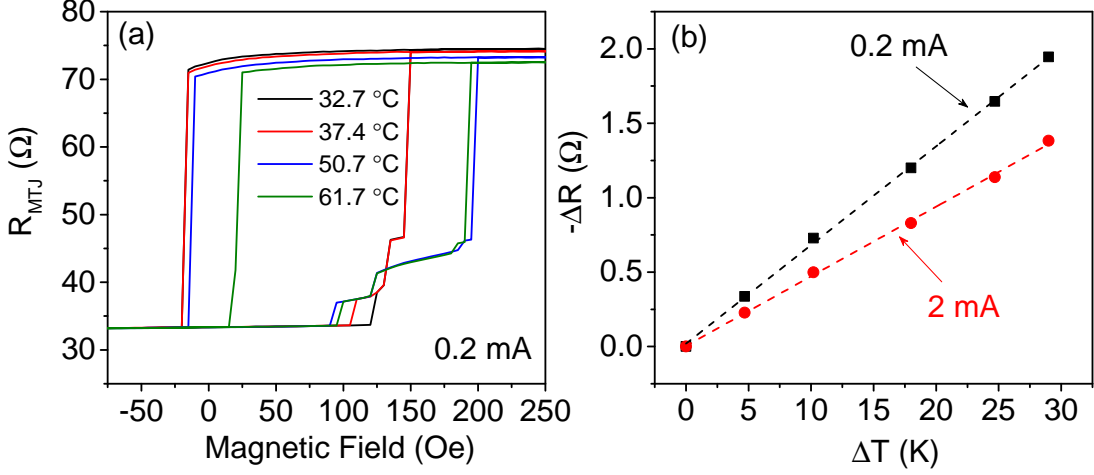


Figure 4.3: (a) MR loops for different temperatures obtained from electric heating at $I_{\text{dc}} = 0.2$ mA. (b) Resistance difference between AP and P state versus temperature change obtained from electric heating at $I_{\text{dc}} = 0.2$ mA and 2 mA.

approximately 215 μV . This is a reasonable value compared to previously measured thermovoltages generated by electric heating across the MgO tunnel barrier of several 10 μV [92, 94]. With increase of the bias current, the variation of R_{P} between both current directions decreases, which is directly obtained from straightforward application of Ohm's law. This also leads to a smaller influence of the thermovoltage component on the resistance change for larger currents I_{dc} . Taking the average of the resistance at I_{dc} the influence of the thermovoltage on the resistance change can be eliminated.

With the temperature coefficients of the resistance changes deduced from Fig. 4.3(b) we are now in a position to calculate the average temperature increases of the MTJ for different laser powers. The resulting temperature scales are shown on the right-hand side of Fig. 4.4(b) for $I_{\text{dc}} = 0.2$ mA (black) and 2 mA (red). With an average laser power of 400 mW, the average temperature of the MTJ increases by 80 K and 82 K for $I_{\text{dc}} = 0.2$ mA and 2 mA, respectively. The relative temperature difference is 2.5 %. For a conservative uncertainty estimation we double this value and obtain an uncertainty of the temperature measurements of approximately 5 %. Although the resistance change versus temperature shows a linear behavior, see Fig. 4.3(b), we note that the temperature calibration for optical heating can also be realized in case of a nonlinear, but monotonic temperature-induced resistance change.

So far we have used the temperature-dependent resistance of the MTJ to calibrate the average temperature increase occurring upon laser heating of the samples. However, to study heat transport properties, time-resolved measurements are required. To this end the time-resolved resistance change of the MTJ occurring after excitation of the

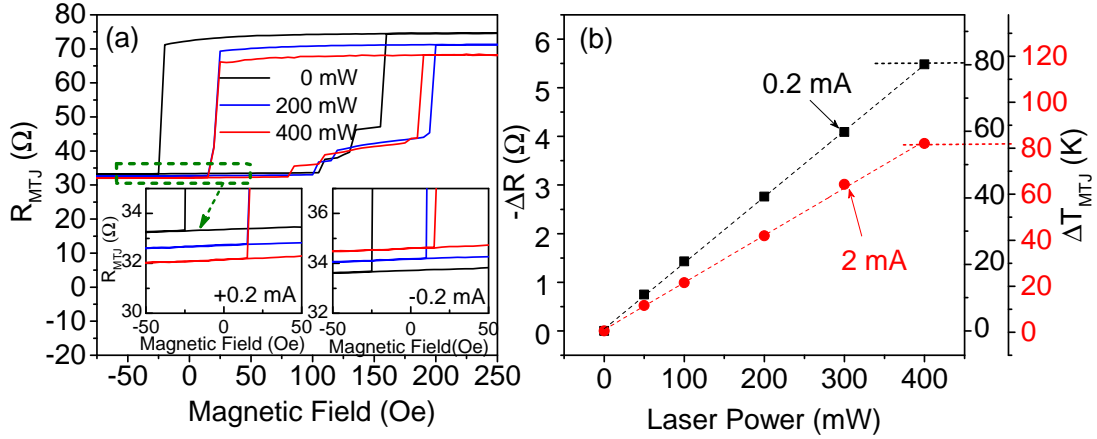


Figure 4.4: (a) MR loops for different laser powers at $I_{dc} = 0.2$ mA. The insets show the resistance change in the P state for $+0.2$ mA and -0.2 mA, respectively. (b) Resistance difference between AP and P state versus laser power at $I_{dc} = 0.2$ mA and 2 mA. The scales on the right-hand side show the corresponding temperature increase in the MTJ deduced from the ΔR versus ΔT curves in Fig. 4.3(b) at $I_{dc} = 0.2$ mA (black scale) and 2 mA (red scale).

sample with femtosecond laser pulses was detected by a sampling oscilloscope with 50Ω input impedance, see Fig. 4.1. Due to the small input impedance the measured oscilloscope signals were very small and superimposed on background signals which arose from electromagnetic coupling and thermopower. To separate signals due to resistance changes from the background signals two oscilloscope traces measured for $\pm I_{dc}$ were subtracted from each other. To reduce noise, 4000 oscilloscope traces were averaged. Using the simplified equation $\pm I_{dc} = V_{scope}/R_{scope} + V_{scope}/R_{MTJ}$ of Eq. 3.3, with $R_{scope} = 50 \Omega$ and $R_{contact} \approx 0$, we can calculate the time-resolved resistance of the MTJ, R_{MTJ} , from the time-resolved voltage, V_{scope} , measured with the oscilloscope [48].

Figure 4.5 shows a typical time-resolved resistance curve of the MTJ in the AP and P states after femtosecond laser pulse excitation. Here the laser pulse excites the sample at $t = 0$ and $t = 13.16$ ns. The resistance in the AP state continuously decreases after optical excitation and reaches its minimum at about 3.5 ns. In contrast, the resistance change in the P state is much smaller than in the AP state being in agreement with the previous dc current results and showing that the tunnel junction is the origin of the resistance change. The time-resolved measurements confirm that the resistance changes result from temperature variation due to heat diffusion from the Al layer into the underlying layers and not from ballistic transport of hot electrons. In the latter case one would expect a much faster temperature change after optical excitation [95]. When moving the focus of the laser beam away from the center of the sample, the

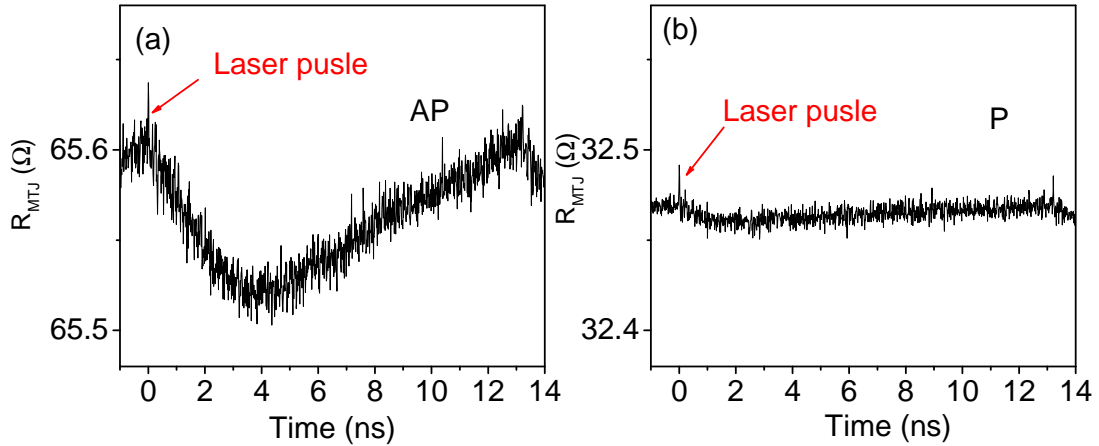


Figure 4.5: Time-resolved resistance change of the MTJ after laser pulse excitation for $I_{dc} = 2$ mA in the (a) AP and (b) P states.

resistance change drastically decreases in both magnetization states, showing that the laser is the source of heating.

We can now easily convert the time-dependent resistance curves measured in AP state into time-dependent temperature curves using the temperature coefficients of the resistance changes deduced from time-integrated measurements. The resulting time-resolved temperature changes for $I_{dc} = 0.4$ mA and 2 mA are shown in Fig. 4.6(a) and (b), respectively. The smaller of the two bias currents was chosen to be 0.4 mA instead of 0.2 mA as used in Fig. 4.3. This is because a larger current generates a larger voltage signal for a certain temperature change and consequently the signal-to-noise ratio is larger for 0.4 mA than for 0.2 mA. With increasing laser power the time-independent temperature increase due to heat accumulation and the time-dependent temperature changes gradually increases. For a laser power of 400 mW, the average temperature increases extracted from Fig. 4.6 are 78 K and 81 K for $I_{dc} = 0.4$ mA and $I_{dc} = 2$ mA, respectively. This is in excellent agreement to the time-integrated measurements shown in Fig. 4.4(b) and proves that the measured resistance changes result from the tunnel barrier. For an optical power of 400 mW, the time-dependent modulation of the MTJ temperature is 1.7 K and, thus, approximately 2 % of the time-independent temperature change. We can also deduce the absolute temperature variation across the tunnel junction using $T = \Delta T + T_0$, i.e., for a laser power of 400 mW the maximum MTJ temperature is 113.7 °C.

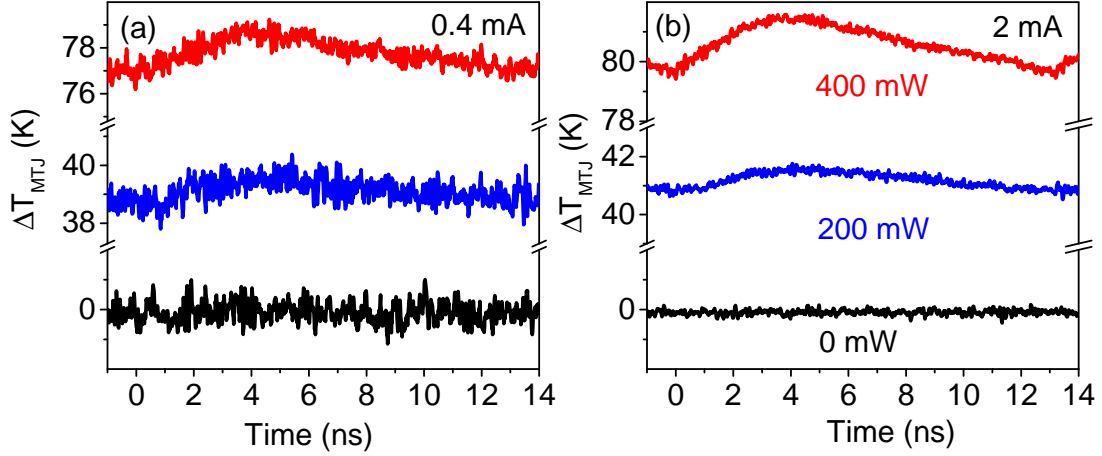


Figure 4.6: Time-resolved temperature changes for different laser powers and for (a) $I_{\text{dc}} = 0.4$ mA and (b) 2 mA, respectively. To obtain the absolute temperature the value $T_0 = 32.7$ °C has to be added to the ΔT values.

4.5 Heat transport simulations

4.5.1 Time and spatially resolved temperature variations

To validate our experimental data we have also performed time-dependent simulations of the temperature evolution, based upon the heat diffusion equation. Yet, before being able to start these finite element simulations, we have to determine the temperature evolution of the top Al layer resulting from optical excitation with femtosecond laser pulses. To this end we employ time-domain thermal-reflectance (TDTR) measurements, in which a femtosecond probe beam detects the surface temperature change of the Al layer after excitation of this layer with a pump beam. Details of the TDTR method are described in chapter 3. The measured temperature evolution of the top Al layer is shown in the inset of Fig. 4.7. This was obtained with the same laser system and an excitation power of 100 mW. After optical excitation the temperature increases by approximately 20 K and decays quickly by approximately 15 K within the following 200 ps. After that, it decays on a slow time scale before the next laser pulse arrives. The time-independent heating caused by subsequent laser pulses is 17.5 K. Extrapolating the TDTR curve to the full time period of our laser system (13.16 ns) yields an average heating of the Al layer of 19.6 K above the ambient temperature T_0 . Multiplying this value by 4 to account for the different laser power we obtain an average temperature increase of 78.4 K of the Al layer. This value is in very good agreement with the time-integrated measurements of the tunnel resistance shown in Fig. 4.4(b).

The time-dependent surface temperature of the Al layer as deduced from the TDTR

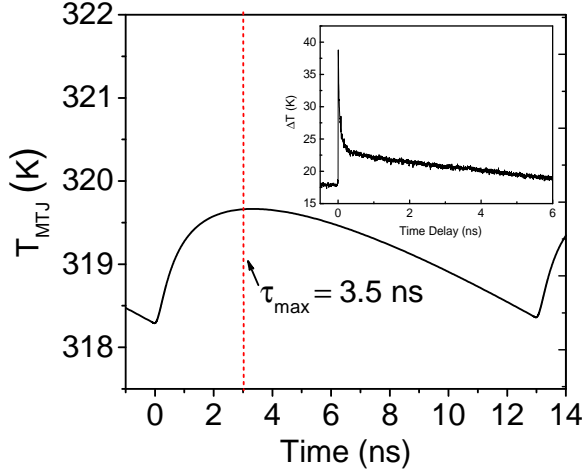


Figure 4.7: Simulation of the time-resolved temperature change of the MTJ for an optical power of 100 mW. The maximum temperature occurs 3.5 ns after laser pulse heating (dashed line). The inset of figure shows the temperature change of the Al layer measured by TDTR method used for the simulations.

Table 4.1: Thermal conductivity κ , heat capacity c_p and density ρ , for the different layers of our sample used in the simulation

Material	c_p J/(kg K)	ρ kg/m ³	κ W/(m K)
Si	700	2329	130
Al ₂ O ₃ ^a	900	3400	2
Ta	140	16400	57.5
CoFeB ^b	440	8200	87
MgO	945	3580	0.2 ^c
Ru ^b	238	12400	117
IrMn ^d	316	10181	5.7
CuN ^e	384	8960	401
TiWN ^f	160	16000	5
Al	904	2700	237

^aReference [96].^bReference [97].^cReference [98].

^dReference [99].^eThe values for Cu have been used.^fReference [100].

measurement was taken as input parameter for the simulation. Based upon this temperature evolution, the temperature variation in each layer of the whole stack was simulated as a function of time by COMSOL Multiphysics [70] using a two dimensional heat transfer model. The geometry for the simulation was taken from the cross-section of the experimentally employed sample, shown in Fig. 3.1(a). The lateral simulated width was 500 μm . The bottom temperature of the Si substrate was set to the ambient temperature. All relevant parameters such as thermal conductivity κ , heat capacity c_p and density ρ , are listed in Table 4.1. For the interfaces involving the MgO layer, the

interface resistances have been included in the effective thermal conductivity value of MgO, see also Ref [101]. For all metal-metal interfaces, we have considered a thermal conductance of 4 GW/(m² K), see Ref [100], and for all interfaces involving Al₂O₃ we have considered a thermal conductance of 100 MW/(m² K).

Figure 4.7 shows the calculated time-resolved temperature change $T_{\text{MTJ}}(t)$ of the MTJ (The MTJ stands for the average temperature of the CoFeB/MgO/CoFeB trilayer). The maximum temperature increase occurs 3.5 ns after optical excitation, and the average temperature increase is 19.0 K. These values are again in very good agreement with the experimental results. Yet, the simulated amplitude of the temperature increase is approximately 1.4 K for 100 mW optical pump power. This is more than 3 times larger than the measured temperature increase (1.7 K for 400 mW). At present we are unsure where this discrepancy results from. It could be due to the simulations, e.g., material parameters (in particular of interface heat conductivities), boundary conditions, and neglect of strain or hot electrons. Other error sources might be inaccurate parameters extracted from the experiment (such as the optical spot size) or the neglect of a spatially inhomogeneous temperature drop across the tunnel junction. In this regard, it should be emphasized that a variation of the material parameters might change the simulated temperature traces considerably. Yet, a decrease of the simulated temperature peak occurring in the MgO layer (which fits better to the experiments) will typically also lead to an additional delay of this peak (which fits worse to the experiment).

4.5.2 Time resolved spatial temperature gradients

Optical heating has been proposed as a technique to generate very large thermal gradients to induce T-STT [50]. An estimation of the temperature drop across the MgO barrier ($\Delta'T_{\text{MgO}}$) can provide input for the study of T-STT. Here, we need to pay attention to the difference between $\Delta'T_{\text{MgO}}$ and ΔT_{MTJ} . $\Delta'T_{\text{MgO}}$ is the temperature drop across the MgO barrier while ΔT_{MTJ} is the average temperature change of the MTJ (usually stands for CoFeB/MgO/CoFeB trilayer).

The simulation gives the spatial temperature distribution of each layer at any delay time after optical excitation. Figure 4.8(a) shows the temperature distribution in the two dimensional cross-section of sample at 2.5 ns after laser pulse. The temperature along the red dashed line is plotted as a function of z direction, see Fig. 4.8(b).

The temperature drop across the MgO barrier ($\Delta'T_{\text{MgO}}$) as a function of time is shown in Fig. 4.8(c) and (d). The maximum temperature drop $\Delta'T_{\text{max.MgO}}$ (2.5 ns) occurs earlier than maximum temperature $T_{\text{max.MgO}}$ (3.5 ns). The value of $\Delta'T_{\text{MgO}}$

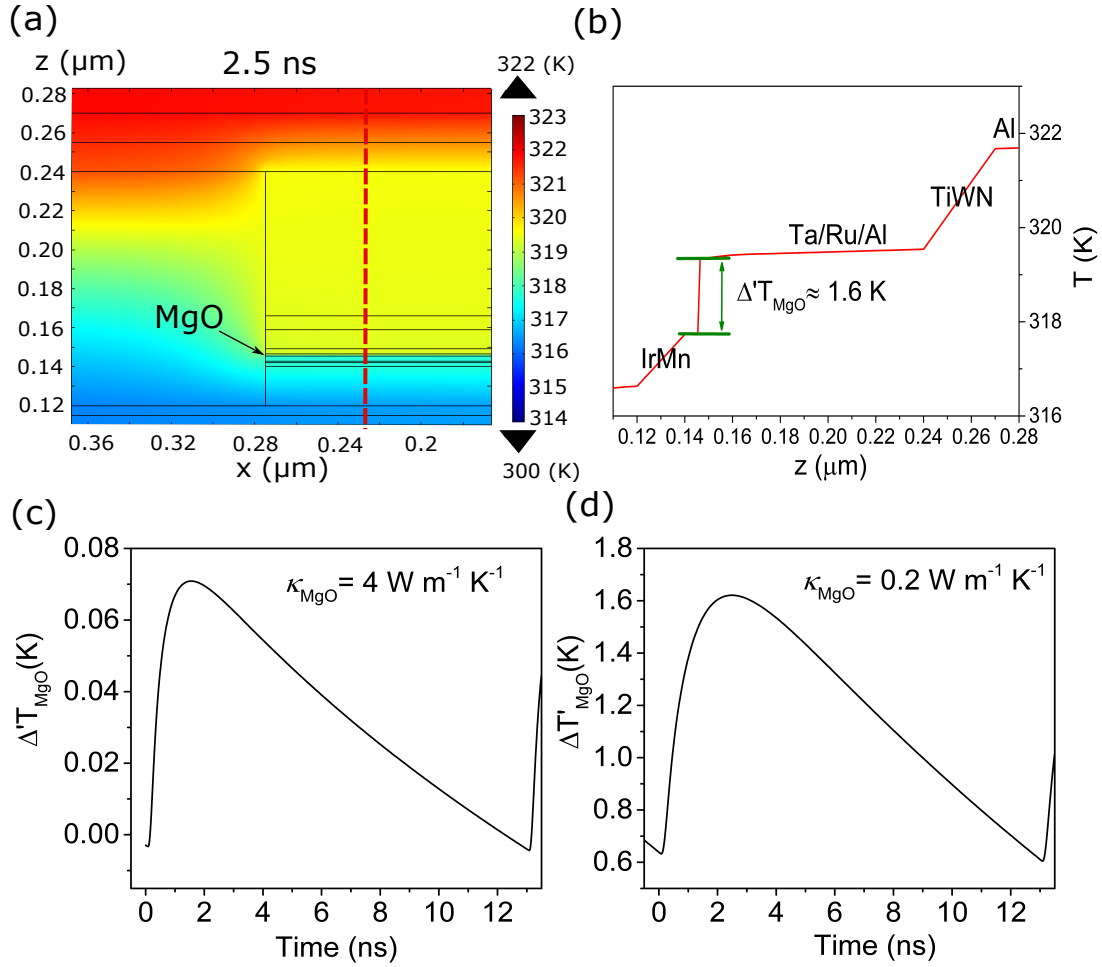


Figure 4.8: (a) Simulated temperature distribution of every layer in the two dimensional cross-section of the sample at 2.5 ns after laser pulse heating. A large temperature difference can be found between the upper and the lower interface of MgO barrier when $\kappa_{\text{MgO}} = 0.2 \text{ W m}^{-1} \text{ K}^{-1}$ is used in the simulation. (b) Extracted temperatures for each layer of the MTJ samples from the red dashed line shown in the cross-section of the sample. (c) and (d) Simulated time resolved temperature drop $\Delta T_{\text{MgO}}(t)$ across the MgO barrier after laser pulse excitation assuming a thermal conductivity of MgO of $4 \text{ W m}^{-1} \text{ K}^{-1}$ and of $0.2 \text{ W m}^{-1} \text{ K}^{-1}$, respectively.

is strongly affected by the thermal conductivity of MgO used in the simulation. A commonly used value ($\kappa_{\text{MgO}} = 4 \text{ W m}^{-1} \text{ K}^{-1}$) [96] gives a small $\Delta'T_{\text{max.MgO}}$, about 70 mK for 100 mW laser power, see Fig. 4.8(c). With a laser power of 400 mW, $\Delta'T_{\text{max.MgO}} \approx 0.28 \text{ K}$ is much smaller than the average temperature increase (80 K) and far away from predictions of the requirement ($\Delta'T_{\text{MgO}} = 6.5 \text{ K}$) for magnetization switching from the AP to the P state for an MTJ [10].

However, recently some publications argue that the thermal conductivity of MgO (down to $0.01 \text{ W m}^{-1} \text{ K}^{-1}$) is much lower due to the very small interface thermal conductance at both interfaces of MgO [98, 101]. We obtain a maximum temperature drop across the barrier $\Delta'T_{\text{max.MgO}}$ of 1.6 K (in Fig. 4.8 (b) and (d)) when a low value ($\kappa_{\text{MgO}} = 0.2 \text{ W m}^{-1} \text{ K}^{-1}$) is used (for 100 mW optical power). This temperature drop is much larger than the temperature drop estimated from the simulation in which the value of $\kappa_{\text{MgO}} = 4 \text{ W m}^{-1} \text{ K}^{-1}$ is used. In a previous study, the Seebeck coefficient of the MTJ was calculated by the expression $S = V/\Delta'T_{\text{MgO}}$ and the $\Delta'T_{\text{MgO}}$ was simulated by using $\kappa_{\text{MgO}} = 4 \text{ W m}^{-1} \text{ K}^{-1}$ [97]. However, when the interface thermal conductance of the barrier will be taken into account, the obtained S will be much smaller than before. This will simultaneously decrease the T-STT, since it is proportional to $P'S$. The large overall heating and small T-STT may be the reason why we didn't observe precession in the time resolved measurement.

Our absolute temperature measurement technique can find applications in the field of spin caloritronics, such as tunneling magnetothermopower (TMTP) measurements [92, 97, 102, 103]. Similar to the tunnel magnetoresistance effect (TMR), where the resistance R of the MTJ is dependent on the magnetization orientation of two magnetic layers, the Seebeck coefficient S is dependent on the magnetic states of the MTJ. The related tunnel magnetoSeebeck (TMS) effect or tunneling magnetothermopower (TMTP) is defined as [104]:

$$\text{TMTP} = \frac{V_{\text{TP}}(\text{AP}) - V_{\text{TP}}(\text{P})}{V_{\text{TP}}(\text{P})} \times 100\%. \quad (4.1)$$

Fig. 4.9(a) shows measurements of the laser induced thermovoltage V_{TP} as a function of magnetic field applied along the nominal easy axis of the MTJ (sample A). The thermovoltage $V_{\text{TP}}(\text{P})$ in the P state is higher than $V_{\text{TP}}(\text{AP})$ in the AP state with a maximum difference between the AP and the P state of $\Delta V_{\text{TP}} \approx 5.7 \mu\text{V}$ for the laser power of 600 mW. The laser spot size used in this measurement is about two times larger than before. Still from the previously obtained temperature coefficients of the resistance, we can estimate the average temperature increase of the MTJ, which is shown on right hand side of in Fig. 4.9(b). The average temperature increase $\Delta T_{\text{MTJ}} \approx 33 \text{ K}$ ($= T - T_0$, with $T_0 = 29.1^\circ\text{C}$) of the MTJ is corresponding to the laser

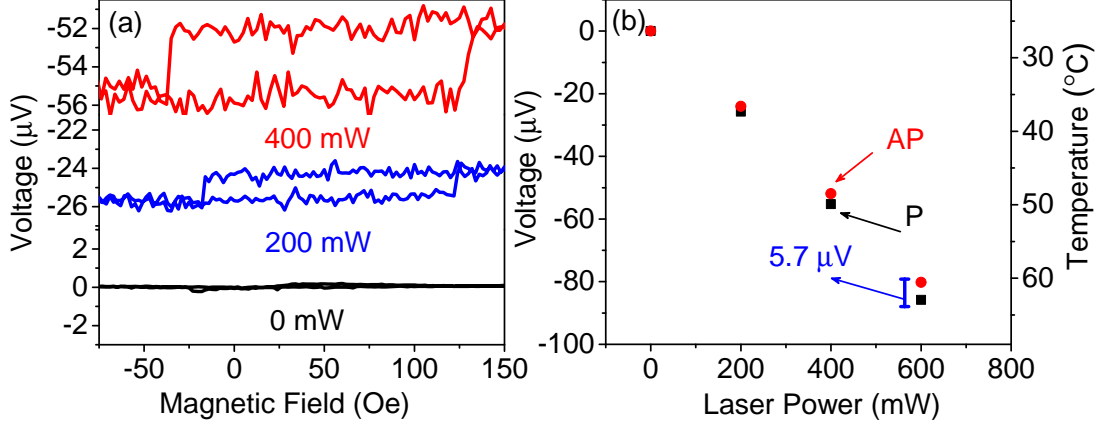


Figure 4.9: (a) Easy axis themovoltage loops under different laser heating powers. The themovoltage is measured by a high impedance nanovoltmeter. (b) The thermovoltage V_{TP} as a function of the laser power. The scale on the right-hand side shows the corresponding temperature $T = \Delta T + 29.1$ ($^{\circ}\text{C}$) of the MTJ calculated from the temperature coefficient of the resistance.

power of 165 mW in our COMSOL simulation. With this value and for $\kappa_{\text{MgO}} = 0.2$ $\text{W m}^{-1} \text{K}^{-1}$, one finds a time integrated temperature drop across the MgO barrier of $\Delta' T_{\text{MgO}} = 1.1$ K. Based on this, we can estimate a spin dependent Seebeck coefficient of the MTJ of $\Delta S = \Delta V_{\text{TP}} / \Delta' T_{\text{MgO}} = 5.2$ $\mu\text{V K}^{-1}$, which is in agreement with the value recently obtained in the literature [101]. In this measurement, to obtain the ΔS , the key issue is to obtain the $\Delta' T_{\text{MgO}}$, which depends on the laser power, laser spot and position. But the local temperature of MTJ linearly depends on the heat deposited above MTJ, as shown in Fig. 4.4(b). Thus, in the case of the same sample and the same laser excitation source, whenever the local temperature of the MTJ is determined, we can derive the $\Delta' T_{\text{MgO}}$ based on the simulation.

4.6 Temperature gradient effects

In the previous section, measurements were carried out on the MTJ with in-plane magnetic anisotropy. $\Delta R(T)$ was used to determine the local temperature of MTJ, but this method is invalid for some samples, such as Sample B. In this sample, the FL is quite thin and it has an out of plane magnetic anisotropy which speaks for high sensitivity to the STT effect. Hence the sample should also be suitable to study thermally induced STT (T-STT) effect. The laser pulses heat up the MTJ and create a large temperature gradient or temperature drop across the MgO barrier (several Kelvin). Such a large temperature gradient could affect the magnetization reversal of the MTJ.

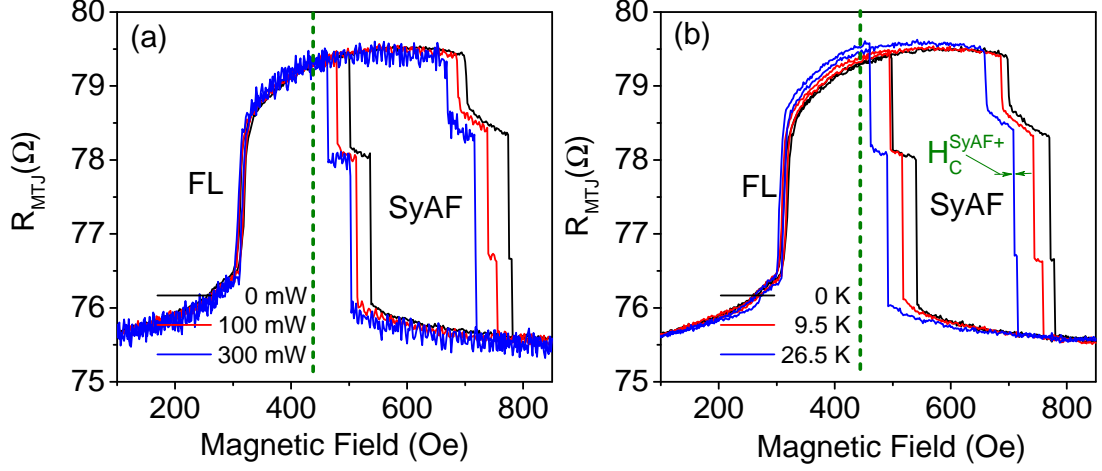


Figure 4.10: (a) MR loops for different laser powers at $I_{\text{dc}} = 0.05$ mA. (b) MR loops for different electric heating temperature at $I_{\text{dc}} = 0.05$ mA. The loop on the left side of dashed line shows the magnetization switching of of the FL and the loop on the right side shows switching of the SyAF layer.

Figure 4.10 shows the temperature dependence of MR loops of sample B when a magnetic field is applied along the defined easy axis of the RL at different (a) laser heating powers and (b) electric heating temperatures, respectively. The major resistance loop on the right side of the green dashed line corresponds to the magnetization reversal of the SyAF (RL) and the minor loop (left) corresponds to the magnetization reversal of the FL. Since ΔR is almost independent of the temperature, we can not use $\Delta R(T)$ to measure the local temperature for this sample. However, as it is shown in Fig. 4.10(b), the major MR loop has a strong dependence on the temperature. Similar results can be found under the laser heating, see Fig. 4.10(a). Thus, we can use the temperature dependence of the switching field of the SyAF for characterizing the local temperature of the MTJ. A small detection current of $I_{\text{dc}} = 0.05$ mA (5×10^4 A/cm²) is applied to measure the MR loop. Thus, the charge-current-induced STT effect and a self-heating effect on the magnetization reversal of the FL can be safely excluded. Therefore, by taking advantage of the temperature dependence of the switching field of the SyAF, we might be able to separately extract the temperature gradient effect and the temperature effect on the magnetization reversal of the FL.

Figure 4.11 shows switching field change $-\Delta H_C^{\text{SyAF+}}$ of the SyAF layer versus laser heating powers and electric heating temperature. With a linear fit to $-\Delta H_C^{\text{SyAF+}}(T)$ in Fig. 4.11, the temperature coefficient η of the switching field change can be calculated, $\eta = -\Delta H_C^{\text{SyAF+}}/\Delta T_{\text{MTJ}} \approx 2.43$ Oe/K. With this value, one can estimate the average temperature increase (ΔT_{MTJ}) of the MTJ during the laser heating. The calculated ΔT_{MTJ} are 10.1 K and 25.5 K for the laser power of 100 mW and 300 mW, respectively.

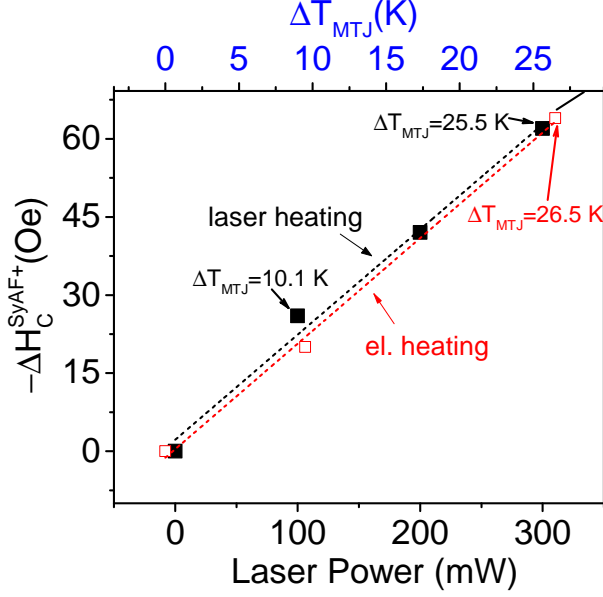


Figure 4.11: Switching field changes of SyAF ($-\Delta H_C^{SyAF+}$) versus laser power and electric heating temperature at $I_{dc} = 0.05$ mA when the magnetization switches from the AP to the P state. The scale on the top shows the corresponding temperature increase in the MTJ for different laser heating powers deduced from the electric heating result.

Now, we are able to study the temperature gradient effect on the switching field of the FL during laser heating.

Figure 4.12 shows MR loops of the FL for (a) electric heating and (c) laser heating. During electric heating, the switching field of the FL shifts about 7 Oe to lower magnetic fields when the average temperature of the MTJ increases by 26.5 K. However, during optical heating, the switching field only shifts by 3 Oe to lower magnetic fields when the laser power increases from 0 mW to 300 mW. With 300 mW laser heating power, the average temperature increases by 25.5 K which is deduced from Fig. 4.11. A temperature difference of 1 K in the MTJ can not be the reason for such a large switching field difference of the FL between laser heating and electric heating. Additionally, it can not be due to a spin polarized charge current induced by a thermalvoltage, see Fig. 4.9(a), since this current is too small (a few μA). Therefore, the difference most probably stems from a T-STT effect or a magnetoelastic effect [54] (stress) induced by the temperature gradient. The following explanation advocates to the T-STT effect, since the RL is hotter than the FL, the majority spins of the RL accumulate into the FL, which favor the P state. The T-STT makes it easier for the magnetization of the FL to switch from the AP to the P state and leads to an additional shift of the switching field (≈ 4 Oe) to higher magnetic fields. We also observe a similar shift in the switching field of the FL when its magnetization switches from the P to AP the state. Such behavior is not typical for STT effect on the MTJ with in plane magnetic anisotropy, but it may occur for the FL with out-of-plane magnetic anisotropy. Here, we will not go into detail of possible magnetoelastic effects, which will be discussed in chapter 6.

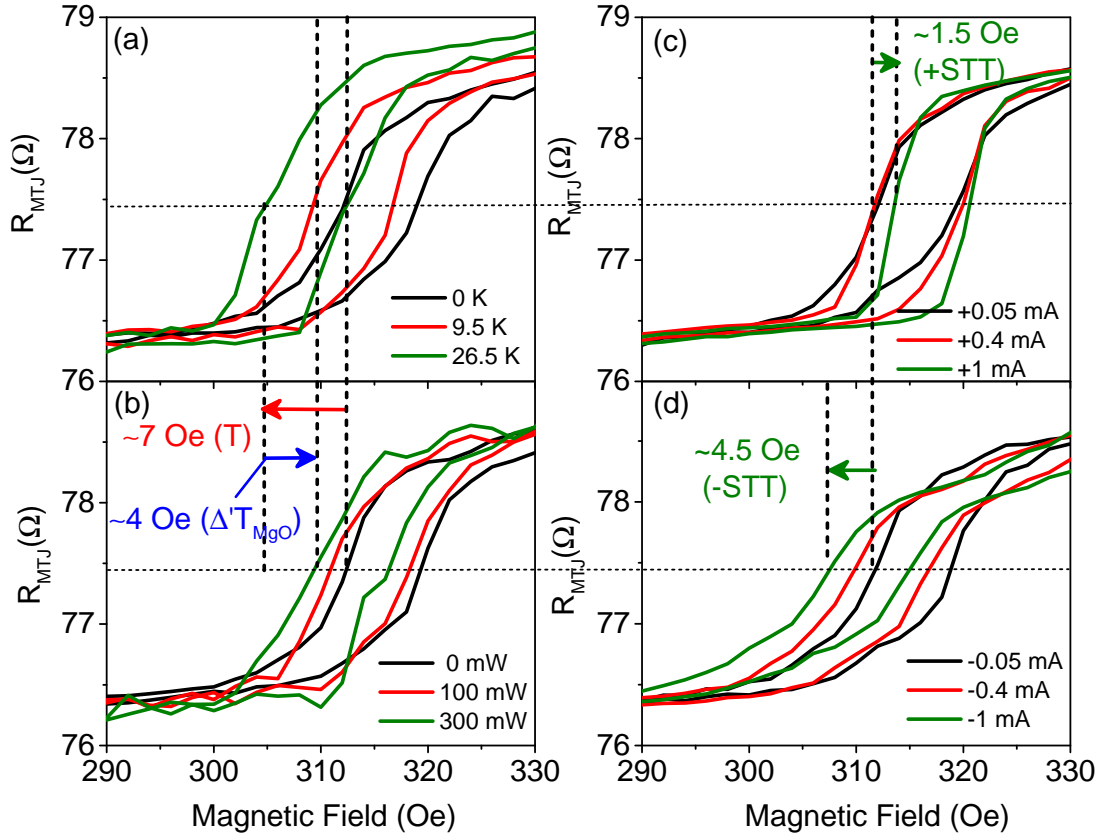


Figure 4.12: The two figures on the left side show MR loops of the FL measured at different (a) temperatures and (b) laser heating powers at $I_{\text{dc}} = 0.05$ mA. While in (a) only a temperature effect occurs, in (b) a temperature and a temperature gradient effect might be present. The right two figures show MR loops of the FL measured at different bias currents (c) positive bias current (+ electrons flow from the RL to the FL) and (d) negative bias current (-). The arrows represent the shift of the switching field due to effects of the temperature T , temperature gradient ΔT_{MgO} and charge induced spin transfer torque STT.

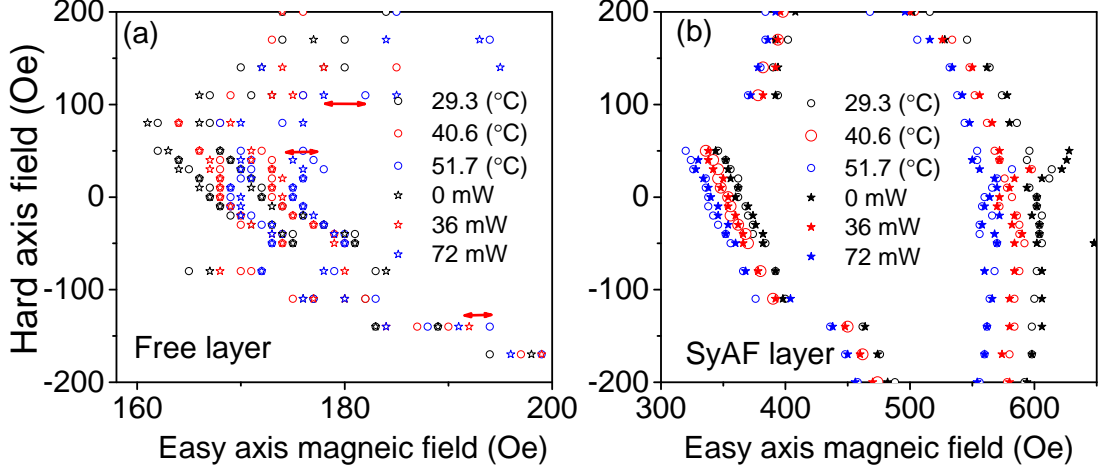


Figure 4.13: The measured astroids of the (a) the FL and (b) SyAF as a function of the laser heating power and the electric heating temperature, respectively.

To study the strength of the temperature gradient effect on the magnetization reversal, we make a comparison measurement with conventional charge-current-induced STT effect. Depending on the polarity of the applied charge current, STT makes the MTJ either favor the AP or the P state [38]. We measured MR loops at various bias currents, as shown in Fig. 4.12 (c) and (d). For a positive charge current (electrons flow from the RL to the FL), the switching field shifts to a higher magnetic field, which is similar to the effect of the T-STT favoring the P state. The switching field shifts about 1.5 Oe with a current density of $I_{dc} = +1 \times 10^6$ A/cm², see Fig. 4.12 (c), which means that the temperature gradient effect (with a shift of 4 Oe) is as large as the STT created by a charge current density of 10^6 A/cm² in the MTJ.

The result looks quite promising, however, to address the origin of our observation, we need to measure the angle dependence of the temperature gradient effect on the magnetization reversal of the MTJ. This can be accomplished with the astroid of the magnetic layer as described in chapter 3. Figure 4.13 shows the measured astroid of the FL and SyAF layer as a function of laser power and temperature for another MTJ sample. Now the astroid of the SyAF is used for temperature probing. The good overlap of the measured astroids of the SyAF (Fig. 4.13(b)) obtained from the laser heating and electric heating shows that the MTJ has the same temperature in the two heating cases. If there is a large T-STT effect, for this sample with out of plane magnetic anisotropy, we should observe a difference in the switching fields of the FL between two heating cases. This should occur in a large range of bias magnetic fields which are applied along the hard axis of the MTJ. However, if we look at the bias magnetic field range from -50 to 50 Oe, where the switching field of the FL can be easily determined, only little difference of the switching field between laser and electric

heating (red arrow) is found, as shown in Fig. 4.13(a). Thus, we may attribute the difference between the two heating cases to the changes in the magnetic anisotropy of the FL due to the stress or strain induced by the temperature gradient.

4.7 Conclusions

In this chapter, we have focused on thermal effects in the MTJ induced by laser pulse heating. We took advantage of the temperature dependence of the resistance of the MTJ as detected by a fast sampling oscilloscope. After calibrating the measurement setup using steady-state electric heating, we were able to quantify temperature changes in the MTJ induced by femtosecond optical heating of the metal contact lying several 100 nm above the MTJ. We found that a femtosecond pulse train with an average power of 400 mW and a repetition rate of 76 MHz leads to a constant temperature increase of 80 K and a temporally varying temperature change of 2 K in the MTJ. The maximum temperature change in the MTJ occurs 3.5 ns after the femtosecond laser pulses hit the metal contact, which is supported by simulations. The simulated maximum difference across the MgO barrier ΔT_{MgO} is about 1.6 K for 100 mW laser power when the interface heat conductance is taken into account. We investigated the temperature gradient effect on the magnetization reversal of the MTJ. By taking advantage of the temperature dependence of the switching field of the SyAF, we characterize the average temperature rise of the MTJ during laser heating. Thereby the temperature gradient and the temperature effect on the switching field of the FL could be separated. We observed an additional 4 Oe switching field change of the FL layer in the laser heating compared to the electric heating when the MTJ has the same temperature. Comparing this result with the switching field change of the FL caused by conventional charge induced STT, we found that the temperature gradient effect or T-STT in our case could be as large as the STT induced by a charge current density of 10^6 A/cm². However, other effects like magnetoelastic effect can not be ruled out for being responsible for the switching field changes.

5 The MTJ as a temperature sensor

5.1 Introduction

Due to the fast miniaturization of electric device, heat dissipation and heat transport are important and even sometimes critical parameters for practical applications and fundamental research [89]. This is mainly because electric devices with dimensions below 100 nm can be easily damaged due to low efficiency of heat dissipation. Additionally, the exact knowledge of heat dissipation and the discrimination between temperature and temperature gradients is crucial for understanding new physical phenomena [85]. Therefore, a strong drive exists to exploit novel nanoscale temperature sensors featuring a high spatial and temporal resolution, a high sensitivity and stability, and a large operating temperature range.

The magnetic tunnel junction (MTJ) is a complex magnetic system with several magnetic layers involved. It features a large variety of physical phenomena occurring in and between the different layers as a response upon external perturbations. Most applications take advantage of the dependence of the tunnel magnetoresistance (TMR) on the magnetization direction of the MTJ's free layer. This dependence has been widely used for sensor applications, such as magnetic field or strain sensing, due to its high sensitivity and stability, low energy consumption, and small size [20, 56, 105]. However, so far, the MTJ has only been employed as a temperature sensor in a few studies [106–108] and a systematic investigation and comparison of the different effects enabling temperature measurements using an MTJ is missing.

In this chapter, we present a comprehensive study of using the MTJ as a temperature sensor as exemplarily depicted in Fig. 5.1(a), capable of performing time-resolved and quantitative temperature measurements in buried nanostructures. Three different properties of the MTJ will be evaluated for this purpose: the tunnel resistance, the coercivity of the free layer, and the coercivity of the synthetic antiferromagnet (SyAF). We demonstrate temperature measurements using the MTJ for the case in which the metal contact above the MTJ is heated with femtosecond laser pulses and show that the temperatures obtained with the three different techniques are consistent with each other. Additionally, we discuss and compare the sensitivity, operability, and accuracy

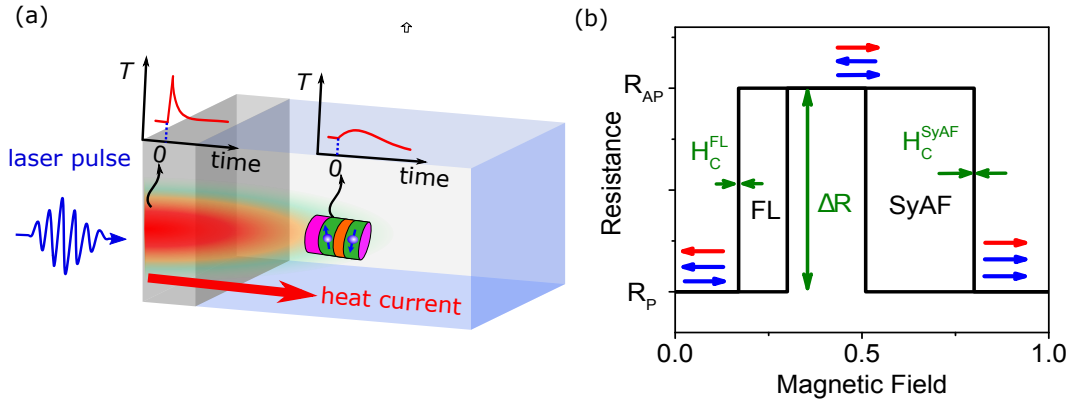


Figure 5.1: (a) Schematic sketch of the MTJ as a buried nanoscale temperature sensor. (b) Typical MR loop with a magnetic field applied along the easy axis of the MTJ. The minor loop corresponds to the magnetization reversal of the free layer (red arrow), whereas the major loop corresponds to the magnetization reversal of the reference layer in the SyAF (upper blue arrow). The green arrows mark the three most important properties of the MR loop: tunnel resistance change ΔR , coercivity of the FL H_C^{FL} , and coercivity of the reference layer of the SyAF H_C^{SyAF} .

of these three methods.

The remainder of this chapter is structured as follows. In section 5.2, the experimental setup is presented. The main results of the MTJ temperature sensor based the tunnel resistance has been described in chapter 4, we give a briefly discussion in section 5.3. In section 5.4, temperature measurements based on the coercivity of free layer are described and compared to the temperature measurements employing the tunnel resistance of the MTJ. Section 5.2 focuses on temperature measurements based on the coercivity of the SyAF. In this section we also give a comparison to temperature measurements based on the coercivity of free layer. Finally, In section 5.6, the pros and cons of all three techniques are discussed and conclusions are given.

5.2 Experimental basics

Figure 5.1(b) shows a typical magnetoresistance (MR) loop for a magnetic field being applied along the easy axis of the MTJ with an in plane magnetic anisotropy. The green arrows mark the three most important properties of the MR loop. First, the change of the tunnel resistance (ΔR), which occurs upon switching of the magnetization orientation of the free layer (FL, red horizontal arrow). The MTJ is in a low (R_P) and high (R_{AP}) resistance state when the free layer magnetization is parallel (P) and

antiparallel (AP), respectively, to the reference layer of the SyAF (upper blue arrow). Second, the magnetic field at which the P state switches to an AP state, yields the coercivity of the FL (H_C^{FL}). This switching determines the minor resistance loop (left loop) in Fig. 5.1(b). Third, the magnetic field (H_C^{SyAF}) at which the reference layer of the SyAF switches. This switching is determined by the inter-layer exchange coupling of the two layers comprising the SyAF (two blue arrows) and leads to the major resistance loop (right loop). All three properties (R , H_C^{FL} and H_C^{SyAF}) depend on the temperature and, thus, enable the use of the MTJ as a thermometer as described in section 5.3 to 5.5.

5.3 Temperature sensor based on the tunnel resistance

The most fascinating property of the MTJ is the high sensitivity of its tunnel resistance to an external stimulus. The temperature dependence of the resistance $R(T)$ can be described with the spin-polarized direct elastic tunnel model [16,109]:

$$R(T) = R_T [1 + P_1(T)P_2(T) \cos \varphi]^{-1}, \quad (5.1)$$

where φ is the magnetization angle between the FL and the reference layer, $P_{1,2}(T)$ denote the spin polarization of the FL and the reference layer, and $R_T = R(0)CT \sin(CT)$, where $R(0)$ is the resistance at 0 K and C is a constant. Although in Eq. 5.1, the resistance has a nonlinear temperature dependence over a wide temperature range, it is easy to see that in a restricted temperature range close to room temperature, R depends linearly on T [20, 25, 110]. Taking advantage of this temperature dependence the MTJ can be employed as a temperature sensor with high spatial and temporal resolution. Since this technique has been demonstrated chapter 4 [107], we only briefly describe measurement results. For these measurements, sample A with dimensions of 150 nm \times 500 nm has been used.

Figure 5.2 shows the temperature-dependent resistance change ΔR versus the electric heating temperature and the laser excitation power. Here ΔR is defined as $\Delta R(T) = (R_{\text{AP}} - R_{\text{P}})_T - (R_{\text{AP}} - R_{\text{P}})_{T_0}$, where R_{AP} and R_{P} is the resistance of the MTJ in the AP and P state, respectively, and T_0 denotes room temperature. A linear fit to the electric heating data allows us to calculate the temperature coefficients of the resistance $\alpha = -\Delta R/\Delta T$. For the two different bias currents of 0.2 mA and 2 mA we obtain values for α of 66.3 m Ω /K and 46.8 m Ω /K, respectively. With these values, we are able to calculate the average temperature increase of the MTJ for different laser excitation powers.

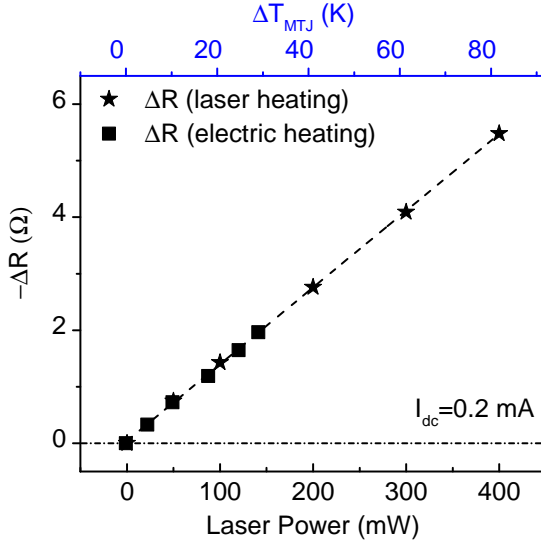


Figure 5.2: Resistance change ΔR of the MTJ as a function of laser power (bottom scale) and as a function of temperature change due to electric heating (top scale). Due to the overlap of the curves, the upper axis directly shows the temperature rise of the MTJ for different laser excitation powers.

The method also enables time-resolved temperature measurements after replacing the voltmeter with a fast sampling oscilloscope. These dynamic measurements are in very good agreement with finite element temperature simulations [107]. The biggest advantage of this method for temperature measurements is that it constitutes a quick, simple, and practical method allowing for both, time-integrated and time-resolved measurements. A high TMR and low tunnel resistance with a large temperature dependence are beneficial for temperature characterization. Since the tunnel resistance is quite sensitive to the current amplitude, the method may not work well when using small current amplitudes (< 0.1 mA) in complex electromagnetic environments.

5.4 Temperature sensor based on the coercivity of the free layer

In MTJ-based magnetoresistive random access memory (MRAM) devices, coercivity is an important figure of merit. The temperature dependence of the coercivity has been well studied for MTJs having an in-plane and out-of-plane anisotropy [41,111,112]. The temperature effect influences magnetization and magnetocrystalline anisotropy leading to coercive field changes of the free layer. These effects enable thermally assisted [99] or even thermally induced [112] magnetization switching. In this section, the temperature-dependent coercivity of the FL, H_C^{FL} , will be employed as a temperature sensor.

The temperature dependence of $H_C^{\text{FL}}(T)$ with uniaxial anisotropy can be described as following [113–115]:

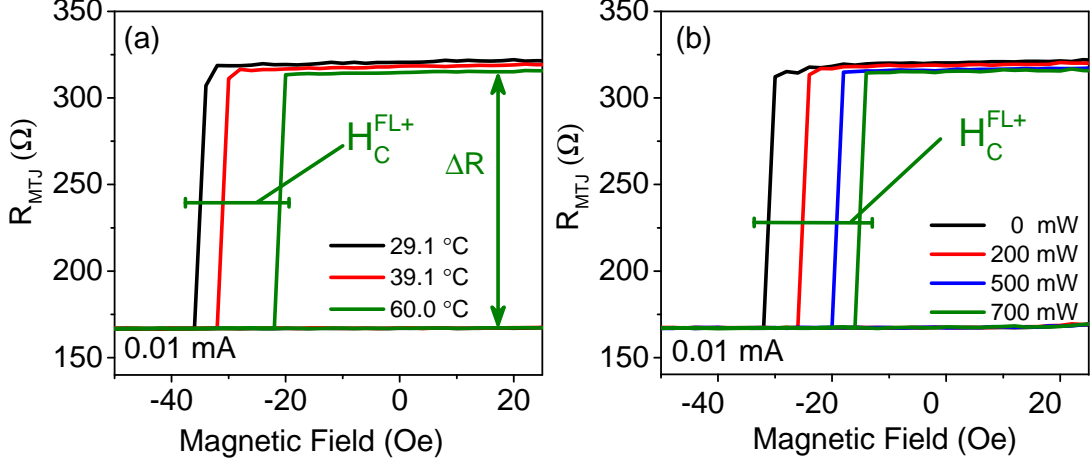


Figure 5.3: (a) MR loops with the magnetic field applied along the easy axis for different temperatures obtained from electric heating at $I_{\text{dc}} = 0.01$ mA. (b) MR loops for different laser powers at $I_{\text{dc}} = 0.01$ mA. Note that the resistance change due to a thermovoltage has been eliminated in (b).

$$H_C(T) = H_a \left[1 - \left(\frac{k_B T \ln(t/t_0)}{E_0} \right)^{1/2} \right], \quad (5.2)$$

where H_a is the anisotropy field at 0 K, k_B is the Boltzmann constant, E_0 is the energy barrier, t_0 is a time constant ranging between 10 ps and 1 ns, and t is the time necessary to overcome the energy barrier at the temperature T .

Measurements have been performed on sample A (MTJ stack dimensions $50 \text{ nm} \times 50 \text{ nm}$), which shows a single domain switching behavior. In contrast to the previous section, we used a smaller detection current $I_{\text{dc}} = 0.01$ mA for the measurement of MR loops, mainly to avoid effects of spin transfer torque on the coercivity. To analyze the temperature dependence of the switching field, we define the coercivity change as $\Delta H_C^{\text{FL}\pm} = (H_C^{\text{FL}\pm})_T - (H_C^{\text{FL}\pm})_{T_0}$, where \pm refers to the switching of the magnetization from AP to P (+) and vice versa (-).

In Fig. 5.3(a) and (b) we plotted MR loops as a function of temperature and laser power, respectively, showing the switching from AP to P ($\Delta H_C^{\text{FL}+}$). Note that in Fig. 5.3(b), a resistance change induced by a thermovoltage (due to the spatial temperature gradient of the laser heating) has been eliminated by shifting MR loops to the same resistance value in the P state. It is obvious that both ΔR and ΔH_C^{FL} monotonically change with increasing temperature.

The dependence of $\Delta H_C^{\text{FL}+}$ and ΔR on electric heating temperature and laser excitation power, resulting from Fig. 5.3(a) and (b), are shown in Fig. 5.4. Linear fits to $\Delta R(T)$ (black line) and $\Delta H_C^{\text{FL}}(T)$ (red line) yield temperature coefficients of the

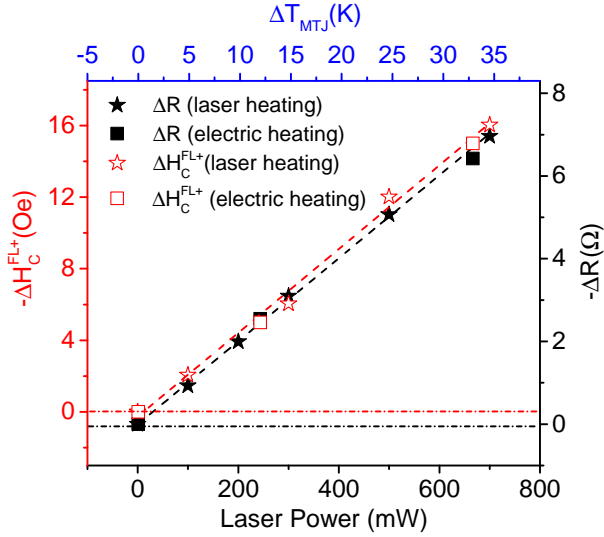


Figure 5.4: Coercivity change $\Delta H_C^{\text{FL}+}$ (red) and resistance change ΔR (black) of the MTJ's free layer as a function of laser excitation power (bottom scale) and temperature change due to electric heating (top scale). For clarity, the zero values of the right and left axis are vertically shifted. Otherwise most of the data points would perfectly overlap diminishing the readability. Due to the identical slope of all curves, the upper axis directly shows the temperature rise of the MTJ for different laser excitation powers.

resistance and the coercivity of 194 mΩ/K and 458 mOe/K, respectively. The good agreement between the measurement values of $\Delta R(T)$ and $\Delta H_C^{\text{FL}}(T)$ and the fit curves justifies the linear fit in the temperature range from 290 K to 340 K. Yet, we note that in another temperature range a fit based upon Eq. 5.2 might be more appropriate.

With the temperature coefficients of the resistance and the coercivity deduced above, we can calculate the average temperature increases of the MTJ for different laser excitation powers. The upper axis of Fig. 5.4 directly converts the laser excitation power of the lower axis into a temperature increase of the MTJ. For a laser excitation power of 700 mW, the average temperature of the MTJ increases by 33.1 K and 35.0 K as obtained from the $\Delta R(T)$ and $\Delta H_C^{\text{FL}}(T)$ values, respectively. This good agreement between the two methods validates the measurements and shows that both methods can be used for quantitative temperature measurements.

At the end of this section we comment on the measurement accuracy of the coercivity values ΔH_C^{FL} . The coercivity does not always change monotonically with temperature, in particular, when the sample is not perfect, e.g., does not have an ideal uniaxial anisotropy or spatially uniform magnetization. This is demonstrated in Fig. 5.5(a). The MR loops were measured in a situation where the MTJ is supposed to have the same temperature for both, electric and laser heating. Yet, a coercivity difference of 10 Oe between two heating cases is obtained. This difference is due to the magnetization of the FL, which rotates with the external magnetic field but might be pinned at the edges or defects of the FL. Repeated measurements under identical conditions may not solve

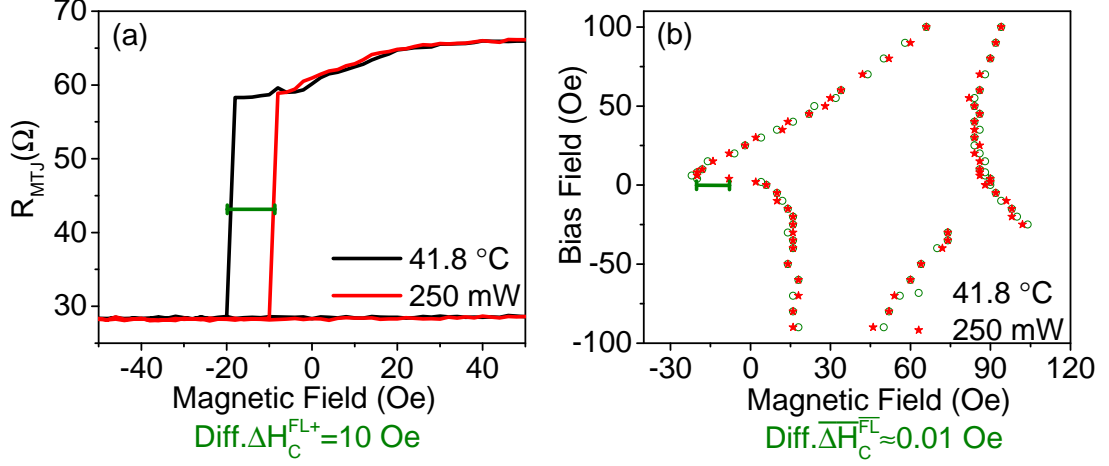


Figure 5.5: (a) MR loops and (b) Stoner-Wohlfarth astroids measured for electric and laser heating both of which are supposed to lead to the same temperature. For a certain magnetic field angle $\Delta H_C^{\text{FL}+}$ obtained from both heating conditions might be different (a), yet, averaging over the magnetic field angle nearly identical average values $\overline{\Delta H_C^{\text{FL}}}$ are obtained (b). The terms Magnetic Field and Bias Field denote magnetic fields applied along the easy and hard axis of the MTJ, respectively.

this problem. To improve the accuracy, one solution is to use the Stoner-Wohlfarth astroid for temperature probing [36, 38, 111, 112]. The astroid shows the switching points extracted from MR loops which are measured for magnetic field sweeps along the easy axis of the MTJ at various constant magnetic fields applied along the hard axis, see Fig. 5.5(b).

We obtain a very good overlap of the measured astroids for the two heating cases. In fact, the averaged difference $\overline{\Delta H_C^{\text{FL}}}$ of the astroid shift between electric and laser heating is only 0.01 Oe. Here, ΔH_C^{FL} is defined as $\Delta H_C^{\text{FL}}(T) = (H_C^{\text{FL}+} + H_C^{\text{FL}-})_T - (H_C^{\text{FL}+} + H_C^{\text{FL}-})_{T_0}$. Thus, for nonideal samples, $\overline{\Delta H_C^{\text{FL}}}$ can be taken as a quantitative and accurate measure of the temperature of the MTJ.

5.5 Temperature sensor based on the coercivity of the synthetic antiferromagnet

Two ferromagnetic layers can be coupled through a thin non-magnetic spacer, which is often made of Ru. Depending on the thickness of Ru, the coupling strength oscillates between ferromagnetic and anti-ferromagnetic. This behavior is described by the Ruderman-Kittel-Kasuya-Yosida (RKKY) model [33]. In the MTJs employed in this

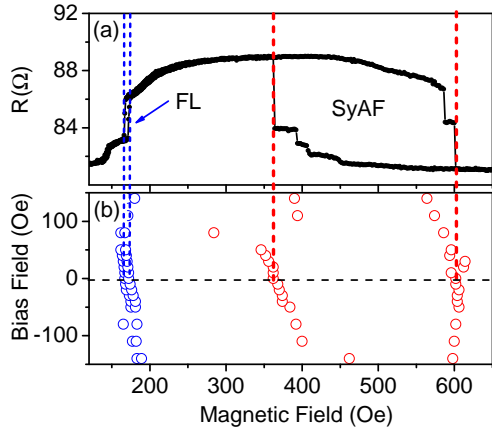


Figure 5.6: (a) Measured MR loops for the magnetic field applied along the easy axis of the MTJ at $I_{dc} = 0.05$ mA. (b) Switching points for the FL and the SyAF extracted from MR loop measurements at various magnetic fields applied along the hard axis, referred to as Bias Field in the figure.

study, the Ru thickness is chosen such that an antiferromagnetic inter-layer exchange coupling occurs between the two ferromagnetic layers; this trilayer system is referred to as synthetic antiferromagnet (SyAF).

The switching field H_C^{SyAF} of the reference layer of the SyAF, compare with Fig. 1(b), is proportional to the RKKY coupling J , which in turn depends on the temperature [33, 108, 116]:

$$H_C^{\text{SyAF}}(T) \propto J(T) = J_0 \frac{T/T_0}{\sinh(T/T_0)}, \quad (5.3)$$

where $T_0 = \hbar v_F / 2\pi k_B t$ is the characteristic temperature, v_F is the Fermi velocity at T_0 , t is thickness of the Ru layer, and J_0 is the coupling strength at T_0 . Wiese *et al.* evaluated the characteristic temperature to be 150 K (corresponding to a Fermi velocity of 1.15×10^5 m/s) for a SyAF consisting of a CoFeB/Ru/CoFeB trilayer [116]. The low value of v_F gives rise to a strong temperature dependence of the coupling strength in Ru-based antiferromagnetic systems. Although Eq. 5.3 is nonlinear, it can be approximated by a linear function within a small temperature range of approximately 100 K [116].

In a previous publication, Chavent *et al.* employed the dependence of $H_C^{\text{SyAF}}(T)$ to quantitatively probe the local temperature of an MTJ in response to the application of large charge currents [108]. We adopt a similar technique for the quantitative measurement of local temperatures in response to laser heating. For these measurements, sample B has been used. Figure 5.6(a) shows typical MR loops measured for an in-plane magnetic field applied along the easy axis of the MTJ at $I_{dc} = 0.05$ mA. As already described in the introduction, the major and minor loops correspond to the magnetization switching of the SyAF's reference layer and the FL, respectively. The multi-step switching is due to multiple domains in the sample.

Subtracting the two MR loops obtained from magnetic field sweeps from 700 Oe to

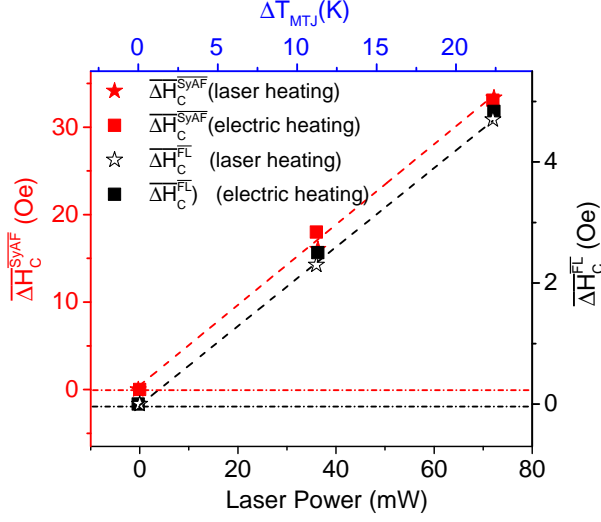


Figure 5.7: Averaged coercivity changes $\overline{\Delta H_C^{FL}}(T)$ (black) and $\overline{\Delta H_C^{SyAF}}(T)$ (red) as a function of laser power (bottom scale) and temperature change due to electric heating (top scale). For clarity, the zero values of the right and left axis are vertically shifted. Due to the identical slope of the measurements the upper axis directly shows the temperature rise of the MTJ for different laser excitation powers.

100 Oe and from 100 Oe to 700 Oe, we can easily extract the magnetization switching points of the different magnetic layers. The dots in Fig. 5.6(b) show these switching points for the FL (blue) and the SyAF (red). Similarly to the temperature measurements based on the astroid of the FL, we will now employ the magnetization switching points of the SyAF for temperature probing.

Since sample B has an out-of-plane magnetization of the FL, the extracted switching points do not look like an astroid as it is the case for sample A with an in-plane uniaxial anisotropy. Therefore we consider both magnetization switching points (from AP to P and from P to AP) in the data analysis. We define the temperature dependent coercivity of the FL ΔH_C^{FL} as above and the temperature-dependent coercivity of the SyAF as $\Delta H_C^{SyAF}(T) = (H_C^{SyAF+} + H_C^{SyAF-})_T - (H_C^{SyAF+} + H_C^{SyAF-})_{T_0}$. With this definition the coercivity changes averaged over the different magnetic fields applied along the hard axis (-50 Oe to 50 Oe and -100 Oe and 100 Oe for the FL and SyAF, respectively) are denoted by $\overline{\Delta H_C^{FL}}$ and $\overline{\Delta H_C^{SyAF}}$. Figure 5.7 shows $\overline{\Delta H_C^{FL}}$ and $\overline{\Delta H_C^{SyAF}}$ as a function of temperature and laser excitation power. Linear fits to the data points yield temperature coefficients of the coercivity of 220 mOe/K and 1480 mOe/K for the FL and the SyAF, respectively. The estimated temperature of MTJ due to pulsed laser heating obtained from the two different methods agree very well with each other. This directly proves that also temperature measurements based on the inter-layer exchange coupling of the SyAF provide accurate results.

Table 5.1: Comparison of the three different methods for temperature measurements using an MTJ with respect to sensitivity, required current through the MTJ, measurement time, possibility to detect temperature dynamics, usability.

Method	Sensitivity	Required current	Measurement time	Temperature dynamics	Usability
$R(T)$	several mK	$\sim\text{mA}$	s	✓	easy
H_C^{FL}	hundreds of mK	$\sim\mu\text{A}$	min	×	difficult
H_C^{SyAF}	hundreds of mK	$\sim\mu\text{A}$	min	×	difficult

5.6 Comparison of the three methods and conclusions

In the preceding sections, we have introduced three methods for using the MTJ as a temperature sensor capable of performing quantitative measurement in buried nanoscale environments. The method based on the tunnel resistance has been compared with the method based on the coercivity of the free layer and, likewise, the method based on the coercivity of the free layer has been compared with the method based the coercivity of the SyAF. We cannot directly compare all three methods with each other, mainly because of two reasons. (i) Samples with an out-of plane magnetization of the FL have a similar temperature dependence in the AP and P state and, consequently, $\Delta R(T)$ will be very small. A thermovoltage due to laser pulse heating will further complicate measurements for small $\Delta R(T)$. (ii) Samples with an in-plane magnetization of the FL may have very large switching fields of the SyAF, making studies on SyAF switching very challenging.

Although all of the three methods can be used for temperature measurements, there are certain differences between them. Table 5.1 compares the methods regarding the sensitivity, required bias current through the MTJ, measurement time, possibility to capture temperature dynamics, and usability. Looking at the table it becomes clear that the $R(T)$ method has many advantages over the other techniques. It provides the best sensitivity and is capable of detecting temperature changes of several mK. Moreover, the measurement time is on the order of seconds or smaller and it allows one to perform time-dependent measurements of temperature dynamics. This is not possible with the other two methods. Also from the usability point of view the $R(T)$ method has advantages since the requirements with respect to experimental equipment (e.g., generation of 2-dimensional magnetic fields) are relaxed as compared to the other two methods. The only drawback of the $R(T)$ method is that it requires larger bias currents than the other two methods. In such a case, attention has to be paid that the

$R(T)$ measurement are not influenced by temperature gradients due to thermoelectric effects and self heating [107].

In conclusion, the development of a temperature sensor with high resolutions and accuracy is critical for the future nanotechnology and the promotion of fundamental research. We have discussed the possibility of using the MTJ as a highly sensitive and accurate temperature sensor, which is capable of performing quantitative temperature measurements in buried nanostructures. Such detection schemes are supposed to enable further studies on temperature-induced magnetization dynamics in MTJs. Additionally, experimental methods for nanoscale temperature measurements are important for the validation of nanoscale thermal transport simulations with high impact on the thermal management of nanoscale devices.

6 Magnetoelastic effects in MTJs induced by femtosecond laser pulse excitation

6.1 Introduction

Manipulating the spin through external stimulus is a key issue in the field of spintronic with the aim to boost logic and memory applications. Such a manipulation can be achieved by different physical effects, employing photons, electrons, heat flux, THz radiation, as well as phonons [6, 69, 77, 117–121]. In particular, the interaction of acoustic pulses with spin structures provides interesting prospects. This is because acoustic pulses can be easily generated on picosecond time scales and the magnetoelastic effect (the change of magnetic properties due to elastic deformation) governing the interaction may lead to significant magnetization changes. Recently, the influence of surface acoustic waves (SAWs) on certain nanoelements and magnetic bubbles was studied [64, 121–125]. Additionally, laser-induced acoustic pulses were used to excite magnetization dynamics in ferromagnetic layers [12, 63]. It has been found that the acoustic-pulse-induced precession can be enhanced when being resonantly driven [61, 65, 66], yet, an identification of the precession modes is difficult, even in cases without acoustic perturbation [48, 126, 127]. Based upon the previous studies on magnetoelastic effects [12, 48, 61, 63–66, 121, 126], the next logical step would be to extend these studies to magnetic devices having important industrial relevance. Magnetic tunnel junctions (MTJs) are certainly among these devices as they are used in data storage, magnetic sensor and other spintronic applications. So far, manipulation of the magnetization in MTJs has been realized by charge currents or heat currents through spin transfer torque (STT) [51, 128]. Moreover, strain has been used to manipulate the MTJ's magnetization [129, 130]. Yet, no experiment on acoustic-pulse-induced magnetization dynamics in MTJs has been reported.

In this chapter, we study the excitation of magnetization dynamics in MTJs by femtosecond-laser-induced acoustic pulses taking advantage of the magnetoelastic coupling. Due to the dependence of the tunnel resistance on the magnetization orientation of the FL in the MTJs, our technique can directly measure small spin precession an-

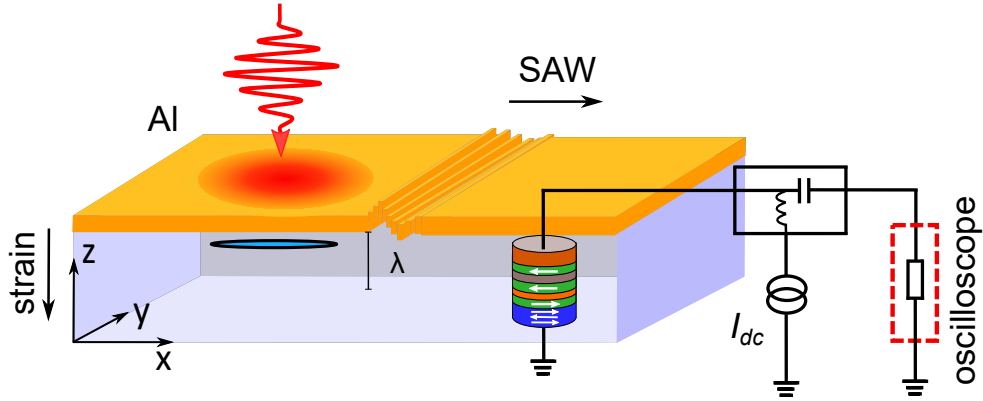


Figure 6.1: Schematic sketch of the experimental setup for SAW driven magnetization dynamics in the MTJ. The setup is also used for study the STT induced magnetization dynamics in the MTJ with voltage pulse instead of laser pulse.

gles. Using a time resolved detection technique we are able to pinpoint SAWs as being responsible for the spin manipulation and exclude other acoustic waves and effects resulting from laser pulse excitation. Moreover, the magnetization mode driven by the SAWs in the free layer of the MTJ can be determined by comparison to magnetization modes triggered by charge current pulses and micromagnetic simulations. So far, the identification of the exact magnetization mode in previous magnetoelastic experiments has not been accomplished. Taking advantage of the coherent nature of SAWs, we also show that our scheme allows coherent control of the magnetization. Using two separate acoustic pulses we can either enhance or switch off the precession in the MTJ.

6.2 Experimental basics

The experiments were carried out on a rectangular MTJ nanopillar of the sample A (dimensions of 100×550 nm), which was described in chapter 3. The tunnel magnetoresistance of the MTJ is approximately 100 % and its magnetic anisotropy field is $H_K(\text{FL}) = 100$ Oe as being determined from a measured Stoner-Wohlfarth astroid, as shown in Fig. 3.6(c). The laser pulses were obtained from a femtosecond laser (500 fs pulse width, 300 kHz repetition rate, 1040 nm center wavelength, 15 nJ pulse energy) and focused to a $1/e^2$ diameter of $8 \mu\text{m}$ on the top Al layer, see Fig. 6.2(b). Samples with different nanopillar dimensions showed similar results.

To obtain information about the acoustic pulses generated in the Al layer by the femtosecond laser pulses, we performed a pump and probe beam distortion detection

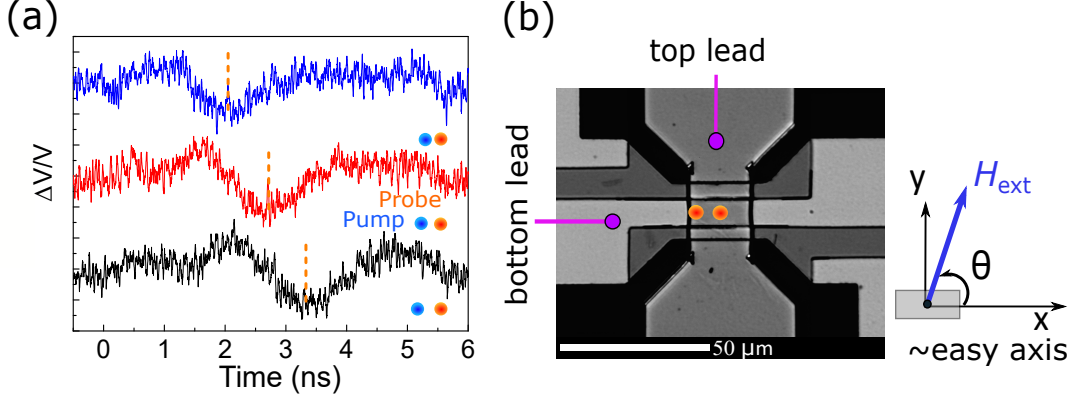


Figure 6.2: (a) Time-domain reflectance measurements of SAWs induced by femtosecond laser pulses for three different distances ($5.3 \mu\text{m}$, $8.9 \mu\text{m}$, and $13.4 \mu\text{m}$) between pump and probe pulse. The dashed vertical lines denote the minimum of the SAWs used to calculate the SAW velocity. (b) Microscope image of the electrical contacts above the MTJ nanopillar with two different laser heating positions (orange dots) and orientation of the MTJ's nominal easy axis as well as the externally applied in-plane magnetic field.

technique (BDD) [76]. Both, picosecond strain pulses (propagating into the sample) and SAWs (propagating along the surface) can be detected. The details of generation and detection of the acoustic pulse have been described in chapter 3. The time traces of SAWs for three different distances ($5.3 \mu\text{m}$, $8.9 \mu\text{m}$, and $13.4 \mu\text{m}$) between pump and probe pulses are shown in Fig. 6.2(a). The measured SAWs have a bipolar shape which is similar to the shape of a typical strain pulse propagating into the sample but with much longer duration of several ns. The duration difference between the strain pulses and SAW is related to the thermal distribution in the Al layer after laser excitation (which extends several μm along the surface but only several 10 nm normal to the surface). From the figure, we estimate the SAW velocity to be $(3.3 \pm 0.5) \mu\text{m}/\text{ns}$. This value compares well with literature data for SAWs in Al of $2.95 \mu\text{m}/\text{ns}$ [131].

The tunnel resistance of the MTJs depends on the angle φ between the magnetization orientation of the FL and the RL [56]:

$$R(\varphi) = R_{\perp} [1 - B \cos \varphi]^{-1}, \quad (6.1)$$

where $B = \frac{R_{\text{AP}} - R_{\text{P}}}{R_{\text{AP}} + R_{\text{P}}}$, $R_{\perp} = \frac{2R_{\text{AP}}R_{\text{P}}}{R_{\text{AP}} + R_{\text{P}}}$ and R_{P} and R_{AP} are the resistance values for $\varphi=0^{\circ}$ (parallel alignment, P) and $\varphi=180^{\circ}$ (antiparallel alignment, AP), respectively. Due to the magnetoelastic effect, a phonon pulse leads to an angular excursion of magnetization of the FL, which in turn causes a change of the tunnel resistance. We neglect the magnetoelastic effect in the fixed layer, since its magnetization is well pinned by the synthetic antiferromagnet. The measurement of SAW-induced magnetization dynamics

in the MTJ is realized by time resolved measurements of tunnel resistance changes.

To study the SAW induced magnetization dynamics in the MTJ, we measured the time resolved voltage change under constant bias current due to tunnel resistance changes by using a sampling oscilloscope with 50Ω input impedance. The trigger signal for the oscilloscope was obtained from the femtosecond laser system such that the oscilloscope time axis is synchronized with the laser pulses. A small current ($I_{dc} = \pm 400 \mu\text{A}$) was applied to the MTJ through a bias tee [48], see Fig. 6.1. To separate signals due to tunnel resistance changes from unwanted background signals, two oscilloscope traces taken for $+I_{dc}$ and $-I_{dc}$ were subtracted from each other after averaging over 2000 individual traces. The time resolution of the experiment is approximately 50 ps as given by the rise-time of the sampling oscilloscope and the transfer function of the other electrical components. Static magnetic fields up to 300 Oe at various in-plane angles θ were applied as indicated in Fig. 6.2(b).

6.3 Surface acoustic wave induced magnetization dynamics in MTJ

For a better understanding, we first give a description of the magnetoelastic effects in the MTJ with different acoustic waves and considering surface acoustic waves (SAWs), strain pulses (SPs), and skimming surface longitudinal waves (SSLWs) generated by the laser pulses [132, 133].

Figure 6.3(a) shows the experimental geometry, where a metal surface is excited with an ultrashort laser pulse, generating acoustic waves propagating into the hemisphere underneath the surface. The acoustic pulses lead to lattice displacements \mathbf{u} which are described by the elastic strain tensor $\varepsilon_{ij} = \partial\mu_i/\partial x_j$. Due to rotational symmetry we only consider x and z components of the strain tensor and neglect y components. The magnetization of the free layer is described in the (1, 2, 3) coordinate system, with the equilibrium magnetization orientation \mathbf{m}_3 lying in the plane of the magnetic layer and φ_0 being the angle between \mathbf{m}_3 and \mathbf{x} , see Fig. 6.3(a). The acoustic waves induce magnetization precession through the occurrence of transverse magnetization components \mathbf{m}_1 and \mathbf{m}_2 ; with \mathbf{m}_2 also lying in the plane of the magnetic layer. Based upon previous magnetoelastic calculations we can express the acoustic wave induced magnetic driving field along the 1 and 2 directions as [61, 62]:

$$\mu_0 \begin{pmatrix} h_1 \\ h_2 \end{pmatrix} = \begin{pmatrix} 2b_2\varepsilon_{xz} \cos \varphi_0 \\ 2b_1\varepsilon_{xx} \sin \varphi_0 \cos \varphi_0 \end{pmatrix}, \quad (6.2)$$

where b_1 and b_2 are magnetoelastic coupling constants.

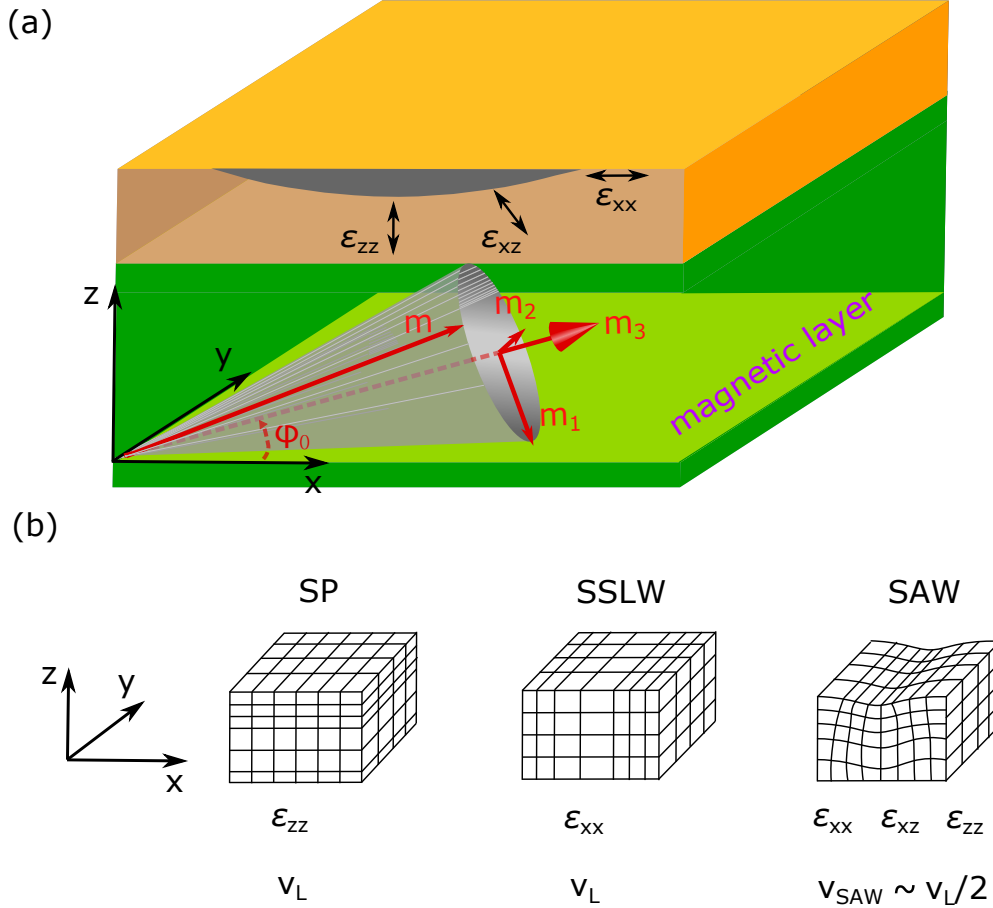


Figure 6.3: (a) Experimental geometry. A metal surface (yellow) is excited with an ultrashort optical pulse, generating different time-dependent strain tensor components ϵ_{ij} . The strain tensor components might interact with the magnetization of the magnetic layer, thereby inducing time-dependent magnetization dynamics. The dynamics can be described in the 1, 2, 3 coordinate system with the 3-direction being equal to the equilibrium magnetization \mathbf{m}_3 and the 2-direction lying in the plane of the magnetic layer. (b) Three most prominent acoustic waves and the corresponding strain tensor components and velocities. SP: strain pulses, SSLW: surface skimming longitudinal waves, SAW: surface acoustic waves.

From this model it is clear that mainly the ε_{xz} and ε_{xx} components of the strain tensor induce magnetization changes. We now have to assign the appropriate strain tensor components to the different acoustic waves [58,134,135], see Fig. 6.3(b). In this figure we also listed the corresponding velocities with $v_L \approx 6.4$ nm/s being the velocity of sound in Aluminum [136]. The properties of the different acoustic waves and Eq. (6.2) lead to three important conclusions:

1. The SPs, which reaches the MTJ after approximately 80 ps, mainly involve the ε_{zz} strain tensor component. However, this component does not couple to the in-plane magnetization (being directed along the x direction) and, thus, cannot excite any magnetization dynamics.
2. The SSLWs involve a strain tensor component (ε_{xx}), which might couple to the in-plane magnetization. However, these waves propagate with approximately twice the velocity ($6.4 \mu\text{m/ns}$) as compared to the SAWs. This larger velocity is not consistent with the measurements of $(3.3 \pm 0.5) \mu\text{m/ns}$, as shown in Fig. 6.2(a).
3. Only the SAWs have the right strain tensor components to interact with the in-plane magnetization (ε_{xx} and ε_{xz}) and a velocity being consistent with the measurements. Consequently, we strongly believe that it is the SAWs which induce the magnetization dynamics in the MTJ's free layer. It is worth to mention that the penetration depth of SAW into the substrate is close to its wavelength $\lambda \approx$ several μm [137]. The MTJ is located just 150 nm below the top Al layer and, thus, well within the penetration depth of the SAWs.

6.3.1 Position dependent measurement

We now comment on the experimental results. Figures 6.4(a) and (b) show the measured oscilloscope traces for two different magnetic field amplitudes and two different laser excitation positions. While the magnetic field was either $H_{\theta=85^\circ} = 120$ Oe (red, lower curves), corresponding to an AP state of the MTJ, or $H_{\theta=85^\circ} = -150$ Oe (black, upper curves), corresponding to a P state of the MTJ, the excitation spots were either right above the MTJ (a) or $10 \mu\text{m}$ away (b). In all cases, an oscillatory behavior due to precession is observed. The measured oscillation is approximately a factor of three larger in the AP state than in the P state and it persists for several nanoseconds, see Fig. 6.4(a). The difference between the AP and P state is linked to the dependence on the applied magnetic field angle, which will be discussed below. Comparing the precession obtained for the different laser excitation spots it is obvious that for excitation $10 \mu\text{m}$ away from the MTJ nanopillar, the precession starts about 3 ns later as compared to an excitation right above the MTJ. This time delay agrees very well

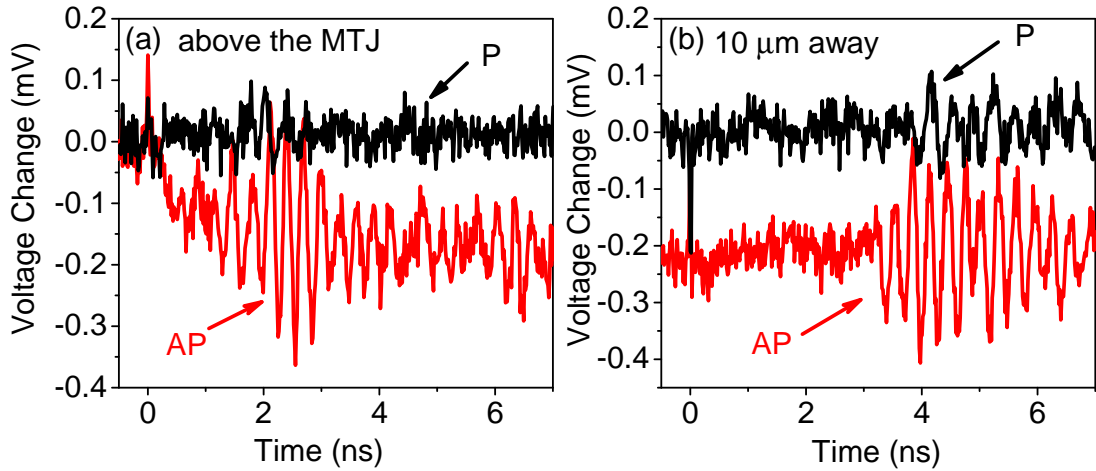


Figure 6.4: Time-resolved voltage change across the MTJ for different excitation conditions and magnetic fields. (a) Optical excitation right above the MTJ nanopillar and (b) $10 \mu\text{m}$ away from the nanopillar. The black and red traces correspond to parallel (P, $H_{\text{ex}} = -150 \text{ Oe}$) and antiparallel (AP, $H_{\text{ex}} = 120 \text{ Oe}$) alignment of the MTJ for $\theta = 85^\circ$. In (b) the red curve is shifted by -0.2 mV for clarity.

with the propagation time of SAWs in Al [131]. As described on the discussion of the interaction magnetoelastic of the MTJ with different acoustic waves, we can exclude other acoustic waves, such as picosecond strain pulses or surface skimming longitudinal waves, as origin of the observed magnetization dynamics. Most likely it is the duration of the SAWs of several ns which leads to the long magnetization precession shown in Fig. 4. We additionally note that the magnetization dynamics in Fig. 4(a) starts at approximately 0.7 ns after the laser excitation. We believe that this delay results from the uncertainty in positioning the center of the pump spot ($8 \mu\text{m}$ $1/e^2$ diameter) right above the MTJ stack ($100 \text{ nm} \times 550 \text{ nm}$) and the spatial shape of the laser excitation spot which is not perfectly symmetric.

For laser excitation right above the MTJ, the AP signal experiences a slow decay within the first ns after the laser pulse hits the Al contact, see Fig. 6.4(a). This is not observed in Fig. 6.4(b) where the red curve is shifted along the y axis for clarity. The slowly decaying signal in Fig. 6.4(a) is due to the heat diffusion from the Al surface to the buried MTJ and results from temperature dependence of spin polarized tunneling. Using the method described in chapter 4 [107], we estimate the time-dependent temperature rise in the MTJ to be approximately 3.2 K . We checked the temperature dependence of the precession frequency obtained from STT experiments with step-like voltage pulses using an electric heating stage below the MTJ sample. A temperature increase up to 30 K has almost no influence on the measured precession. Due to this dependence and because the slowly decaying contribution of Fig. 6.4(a)

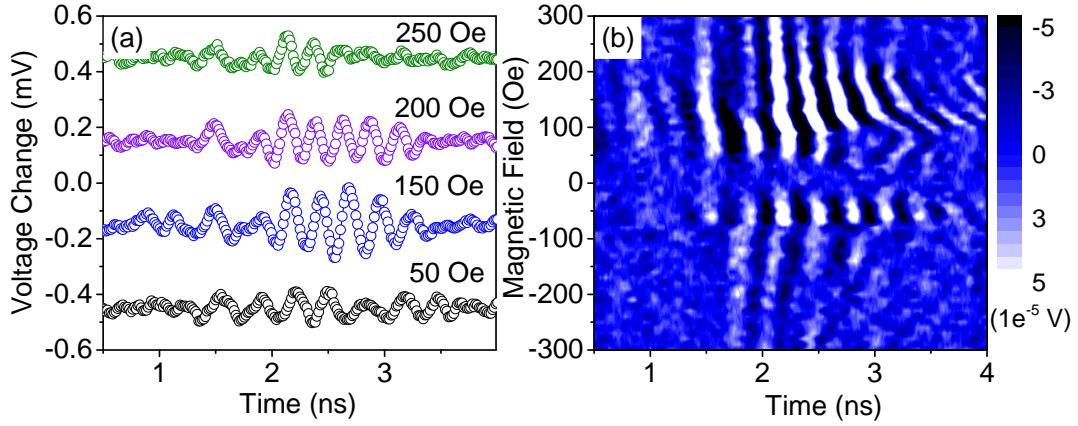


Figure 6.5: (a) Optical excitation right above the MTJ and different magnetic field amplitudes for $\theta = 85^\circ$. All curves are shifted along the y axis for clarity. (b) Contour map of magnetization traces when the magnetic field is swept from the AP to the P state for $\theta = 85^\circ$ and a laser pulse energy of 15 nJ.

vanishes for an excitation position $10 \mu\text{m}$ away from the MTJ, we can safely exclude the laser-induced temperature rise and, thus, a thermal STT as the origin of the observed magnetization dynamics.

6.3.2 Magnetic field dependent measurement

To further study the SAW induced magnetization dynamics, the applied magnetic field amplitude and angle was systematically varied for laser excitation right above the MTJ. We find that the largest signal occurs for a magnetic field of approximately 150 Oe (AP state), see Fig. 6.5(a). A large magnetization precession signal has been found in the magnetic field range of 50 Oe to 200 Oe and -50 to -100 Oe in the AP state, but the precession is very weak when the field is larger than 200 Oe and smaller than -100 Oe, as shown in Fig. 6.5(b). We believe that the magnetic field dependence of the magnetoelastic mode is linked to the magnetic field dependence of the magnetization mode, which occurs in the sample without acoustic perturbation, see discussion further below.

In addition to the dependence on magnetic field amplitude we also find a pronounced dependence on the magnetic field angle, see Fig. 6.6(a). The largest precession occurs for an applied field close to the hard axis of the MTJ ($\theta = 85^\circ$) for the magnetic field amplitude of $H_{\text{ex}} = 120$ Oe. The amplitude of precession gradually decreases when the magnetic field is changed from $\theta = 85^\circ$ to $\theta = 0^\circ$. At $\theta = 45^\circ$, only small magnetization precession can be found in a small magnetic field range which is close to

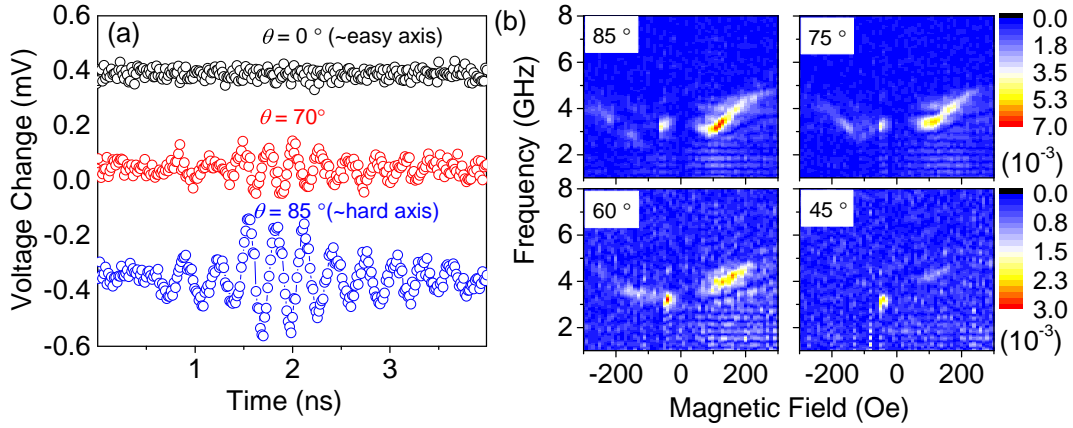


Figure 6.6: (a) Optical excitation right above the MTJ and a magnetic field amplitude of $H_{\text{ex}} = 120$ Oe but for different field angles θ . The black and blue curves are shifted along the y axis for clarity. (b) Spectrum of magnetization dynamics when the magnetic field is applied at different field angles θ with a laser pulse energy of 15 nJ.

the switching field, as shown in Fig. 6.6(b). The amplitude and angle dependencies of the magnetization dynamics show that magnetization precession can hardly be excited by the SAW when the magnetization orientation of the FL is close to the easy axis, but it is easily induced when the magnetization orientation has an angle with the easy axis.

Such magnetic field dependence of the magnetization dynamics is may results from the sensitivity of measurement technique (the sensitivity is proportional to the derivative of the MR loops with respected to the magnetic field). It might also be due to the magnetoelastic coupling which depends on the magnetization orientation of the FL and the strain tensors of the SAW, as described in Eq. 6.2. With the anisotropy field $H_K(\text{FL}) = 100$ Oe of the MTJ as obtained from Fig. 3.6 (c), we find that the largest amplitude of the magnetization precession occurs when φ_0 is in the range $(37^\circ, 59^\circ)$ and $(-29^\circ, -50^\circ)$, which is in agreement with the calculated angle dependence of the magnetization dynamics driven by the strain tensor ε_{xx} , see Eq. 6.2. It seems that the longitudinal motion ε_{xx} of the SAW makes a great contribution to the excited dynamics, while the ε_{xz} makes very little contribution. Yet further studies are needed to specify the contributions to the dynamics from the specific strain tensors. We also believe that the angle dependence of the precession signal mainly indicates the existence of non-uniform modes localized close to the edges of a ferromagnetic stripe. These modes typically occur for external magnetic fields applied perpendicular to an anisotropy field [127, 138]. We will comment on the existence of non-uniform modes in more detail further below.

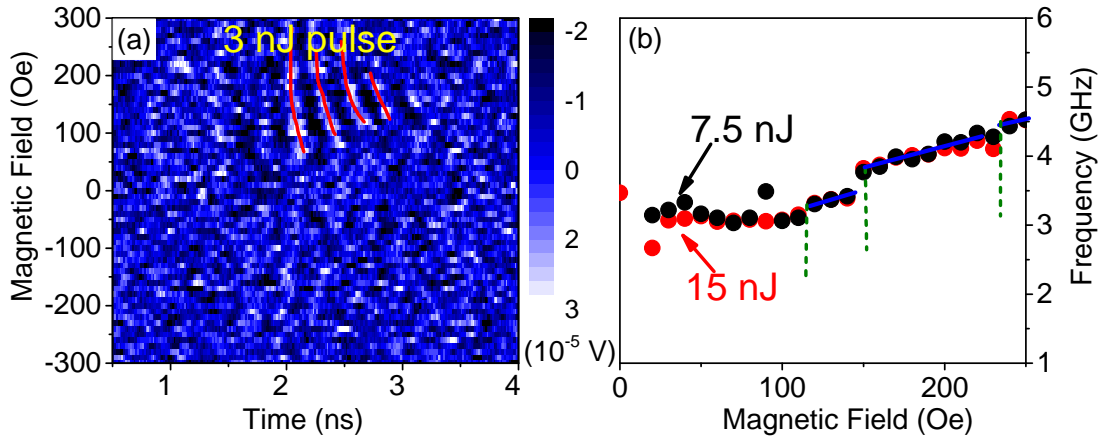


Figure 6.7: (a) Couture map of magnetization traces when the magnetic field sweeps from AP to P state for $\theta = 85^\circ$ with laser pulse energy of 3 nJ. (b) Precession frequency versus applied magnetic field amplitude along the hard axis for two different optical excitation energies (black dots for 7.5 nJ and red dots for 15 nJ).

6.3.3 Laser power dependent measurement

We now analyze the dependence of the precession frequency on the SAW stimulus. This analysis is important to identify the type of magnetization modes being excited by the SAW. The magnetization dynamics can already be excited with a low laser pulse energy of 3 nJ, see Fig. 6.7(a). In Fig. 6.7(b) we have plotted the precession frequency versus applied magnetic field amplitude at $\theta = 85^\circ$ for two optical excitation energies (black dots and red dots for 7.5 nJ and 15 nJ, respectively). In general, the precession frequency increases with applied field amplitude and does not depend on the optical excitation power. The latter dependence further demonstrates that the SAW induced precession is not the result of optical heating of the sample. In such a case we would expect a pronounced dependence on optical excitation power.

Figure 6.7(b) also indicates the onset of a step like dependence of the precession frequency on the applied magnetic field at approximately 150 Oe and to a lesser extent at 120 Oe and 230 Oe. Such a step like behavior has already been observed in ferromagnetic samples and can be explained with an additional magnetic field component resulting from magnetoelastic coupling [61, 139]. In MTJ samples of smaller size we even observed a frequency pinning over the range of several hundred Oe (not shown).

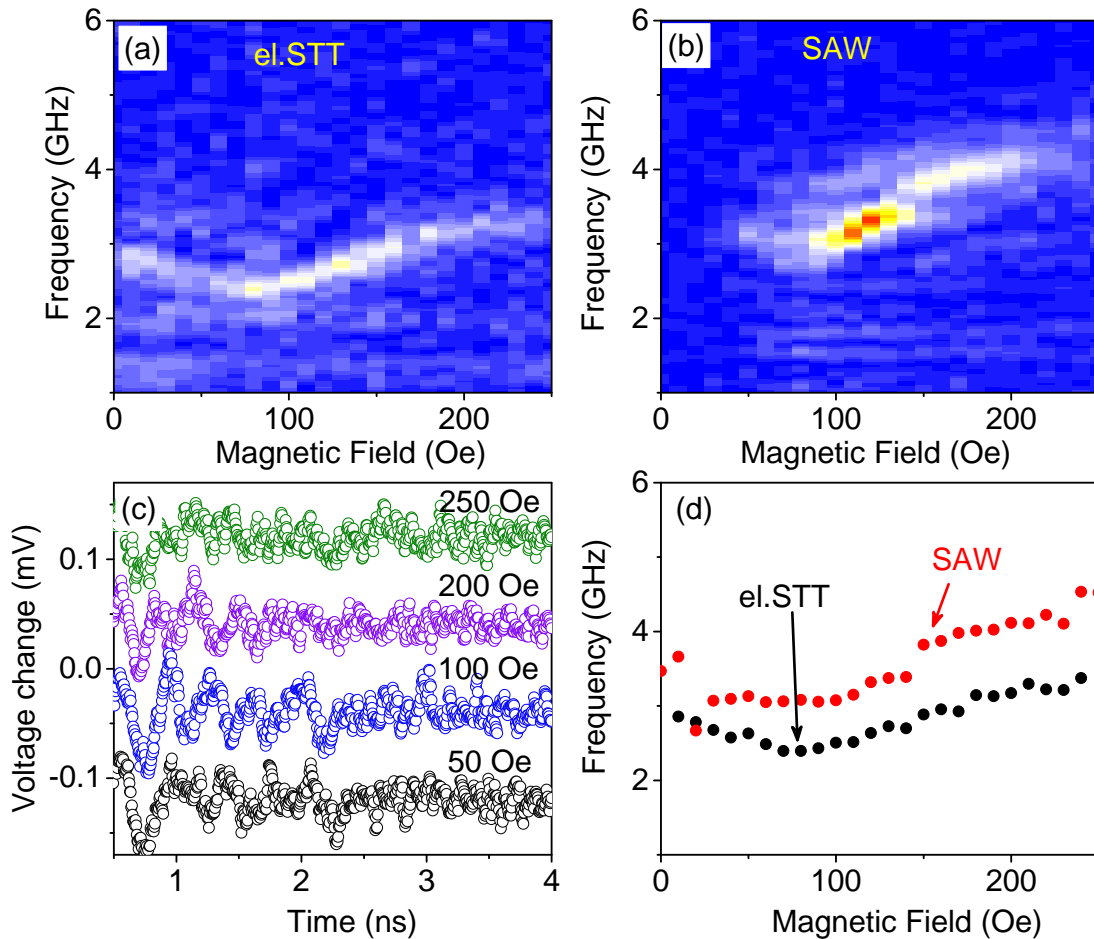


Figure 6.8: (a) and (b) show contour plots of the precession frequency spectra versus magnetic fields along the hard axis driven by 80-ps-long current pulses (electric STT) and SAWs. (c) Magnetization dynamics traces induced by electric STT at different magnetic field amplitudes for $\theta = 85^\circ$. All curves are shifted along the y axis for clarity. (d) Extracted precession frequency versus applied magnetic fields from (a) and (b).

6.4 Magnetization dynamics driven by charge spin transfer torque

In previous studies on magnetoelastic effects in thin magnetic layers, precession signals were read out using optical techniques [12, 66, 121, 140, 141] and it was difficult to determine the spin wave mode of the unperturbed and perturbed system (with respect to elastic perturbations). In our work we measure the precession using fast electrical read out of the MTJ resistance. Since its magnetization dynamics driven by charge current pulses has been well studied [48, 128], our experimental scheme allows for the comparison of the unperturbed magnetization modes with the SAW induced modes. With this comparison we are able to assign the SAW-induced magnetization mode to a spatially non-uniform spin wave mode being mainly localized at the edges of the free layer as explained in the following.

We applied 180-ps-long current pulses with an amplitude of approximately 8 mA and a repetition rate of 100 kHz to the MTJ. The free magnetization precession induced by the current pulse through STT was measured after the pulse decay using a fast sampling oscilloscope [48, 107] with the magnetic field applied along the hard axis. Details of the electric STT induced magnetization precession is described in chapter 3, see Fig. 3.8 (b).

The contour map of Fig. 6.8(a) and (b) shows the precession frequency spectrum versus magnetic field induced by electric STT and SAWs, respectively. Figure 6.8(c) shows the measured magnetization dynamics traces of MTJ induced by electric STT at different magnetic field amplitudes for $\theta = 85^\circ$. The dynamics clearly depends on the magnetic field as shown in Fig. 6.5(a). The precession frequencies obtained from this experiment are visualized in Fig. 6.8(d) as the black dots versus magnetic field amplitude. While the magnetic field dependence of the electric STT induced free precession qualitatively resembles the magnetic field dependence of the SAW induced precession, the SAW frequencies are always larger than the free precession frequencies. Most likely, this frequency difference results from the transition of pure spin waves to magnetoelastic waves. Calculating the dispersion relation of magnetoelastic waves one finds that in the crossover region between pure spin waves and pure elastic waves two magnetoelastic branches exist, having larger and smaller frequencies than the pure spin wave [142]. We believe that the SAW mainly excites the larger frequency branch of the magnetoelastic mode. We can rule out that the magnetization change induced by the magnetoelastic effect causes a significant shift of the precession frequency of a certain magnetization mode. If this were true, we would have observed a dependence of the precession frequency on the optical excitation energy in Fig. 6.7(b).

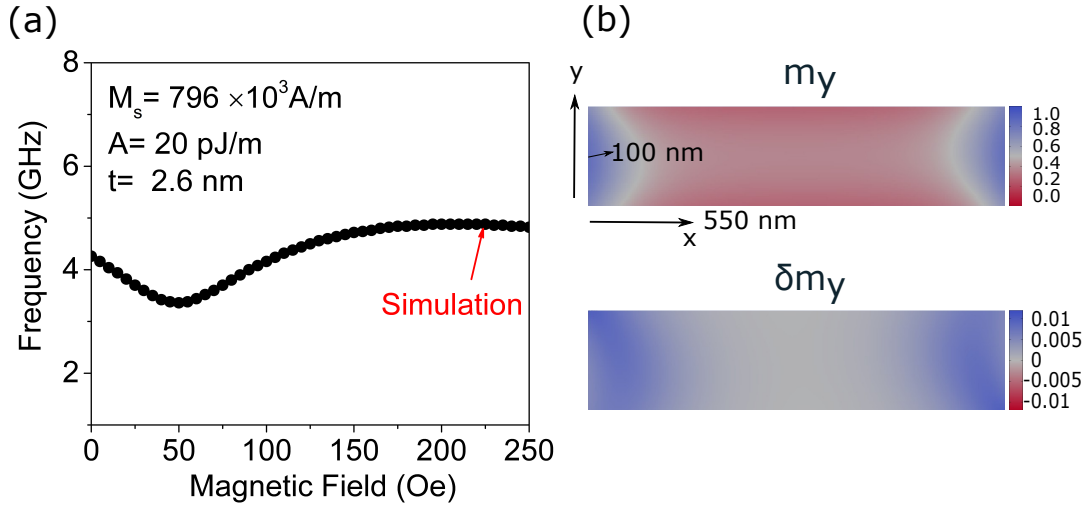


Figure 6.9: (a) Simulated frequency of the free precession in the free layer versus applied magnetic field amplitude. (b) Upper part: Simulated equilibrium configuration of the magnetization component in the y direction in the FL for an applied magnetic field amplitude of 225 Oe. Lower part: Dynamical changes of the magnetization component in the y direction in the FL for an applied magnetic field amplitude of 225 Oe. The oscillations occur near the edges (blue region).

6.5 Simulation of magnetization dynamics driven by surface acoustic waves

Since the magnetic field dependence of the SAW induced precession closely resembles the free precession, it is very likely that the magnetization modes are equal. It is therefore possible to simulate the free precession in the free layer to obtain qualitative information about the magnetization mode being induced by the SAW. For the simulation of free precession we have employed the micromagnetic simulation tool mumax. The following parameters (which have either been taken from literature or from experiments) have been used for the simulation: saturation magnetisation $M_s = 796 \text{ kA/m}$, perpendicular magnetic anisotropy $K_u = 7.96 \text{ kJ/m}^3$, and exchange constant $A_{\text{ex}} = 20 \text{ pJ/m}$. The simulated sample, which has the same nominal dimensions as the FL in the experiment, is discretized in elements of $2 \text{ nm} \times 2 \text{ nm} \times 2.6 \text{ nm}$.

Figure 6.9(a) shows the simulated free precession frequency versus applied magnetic field along the y direction for an excitation of the FL with a sinc function having a cut-off frequency of 15 GHz and a total simulation time of 50 ns. The simulated behavior qualitatively agrees with the measurements. However, the simulated frequencies are higher than experimentally observed. We attribute this difference to certain parameters

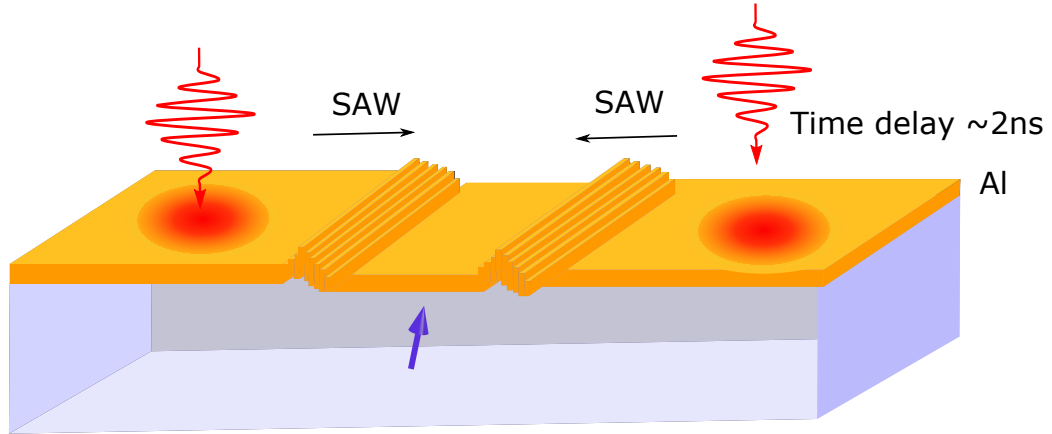


Figure 6.10: Schematic sketch of the experimental setup for coherent control of magnetization dynamics in the MTJ by two femtosecond laser pulse. The second laser beam is time delayed with the first beam, the maximum delay time up to 2 ns. The second laser beam can excite the sample at same positions and different positions with first laser beam.

of the simulation which are not exactly known such as the exact shape of the free layer (e.g., deviation from the nominal shape after lithography).

The upper part of Fig. 6.9(b) shows the y component of the static magnetization vector $\mathbf{m}_{\text{eq}}(x, y)$ of the magnetization mode at an applied magnetic field of 225 Oe. The lower part shows the y component of the dynamical part $\delta\mathbf{m}(x, y)$ of the magnetization mode, which is obtained from the magnetization \mathbf{m} at a certain time instant using $\delta\mathbf{m} = \mathbf{m} - (\mathbf{m} \cdot \mathbf{m}_{\text{eq}})\mathbf{m}_{\text{eq}}$. Both, the static and the dynamical parts clearly show that the free precession mode is confined close to the edges of the FL. This, in turn, strongly suggests that also the SAW induced magnetization dynamics in the FL of the MTJ is linked to a spatially non-uniform mode being localized close to the edges.

6.6 Coherent control of SAW induced magnetization dynamics

Finally, the coherent nature of SAW-induced magnetization dynamics also enables the coherent manipulation of the magnetization by means of two SAW pulses. Figure 6.10 shows a sketch of the measurement. The delay time of the second laser beam with respect to the first beam can be tuned with a delay stage.

Figure 6.11(a) shows time-resolved magnetization traces (again obtained from tunnel

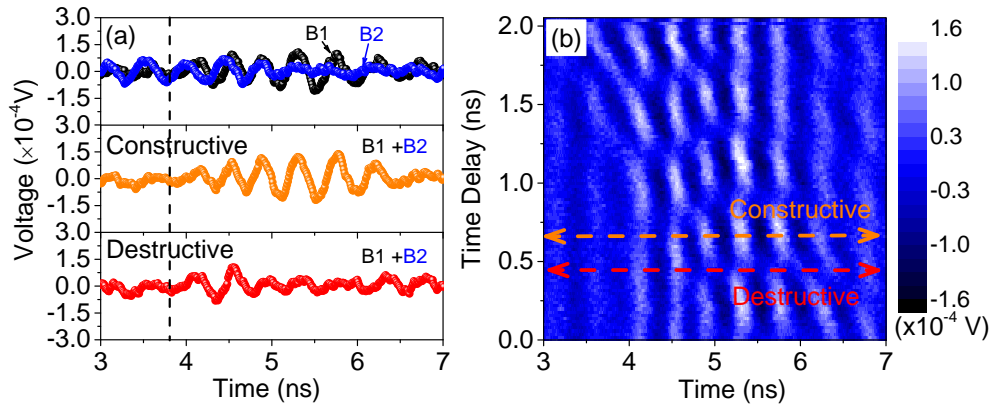


Figure 6.11: Coherent control of magnetization dynamics using two time-delayed laser pulses B1 and B2 being focused onto the same position of the upper contact approximately $10 \mu\text{m}$ away from the MTJ stack. Upper plot: only pulse B1 (black) or B2 (blue), middle plot: constructive interference between B1 and B2, lower plot: destructive interference between B1 and B2. (b) Contour plot of the magnetization dynamics versus time delay between B1 and B2. The horizontal lines correspond to the two lower plots of (a).

resistance measurements using a fast sampling oscilloscope) employing two laser pulses, which were focused onto the same position $10 \mu\text{m}$ away from MTJ and can be time delayed with respect to each other. By varying the time delay between the two pulses the magnetization signal can either be amplified or attenuated by coherent control. A clear periodic dependence of destructive and constructive interferences of magnetic oscillations on the delay between two laser pulses is observed in the contour plot of Fig. 6.11(b). It should be noted that coherent control of the magnetization precession can also be achieved when keeping the time delay between the two laser pulses constant and varying the position of one laser spot with respect to the other. The coherent control study directly extends previous coherent control experiments on magnetization dynamics [117, 119, 143–145] to an industrially relevant device and, thus, might prove useful for future applications.

6.7 Conclusions

In this chapter, we have employed nanopatterned MTJs to study magnetization dynamics driven by femtosecond-laser-pulse-induced SAWs. We could identify a spatially non-uniform magnetization mode as being excited by the SAWs and demonstrated coherent control of magnetization in MTJs using acoustic pulses. Our results open

prospects for future applications, in which magnetization has to be controlled on ultrafast time scales. Additionally, they provide valuable information for spin caloritronic studies in which temperature and temperature gradients are generated by excitation with ultrafast optical pulses. Our time-resolved experiments directly show that the optically generated acoustic pulses must not be neglected and, under certain experimental conditions, even fully determine the optically induced magnetization dynamics.

7 Summary and outlook

In this thesis, the magnetoresistance response, magnetization dynamics, and magnetization reversal in MTJs subjected to femtosecond laser pulses have been investigated. The femtosecond laser pulses were used to generate heat currents and acoustic pulses. The study showed that the heat pulse has a large influence on the magnetization and magnetization reversal while the acoustic pulse can even excite strong magnetization dynamics. The study provides future prospects for the fast magnetization manipulation based on femtosecond laser pulses.

Directly taking advantage of heat to manipulate spin is considered as one of the most energy friendly ways. The major issue in this study was to separate the temperature effect and the temperature gradient effect on the magnetization from each other. To address this issue, we have firstly studied the heat transport through the MTJ with the femtosecond laser pulse heat source by using the tunneling resistance change between the P and AP states of the MTJ with an in-plane magnetization of the FL, which is sensible to the average temperature of the MTJ. Using this simple approach, not only the average temperature increase of the MTJ due to the high repetition rate of the laser pulses, but also a time-dependent temperature increase were characterized. In combination with COMSOL simulations, the time-resolved temperature drop across the MgO barrier ΔT_{MgO} was also evaluated. Our work provides a scheme to quantitatively study the local time resolved temperatures in nanoscale structures and is relevant for fundamental research in the field of spin caloritronics. From this method we have obtained the knowledge about ΔT_{MgO} , which could reach a few K for a certain laser pulse power. Such a huge temperature gradient in the MgO layer has a strong influence on the magnetization reversal of the FL with an out-of-plane magnetization in an MTJ. By studying the temperature dependence of the magnetization switching field of the SyAF, we got rid of the influence of the temperature effect and extracted the pure temperature gradient effect on the magnetization reversal of the FL, which is as large as the electric STT.

Further more, we also gave a proposal for using the MTJ as a temperature sensor, which is based on three intrinsic properties of the MTJ : (i) the temperature dependence of the tunnel resistance, (ii) the temperature dependence of the coercivity of the FL,

and (iii) the coercivity of the SyAF. We have compared the three methods for the case in which a metal layer above the MTJ was heated by femtosecond laser pulses and a good agreement among the different techniques was achieved.

The second research theme in this thesis covered the excitation and coherent control of magnetization dynamics with laser generated acoustic pulses (SAWs). Acoustic pulses were used to induce a magnetization precession in the FL of the MTJ via magnetoelastic coupling. We ruled out the contributions from other optically generated acoustic pulses to the dynamics, confirming that only the SAWs were relevant. The frequency and amplitude of the precession showed a pronounced dependence on the applied magnetic field which was due to the coupling between the magnetization and strain tensors of the SAWs. A spatially non-uniform magnetization mode was identified and coherent control of the magnetization in MTJs using acoustic pulses was demonstrated. Our results open prospects for future applications, in which magnetization has to be controlled on ultrafast time scales. Our time-resolved experiments directly show that the optically generated acoustic pulses could not be neglected and, even fully determine the optically induced magnetization dynamics under certain experimental conditions.

Before discussing further research, there are a couple of questions left in the proceeding studies which remain unclear. For example, is the T-STT large enough for applications? In T-STT measurements, the influence on the magnetization is dominated by the temperature effect and the parasitic effect (such as strain) in the temperature gradient. A better design of the sample and understanding of T-STT mechanisms in different spintronics devices might be possible to enhance the T-STT effect. The other question is about how to realize magnetization reversal with acoustic pulses. Here, the mechanical displacement and the duration of acoustic waves need to be controlled in order to have an appropriate and efficient interaction between strain tensors and the magnetization to induce magnetization reversal.

Future research could also address the following aspects. A time resolved measurement of thermoelectric voltage in the MTJ with high temporal resolution might be possible for samples with high tunnel magnetothermopower. In such a case, the time resolved temperature drop across the barrier might be extracted, which might allow quantitatively studying the heat transport in MTJ nanopillars. Furthermore, it might allow evaluating the magnitude of T-STT effect in more detail. Moreover, measurements of time resolved local temperatures under laser pulse heating at different repetition rates are important for studying nanoscale heat transport. The study of the contribution of specific strain tensors to the magnetization dynamics might in the future allow to manipulate and switch magnetization by acoustic waves. Additionally, it is worth to investigate the interaction of acoustic waves with other magnetic struc-

tures e.g. domain walls, magnetic nanodots and magnetic skyrmions. In the field of spin caloritronics, the giant magneto heatresistance GMHR in the GMR samples has already been studied experimentally. The value of the GMHR was found to be approximately the same as the giant magnetoresistance (GMR). However, the observation of the tunnel magnetoheatresistance (TMHR) in the MTJ still remains unreported. Partly because it is difficult to measure and characterize the thermal conductivity of magnetic thin layers inside the sample. Our approach for measuring time resolved local temperatures may be a useful tool to extract the spin dependent thermal conductivity in an appropriate MTJ sample.

Bibliography

- [1] G. Binasch, P. Grünberg, F. Saurenbach, and W. Zinn, “Enhanced magnetoresistance in layered magnetic structures with antiferromagnetic interlayer exchange,” *Physical Review B*, vol. 39, no. 7, pp. 4828–4830, 1989.
- [2] M. N. Baibich, J. M. Broto, A. Fert, F. N. Van Dau, F. Petroff, P. Eitenne, G. Creuzet, A. Friederich, and J. Chazelas, “Giant magnetoresistance of (001)Fe/(001)Cr magnetic superlattices,” *Physical Review Letters*, vol. 61, no. 21, pp. 2472–2475, 1988.
- [3] J. S. Moodera, L. R. Kinder, T. M. Wong, and R. Meservey, “Large magnetoresistance at room temperature in ferromagnetic thin film tunnel junctions,” *Physical Review Letters*, vol. 74, no. 16, pp. 3273–3276, 1995.
- [4] J. Slonczewski, “Current-driven excitation of magnetic multilayers,” *Journal of Magnetism and Magnetic Materials*, vol. 159, no. 1-2, pp. L1–L7, 1996.
- [5] L. Berger, “Emission of spin waves by a magnetic multilayer traversed by a current,” *Physical Review B*, vol. 54, no. 13, pp. 9353–9358, 1996.
- [6] Y. Otani, M. Shiraishi, A. Oiwa, E. Saitoh, and S. Murakami, “Spin conversion on the nanoscale,” *Nature Physics*, vol. 13, no. July, pp. 829–832, 2017.
- [7] K. Uchida, S. Takahashi, K. Harii, J. Ieda, W. Koshibae, K. Ando, S. Maekawa, and E. Saitoh, “Observation of the spin Seebeck effect,” *Nature*, vol. 455, no. 7214, pp. 778–81, 2008.
- [8] M. Hatami, G. E. W. Bauer, Q. Zhang, and P. J. Kelly, “Thermal spin-transfer torque in magnetoelectronic devices,” *Physical Review Letters*, vol. 99, no. 6, p. 066603, 2007.
- [9] J. C. Le Breton, S. Sharma, H. Saito, S. Yuasa, and R. Jansen, “Thermal spin current from a ferromagnet to silicon by Seebeck spin tunnelling,” *Nature*, vol. 475, no. 7354, pp. 82–85, 2011.
- [10] X. Jia, K. Xia, and G. E. W. Bauer, “Thermal spin transfer in Fe-MgO-Fe tunnel

- junctions,” *Physical Review Letters*, vol. 107, no. 17, p. 176603, 2011.
- [11] M. Löhndorf, T. Duenas, M. Tewes, E. Quandt, M. Rührig, and J. Wecker, “Highly sensitive strain sensors based on magnetic tunneling junctions,” *Applied Physics Letters*, vol. 81, no. 2, pp. 313–315, 2002.
- [12] D. R. Yakovlev, A. V. Scherbakov, A. S. Salasyuk, A. V. Akimov, X. Liu, M. Bombeck, C. Bru, V. F. Sapega, J. K. Furdyna, and M. Bayer, “Coherent Magnetization Precession in Ferromagnetic (Ga,Mn)As Induced by Picosecond Acoustic Pulses,” *Physical Review Letters*, vol. 105, no. 11, p. 117204, 2010.
- [13] S. Ikeda, J. Hayakawa, Y. Ashizawa, Y. M. Lee, K. Miura, H. Hasegawa, M. Tsunoda, F. Matsukura, and H. Ohno, “Tunnel magnetoresistance of 604% at 300 K by suppression of Ta diffusion in CoFeB/MgO/CoFeB pseudo-spin-valves annealed at high temperature,” *Applied Physics Letters*, vol. 93, no. 8, p. 082508, 2008.
- [14] S. Bhatti, R. Sbiaa, A. Hirohata, H. Ohno, S. Fukami, and S. N. Piramanayagam, “Spintronics based random access memory: a review,” *Materials Today*, vol. 20, no. 9, pp. 530–548, 2017.
- [15] A. Fert, “Nobel Lecture: Origin, development, and future of spintronics,” *Reviews of Modern Physics*, vol. 80, no. 4, pp. 1517–1530, 2008.
- [16] M. Julliere, “Tunneling between ferromagnetic films,” *Physics Letters A*, vol. 54, no. 3, pp. 225–226, 1975.
- [17] J. C. Slonczewski, “Conductance and exchange coupling of two ferromagnets separated by a tunneling barrier,” *Physical Review B*, vol. 39, no. 10, pp. 6995–7002, 1989.
- [18] H. Jaffrès, D. Lacour, F. Nguyen Van Dau, J. Briatico, F. Petroff, and A. Vaurès, “Angular dependence of the tunnel magnetoresistance in transition-metal-based junctions,” *Physical Review B*, vol. 64, no. 6, p. 064427, 2001.
- [19] W. Butler, X.-G. Zhang, T. Schulthess, and J. MacLaren, “Spin-dependent tunneling conductance of Fe|MgO|Fe sandwiches,” *Physical Review B*, vol. 63, no. 5, p. 054416, 2001.
- [20] S. S. P. Parkin, C. Kaiser, A. Panchula, P. M. Rice, B. Hughes, M. Samant, and S.-H. Yang, “Giant tunnelling magnetoresistance at room temperature with MgO (100) tunnel barriers,” *Nature materials*, vol. 3, no. 12, pp. 862–867, 2004.
- [21] S. Yuasa, T. Nagahama, A. Fukushima, Y. Suzuki, and K. Ando, “Giant room-temperature magnetoresistance in single-crystal Fe/MgO/Fe magnetic tunnel

- junctions,” *Nature Materials*, vol. 3, no. 12, pp. 868–871, 2004.
- [22] W. F. Brinkman, R. C. Dynes, and J. M. Rowell, “Tunneling conductance of asymmetrical barriers,” *Journal of Applied Physics*, vol. 41, no. 5, pp. 1915–1921, 1970.
- [23] J. S. Moodera, J. Nowak, and R. J. Van De Veerdonk, “Interface magnetism and spin wave scattering in ferromagnet-insulator-ferromagnet tunnel junctions,” *Physical Review Letters*, vol. 80, no. 13, pp. 2941–2944, 1998.
- [24] S. Zhang, P. Levy, a. Marley, and S. Parkin, “Quenching of Magnetoresistance by Hot Electrons in Magnetic Tunnel Junctions,” *Physical Review Letters*, vol. 79, no. 19, pp. 3744–3747, 1997.
- [25] V. Drewello, J. Schmalhorst, A. Thomas, and G. Reiss, “Evidence for strong magnon contribution to the TMR temperature dependence in MgO based tunnel junctions,” *Physical Review B*, vol. 77, no. 1, p. 014440, 2008.
- [26] X. F. Han, A. C. Yu, M. Oogane, J. Murai, T. Daibou, and T. Miyazaki, “Analyses of intrinsic magnetoelectric properties in spin-valve-type tunnel junctions with high magnetoresistance and low resistance,” *Physical Review B*, vol. 63, no. 22, p. 224404, 2001.
- [27] C. Shang, J. Nowak, R. Jansen, and J. Moodera, “Temperature dependence of magnetoresistance and surface magnetization in ferromagnetic tunnel junctions,” *Physical Review B*, vol. 58, no. 6, pp. R2917–R2920, 1998.
- [28] J. M. Teixeira, J. Ventura, J. P. Araujo, J. B. Sousa, P. Wisniowski, and P. P. Freitas, “Tunneling processes in thin MgO magnetic junctions,” *Applied Physics Letters*, vol. 96, no. 26, pp. 137–140, 2010.
- [29] Q. L. Ma, S. G. Wang, J. Zhang, Y. Wang, R. C. C. Ward, C. Wang, A. Kohn, X. G. Zhang, and X. F. Han, “Temperature dependence of resistance in epitaxial Fe/MgO/Fe magnetic tunnel junctions,” *Applied Physics Letters*, vol. 95, no. 5, p. 052506, 2009.
- [30] A. M. Bratkovsky, “Assisted tunneling in ferromagnetic junctions and half-metallic oxides,” *Applied Physics Letters*, vol. 72, no. 18, pp. 2334–2336, 1998.
- [31] T. Dimopoulos, Y. Henry, V. Da Costa, C. Tiusan, and K. Ounadjela, “Influence of barrier overoxidation and annealing on the inelastic spin-dependent tunneling in AlO_x-based junctions,” *Journal of Applied Physics*, vol. 95, no. 11, pp. 6936–6938, 2004.

- [32] B. Hu, K. Moges, Y. Honda, H.-x. Liu, T. Uemura, and M. Yamamoto, “Temperature dependence of spin-dependent tunneling conductance of magnetic tunnel junctions with half-metallic Co₂MnSi electrodes,” *Physical Review B*, vol. 94, no. 9, p. 094428, 2016.
- [33] P. Bruno, “Theory of interlayer magnetic coupling,” *Physical Review B*, vol. 52, no. 1, pp. 411–439, 1995.
- [34] M. Labrune, J. Kools, and a. Thiaville, “Magnetization rotation in spin-valve multilayers,” *Journal of Magnetism and Magnetic Materials*, vol. 171, no. 1-2, pp. 1–15, 1997.
- [35] E. Stoner and E. Wohlfarth, “A mechanism of magnetic hysteresis in heterogeneous alloys,” *Philosophical transactions of the Royal Society of London. Ser. A*, vol. 240, no. 826, p. 599, 1948.
- [36] A. Thiaville, “Extensions of the geometric solution of the two dimensional coherent magnetization rotation model,” *Journal of Magnetism and Magnetic Materials*, vol. 182, no. 1-2, pp. 5–18, 1998.
- [37] S. Kaka and S. E. Russek, “Precessional switching of submicrometer spin valves,” *Applied Physics Letters*, vol. 80, no. 16, pp. 2958–2960, 2002.
- [38] Y. Henry, S. Mangin, J. Cuchiaro, J. A. Katine, and E. E. Fullerton, “Distortion of the Stoner-Wohlfarth astroid by a spin-polarized current,” *Physical Review B*, vol. 79, no. 21, p. 214422, 2009.
- [39] E. Beaurepaire, J. C. Merle, A. Daunois, and J. Y. Bigot, “Ultrafast spin dynamics in ferromagnetic nickel,” *Physical Review Letters*, vol. 76, no. 22, pp. 4250–4253, 1996.
- [40] L. Landau and E. Lifshits, “on the Theory of the Dispersion of Magnetic Permeability in Ferromagnetic Bodies,” *Physikalische Zeitschrift der Sowjetunion*, vol. 169, no. 14, pp. 14–22, 1935.
- [41] S. Ikeda, K. Miura, H. Yamamoto, K. Mizunuma, H. D. Gan, M. Endo, S. Kanai, J. Hayakawa, F. Matsukura, and H. Ohno, “A perpendicular-anisotropy CoFeB-MgO magnetic tunnel junction,” *Nature Materials*, vol. 9, no. 9, pp. 721–724, 2010.
- [42] A. Brataas, A. D. Kent, and H. Ohno, “Current-induced torques in magnetic materials,” *Nature materials*, vol. 11, no. 5, pp. 372–381, 2012.
- [43] J. Katine, F. Albert, R. Buhrman, E. Myers, and D. Ralph, “Current-Driven

- Magnetization Reversal and Spin-Wave Excitations in Co/Cu/Co Pillars,” *Physical Review Letters*, vol. 84, no. 14, pp. 3149–3152, 2000.
- [44] S. Petit, C. Baraduc, C. Thirion, U. Ebels, Y. Liu, M. Li, P. Wang, and B. Dieny, “Spin-torque influence on the high-frequency magnetization fluctuations in magnetic tunnel junctions,” *Physical Review Letters*, vol. 98, no. 7, p. 077203, 2007.
- [45] J. C. Sankey, Y.-T. Cui, J. Z. Sun, J. C. Slonczewski, R. A. Buhrman, and D. C. Ralph, “Measurement of the spin-transfer-torque vector in magnetic tunnel junctions,” *Nature Physics*, vol. 4, no. 1, pp. 67–71, 2008.
- [46] A. M. Deac, A. Fukushima, H. Kubota, H. Maehara, Y. Suzuki, S. Yuasa, Y. Nagamine, K. Tsunekawa, D. D. Djayaprawira, and N. Watanabe, “Bias-driven large power microwave emission from MgO-based tunnel magnetoresistance devices,” *Nature Physics*, vol. 4, no. 10, pp. 803–809, 2008.
- [47] H. Kubota, A. Fukushima, K. Yakushiji, T. Nagahama, S. Yuasa, K. Ando, H. Maehara, Y. Nagamine, K. Tsunekawa, D. D. Djayaprawira, N. Watanabe, and Y. Suzuki, “Quantitative measurement of voltage dependence of spin-transfer torque in MgO-based magnetic tunnel junctions,” *Nature Physics*, vol. 4, no. 1, pp. 37–41, 2008.
- [48] S. Serrano-Guisan, K. Rott, G. Reiss, J. Langer, B. Ocker, and H. W. Schumacher, “Biased Quasiballistic Spin Torque Magnetization Reversal,” *Physical Review Letters*, vol. 101, no. 8, p. 087201, 2008.
- [49] C. Wang, Y.-T. Cui, J. A. Katine, R. A. Buhrman, and D. C. Ralph, “Time-resolved measurement of spin-transfer-driven ferromagnetic resonance and spin torque in magnetic tunnel junctions,” *Nature Physics*, vol. 7, no. 6, pp. 496–501, 2011.
- [50] M. Hatami, G. E. W. Bauer, Q. Zhang, and P. J. Kelly, “Thermal spin-transfer torque in magnetoelectronic devices,” *Physical Review Letters*, vol. 99, no. 6, p. 066603, 2007.
- [51] A. Pushp, T. Phung, C. Rettner, B. P. Hughes, S.-H. Yang, and S. S. P. Parkin, “Giant thermal spin-torque-assisted magnetic tunnel junction switching,” *Proceedings of the National Academy of Sciences*, vol. 112, no. 21, pp. 6585–6590, 2015.
- [52] A. Bose, A. K. Shukla, K. Konishi, S. Jain, N. Asam, S. Bhuktare, H. Singh, D. D. Lam, Y. Fujii, S. Miwa, Y. Suzuki, and A. A. Tulapurkar, “Observation

- of thermally driven field-like spin torque in magnetic tunnel junctions,” *Applied Physics Letters*, vol. 109, no. 3, p. 032406, 2016.
- [53] Z. Zhang, L. Bai, X. Chen, H. Guo, X. L. Fan, D. S. Xue, D. Houssameddine, and C. Hu, “Observation of thermal spin-transfer torque via ferromagnetic resonance in magnetic tunnel junctions,” *Physical Review B*, vol. 94, no. 6, p. 064414, 2016.
- [54] A. K. Michel, A. C. Niemann, T. Boehnert, S. Martens, J. M. Montero Moreno, D. Goerlitz, R. Zierold, H. Reith, V. Vega, V. M. Prida, A. Thomas, J. Gooth, and K. Nielsch, “Temperature gradient-induced magnetization reversal of single ferromagnetic nanowires,” *Journal of Physics D: Applied Physics*, vol. 50, no. 49, p. 494007, 2017.
- [55] D. Wang, C. Nordman, Z. Qian, J. M. Daughton, and J. Myers, “Magnetostriction effect of amorphous CoFeB thin films and application in spin-dependent tunnel junctions,” *Journal of Applied Physics*, vol. 97, no. 10, p. 10C906, 2005.
- [56] A. Tavassolizadeh, K. Rott, T. Meier, E. Quandt, H. Hölscher, G. Reiss, and D. Meyners, “Tunnel magnetoresistance sensors with magnetostrictive electrodes: Strain sensors,” *Sensors*, vol. 16, no. 11, p. 1902, 2016.
- [57] J. C. Cheng, L. Wu, and S. Y. Zhang, “Thermoelastic response of pulsed photothermal deformation of thin plates,” *Journal of Applied Physics*, vol. 76, no. 2, pp. 716–722, 1994.
- [58] C. Thomsen, H. T. Grahn, H. J. Maris, and J. Tauc, “Surface generation and detection of phonons by picosecond light pulses,” *Physical Review B*, vol. 34, no. 6, pp. 4129–4138, 1986.
- [59] C. Thomsen, J. Strait, Z. Vardeny, H. J. Maris, J. Tauc, and J. J. Hauser, “Coherent phonon generation and detection by picosecond light pulses,” *Physical Review Letters*, vol. 53, no. 10, pp. 989–992, 1984.
- [60] T. Saito, O. Matsuda, and O. B. Wright, “Picosecond acoustic phonon pulse generation in nickel and chromium,” *Physical Review B*, vol. 67, no. 20, p. 205421, 2003.
- [61] Y. Yahagi, B. Harteneck, S. Cabrini, and H. Schmidt, “Controlling nanomagnet magnetization dynamics via magnetoelastic coupling,” *Physical Review B*, vol. 90, no. 14, p. 140405, 2014.
- [62] L. Dreher, M. Weiler, M. Pernpeintner, H. Huebl, R. Gross, M. S. Brandt, and S. T. B. Goennenwein, “Surface Acoustic Wave-Driven Ferromagnetic Resonance

- in Nickel Thin Films: Theory and Experiment,” *Physical Review B*, vol. 86, no. 13, p. 134415, 2012.
- [63] J. W. Kim, M. Vomir, and J. Y. Bigot, “Ultrafast magnetoacoustics in nickel,” *Physical Review Letters*, vol. 109, no. 5, p. 166601, 2012.
- [64] N. Ogawa, W. Koshibae, A. J. Beekman, N. Nagaosa, M. Kubota, M. Kawasaki, and Y. Tokura, “Photodrive of magnetic bubbles via magnetoelastic waves,” *Proceedings of the National Academy of Sciences*, vol. 112, no. 29, pp. 8977–8981, 2015.
- [65] J. V. Jäger, A. V. Scherbakov, B. A. Glavin, A. S. Salasyuk, R. P. Champion, A. W. Rushforth, D. R. Yakovlev, A. V. Akimov, and M. Bayer, “Resonant driving of magnetization precession in a ferromagnetic layer by coherent monochromatic phonons,” *Physical Review B*, vol. 92, no. 2, p. 020404, 2015.
- [66] J. Janušonis, T. Jansma, C. L. Chang, Q. Liu, A. Gatilova, A. M. Lomonosov, V. Shalagatskyi, T. Pezeril, V. V. Temnov, and R. I. Tobey, “Transient Grating Spectroscopy in Magnetic Thin Films: Simultaneous Detection of Elastic and Magnetic Dynamics,” *Scientific Reports*, vol. 6, no. 7, p. 29143, 2016.
- [67] L. Thevenard, J.-Y. Duquesne, E. Peronne, H. J. von Bardeleben, H. Jaffres, S. Ruttala, J.-M. George, a. Lemaître, and C. Gourdon, “Irreversible magnetization switching using surface acoustic waves,” *Physical Review B*, vol. 87, no. 14, p. 144402, 2013.
- [68] D. A. Garanin, “Generalized equation of motion for a ferromagnet,” *Physica A: Statistical Mechanics and its Applications*, vol. 172, no. 3, pp. 470–491, 1991.
- [69] G.-M. Choi, C.-H. Moon, B.-C. Min, K.-J. Lee, and D. G. Cahill, “Thermal spin-transfer torque driven by the spin-dependent Seebeck effect in metallic spin-valves,” *Nature Physics*, vol. 11, no. 7, pp. 576–581, 2015.
- [70] COMSOL Multiphysics®, “No Title.”
- [71] W. Arnold, B. Betz, and B. Hoffmann, “Efficient generation of surface acoustic waves by thermoelasticity,” *Applied Physics Letters*, vol. 47, no. 7, pp. 672–674, 1985.
- [72] A. Harata, H. Nishimura, and T. Sawada, “Laser-induced surface acoustic waves and photothermal surface gratings generated by crossing two pulsed laser beams,” *Applied Physics Letters*, vol. 57, no. 2, pp. 132–134, 1990.
- [73] B. Bonello, A. Ajinou, V. Richard, P. Djemia, and S. M. Chérif, “Surface acous-

- tic waves in the GHz range generated by periodically patterned metallic stripes illuminated by an ultrashort laser pulse,” *The Journal of the Acoustical Society of America*, vol. 110, no. 4, pp. 1943–1949, 2001.
- [74] J. D. Achenbach, “Laser excitation of surface wave motion,” *Journal of the Mechanics and Physics of Solids*, vol. 51, no. 11-12, pp. 1885–1902, 2003.
- [75] B. Audoin, H. Meri, and C. Rossignol, “Two-dimensional diffraction of plasma, thermal, and elastic waves generated by an infrared laser pulse in semiconductors,” *Physical Review B*, vol. 74, no. 21, p. 214304, 2006.
- [76] J. Higuete, T. Valier-Brasier, T. Dehoux, and B. Audoin, “Beam distortion detection and deflectometry measurements of gigahertz surface acoustic waves,” *Review of Scientific Instruments*, vol. 82, no. 11, p. 114905, 2011.
- [77] J. D. Costa, S. Serrano-Guisan, B. Lacoste, A. S. Jenkins, T. Böhnert, M. Tarequzzaman, J. Borme, F. L. Deepak, E. Paz, J. Ventura, R. Ferreira, and P. P. Freitas, “High power and low critical current density spin transfer torque nanoo oscillators using MgO barriers with intermediate thickness,” *Scientific Reports*, vol. 7, no. 1, p. 7237, 2017.
- [78] W. S. Capinski and H. J. Maris, “Improved apparatus for picosecond pump-and-probe optical measurements,” *Review of Scientific Instruments*, vol. 67, no. 8, pp. 2720–2726, 1996.
- [79] D. G. Cahill, “Analysis of heat flow in layered structures for time-domain thermoreflectance,” *Review of Scientific Instruments*, vol. 75, no. 12, pp. 5119–5122, 2004.
- [80] A. J. Schmidt, X. Chen, and G. Chen, “Pulse accumulation, radial heat conduction, and anisotropic thermal conductivity in pump-probe transient thermoreflectance,” *Review of Scientific Instruments*, vol. 79, no. 11, p. 114902, 2008.
- [81] P. E. Hopkins, J. R. Serrano, L. M. Phinney, S. P. Kearney, T. W. Grasser, and C. T. Harris, “Criteria for Cross-Plane Dominated Thermal Transport in Multilayer Thin Film Systems During Modulated Laser Heating,” *Journal of Heat Transfer*, vol. 132, no. 8, p. 081302, 2010.
- [82] Y. Wang, J. Y. Park, Y. K. Koh, and D. G. Cahill, “Thermoreflectance of metal transducers for time-domain thermoreflectance,” *Journal of Applied Physics*, vol. 108, no. 4, p. 043507, 2010.
- [83] N. Chigarev, C. Rossignol, and B. Audoin, “Surface displacement measured by

- beam distortion detection technique: Application to picosecond ultrasonics,” *Review of Scientific Instruments*, vol. 77, no. 11, p. 114901, 2006.
- [84] G. E. W. Bauer, A. H. MacDonald, and S. Maekawa, “Spin Caloritronics,” *Solid State Communications*, vol. 150, no. 11-12, pp. 459–460, 2010.
- [85] G. E. W. Bauer, E. Saitoh, and B. J. van Wees, “Spin caloritronics,” *Nature materials*, vol. 11, no. 3, pp. 391–399, 2012.
- [86] H. Yu, S. Granville, D. P. Yu, and J. P. Ansermet, “Evidence for thermal spin-transfer torque,” *Physical Review Letters*, vol. 104, no. 14, p. 146601, 2010.
- [87] A. Slachter, F. L. Bakker, J.-P. Adam, and B. J. van Wees, “Thermally driven spin injection from a ferromagnet into a non-magnetic metal,” *Nature Physics*, vol. 6, no. 11, pp. 879–882, 2010.
- [88] E. Padrón-Hernández, A. Azevedo, and S. M. Rezende, “Amplification of spin waves by thermal spin-transfer torque,” *Physical Review Letters*, vol. 107, no. 19, p. 197203, 2011.
- [89] Y. Yue and X. Wang, “Nanoscale thermal probing,” *Nano reviews*, vol. 3, p. 11586, 2012.
- [90] D. G. Cahill, W. K. Ford, K. E. Goodson, G. D. Mahan, A. Majumdar, H. J. Maris, R. Merlin, and S. R. Phillpot, “Nanoscale thermal transport,” *Journal of Applied Physics*, vol. 93, no. 2, pp. 793–818, 2002.
- [91] X. Kou, J. Schmalhorst, A. Thomas, and G. Reiss, “Temperature dependence of the resistance of magnetic tunnel junctions with MgO barrier,” *Applied Physics Letters*, vol. 88, no. 21, p. 212115, 2006.
- [92] N. Liebing, S. Serrano-Guisan, K. Rott, G. Reiss, J. Langer, B. Ocker, and H. W. Schumacher, “Tunneling magnetothermopower in magnetic tunnel junction nanopillars,” *Physical Review Letters*, vol. 107, no. 17, p. 177201, 2011.
- [93] M. Walter, J. Walowski, V. Zbarsky, M. Münzenberg, M. Schäfers, D. Ebke, G. Reiss, A. Thomas, P. Peretzki, M. Seibt, J. S. Moodera, M. Czerner, M. Bachmann, and C. Heiliger, “Seebeck effect in magnetic tunnel junctions,” *Nature Materials*, vol. 10, no. 10, pp. 742–746, 2011.
- [94] N. Liebing, S. Serrano-Guisan, P. Krzysteczko, K. Rott, G. Reiss, J. Langer, B. Ocker, and H. W. Schumacher, “Tunneling magneto thermocurrent in CoFeB/MgO/CoFeB based magnetic tunnel junctions,” *Applied Physics Letters*, vol. 102, no. 24, p. 242413, 2013.

- [95] S. D. Brorson, J. G. Fujimoto, and E. P. Ippen, “Femtosecond electronic heat-transport dynamics in thin gold films,” *Physical Review Letters*, vol. 59, no. 17, pp. 1962–1965, 1987.
- [96] S. M. Lee, D. G. Cahill, and T. H. Allen, “Thermal conductivity of sputtered oxide films,” *Physical Review B*, vol. 52, no. 1, pp. 253–257, 1995.
- [97] M. Walter, J. Walowski, V. Zbarsky, M. Münzenberg, M. Schäfers, D. Ebke, G. Reiss, A. Thomas, P. Peretzki, M. Seibt, J. S. Moodera, M. Czerner, M. Bachmann, and C. Heiliger, “Seebeck effect in magnetic tunnel junctions.,” *Nature materials*, vol. 10, no. 10, pp. 742–746, 2011.
- [98] J. Zhang, M. Bachman, M. Czerner, and C. Heiliger, “Thermal Transport and Nonequilibrium Temperature Drop Across a Magnetic Tunnel Junction,” *Physical Review Letters*, vol. 115, no. 3, p. 037203, 2015.
- [99] C. Papusoi, R. Sousa, J. Herault, I. L. Prejbeanu, and B. Dieny, “Probing fast heating in magnetic tunnel junction structures with exchange bias,” *New Journal of Physics*, vol. 10, p. 103006, 2008.
- [100] B. C. Gundrum, D. G. Cahill, and R. S. Averback, “Thermal conductance of metal-metal interfaces,” *Physical Review B*, vol. 72, no. 24, p. 245426, 2005.
- [101] T. Böhnert, R. Dutra, R. L. Sommer, E. Paz, S. Serrano-Guisan, R. Ferreira, and P. P. Freitas, “Influence of the thermal interface resistance on the thermovoltage of a magnetic tunnel junction,” *Physical Review B*, vol. 95, no. 10, p. 104441, 2017.
- [102] M. Czerner, M. Bachmann, and C. Heiliger, “Spin caloritronics in magnetic tunnel junctions: Ab initio studies,” *Physical Review B*, vol. 83, no. 13, p. 132405, 2011.
- [103] W. Lin, M. Hehn, L. Chaput, B. Negulescu, S. Andrieu, F. Montaigne, and S. Mangin, “Giant thermoelectric effect in Al₂O₃ magnetic tunnel junctions,” *Nature communications*, vol. 3, p. 744, 2012.
- [104] S. Z. Wang, K. Xia, and G. E. W. Bauer, “Thermoelectricity and disorder of FeCo/MgO/FeCo magnetic tunnel junctions,” *Physical Review B*, vol. 90, no. 22, p. 224406, 2014.
- [105] J. Z. Sun, S. L. Brown, W. Chen, E. A. Delenia, M. C. Gaidis, J. Harms, G. Hu, X. Jiang, R. Kilaru, W. Kula, G. Lauer, L. Q. Liu, S. Murthy, J. Nowak, E. J. O’Sullivan, S. S. Parkin, R. P. Robertazzi, P. M. Rice, G. Sandhu, T. Topuria, and D. C. Worledge, “Spin-torque switching efficiency in CoFeB-MgO based tunnel

- junctions,” *Physical Review B*, vol. 88, no. 10, p. 104426, 2013.
- [106] A. Sengupta, C. M. Liyanagedera, B. Jung, and K. Roy, “Magnetic Tunnel Junction as an On-Chip Temperature Sensor,” *Scientific Reports*, vol. 7, no. 1, p. 11764, 2017.
- [107] H. F. Yang, X. K. Hu, N. Liebing, T. Böhnert, J. D. Costa, M. Tarequzzaman, R. Ferreira, S. Sievers, M. Bieler, and H. W. Schumacher, “Electrical measurement of absolute temperature and temperature transients in a buried nanostructure under ultrafast optical heating,” *Applied Physics Letters*, vol. 110, no. 23, p. 232403, 2017.
- [108] A. Chavent, C. Ducruet, C. Portemont, L. Vila, R. Sousa, I. L. Prejbeanu, and B. Dieny, “Steady State and Dynamics of Joule Heating in Magnetic Tunnel Junctions Observed via the Temperature Dependence of RKKY Coupling,” *Physical Review Applied*, vol. 6, p. 034003, 2016.
- [109] J. M. Teixeira, J. Ventura, J. P. Araujo, J. B. Sousa, P. Wisniowski, and P. P. Freitas, “Tunneling processes in thin MgO magnetic junctions,” *Applied Physics Letters*, vol. 96, no. 26, pp. 2008–2011, 2010.
- [110] Q. L. Ma, S. G. Wang, J. Zhang, Y. Wang, R. C. C. Ward, C. Wang, A. Kohn, X. G. Zhang, and X. F. Han, “Temperature dependence of resistance in epitaxial Fe/MgO/Fe magnetic tunnel junctions,” *Applied Physics Letters*, vol. 95, no. 5, p. 052506, 2009.
- [111] Y. Takeuchi, H. Sato, S. Fukami, F. Matsukura, and H. Ohno, “Temperature dependence of energy barrier in CoFeB-MgO magnetic tunnel junctions with perpendicular easy axis Temperature dependence of energy barrier in CoFeB-MgO magnetic tunnel junctions with perpendicular easy axis,” *Applied Physics Letters*, vol. 107, no. 2015, p. 152405, 2015.
- [112] H. Liu, R. Wang, P. Guo, Z. Wen, J. Feng, H. Wei, X. Han, Y. Ji, and S. Zhang, “Manipulation of magnetization switching and tunnel magnetoresistance via temperature and voltage control,” *Scientific Reports*, vol. 5, p. 18269, 2015.
- [113] J. T. McKinney, “Kinetic effects in coercivity measurements,” *IEEE Transactions on Magnetics*, vol. 17, no. 6, pp. 3020–3022, 1981.
- [114] J. Igarashi, J. Llandro, H. Sato, F. Matsukura, and H. Ohno, “junctions with perpendicular easy axis Magnetic-field-angle dependence of coercivity in CoFeB / MgO magnetic tunnel junctions with perpendicular easy axis,” *Applied Physics Letters*, vol. 111, no. 13, p. 132407, 2017.

- [115] A. Gayen, K. Umadevi, A. C. J, and P. Alagarsamy, “Tuning Magnetic Properties of Thick CoFeB Film by Interlayer Coupling in Trilayer Structured Thin Films,” *Journal of Material Sciences and Engineering*, vol. 7, no. 2, p. 1000437, 2018.
- [116] N. Wiese, T. Dimopoulos, M. Rühlig, J. Wecker, G. Reiss, J. Sort, and J. Nogués, “Strong temperature dependence of antiferromagnetic coupling in CoFeB/Ru/CoFeB,” *Europhysics Letters*, vol. 78, no. 6, p. 67002, 2007.
- [117] A. V. Kimel, A. Kirilyuk, P. A. Usachev, R. V. Pisarev, A. M. Balbashov, and T. Rasing, “Ultrafast non-thermal control of magnetization by instantaneous photomagnetic pulses,” *Nature*, vol. 435, no. 7042, pp. 655–657, 2005.
- [118] N. Berggaard, M. Hehn, S. Mangin, G. Lengaigne, F. Montaigne, M. L. Lalieu, B. Koopmans, and G. Malinowski, “Hot-Electron-Induced Ultrafast Demagnetization in Co/Pt Multilayers,” *Physical Review Letters*, vol. 117, no. 14, p. 147203, 2016.
- [119] K. Yamaguchi, M. Nakajima, and T. Suemoto, “Coherent control of spin precession motion with impulsive magnetic fields of half-cycle terahertz radiation,” *Physical Review Letters*, vol. 105, no. 23, p. 237201, 2010.
- [120] K. Shen and G. E. W. Bauer, “Laser-Induced Spatiotemporal Dynamics of Magnetic Films,” *Physical Review Letters*, vol. 115, no. 19, p. 197201, 2015.
- [121] M. Foerster, F. Macià, N. Statuto, S. Finizio, A. Hernández-Mínguez, S. Lendínez, P. V. Santos, J. Fontcuberta, J. M. Hernández, M. Kläui, and L. Aballe, “Direct imaging of delayed magneto-dynamic modes induced by surface acoustic waves,” *Nature Communications*, vol. 8, no. 1, p. 407, 2017.
- [122] Y. Au, M. Dvornik, T. Davison, E. Ahmad, P. S. Keatley, A. Vansteenkiste, B. Van Waeyenberge, and V. V. Kruglyak, “Direct excitation of propagating spin waves by focused ultrashort optical pulses,” *Physical Review Letters*, vol. 110, no. 9, p. 097201, 2013.
- [123] S. Davis, A. Baruth, and S. Adenwalla, “Magnetization dynamics triggered by surface acoustic waves,” *Applied Physics Letters*, vol. 97, no. 23, p. 232507, 2010.
- [124] V. Sampath, N. D’Souza, D. Bhattacharya, G. M. Atkinson, S. Bandyopadhyay, and J. Atulasimha, “Acoustic-Wave-Induced Magnetization Switching of Magnetostrictive Nanomagnets from Single-Domain to Nonvolatile Vortex States,” *Nano Letters*, vol. 16, no. 9, pp. 5681–5687, 2016.
- [125] O. Kovalenko, T. Pezeril, and V. V. Temnov, “New concept for magnetization

- switching by ultrafast acoustic pulses,” *Physical Review Letters*, vol. 110, no. 26, p. 266602, 2013.
- [126] Z. Zeng, K. H. Cheung, H. W. Jiang, I. N. Krivorotov, J. A. Katine, V. Tiberkevich, and A. Slavin, “Evolution of spin-wave modes in magnetic tunnel junction nanopillars,” *Physical Review B*, vol. 82, no. 10, p. 100410, 2010.
- [127] C. Bayer, J. P. Park, H. Wang, M. Yan, C. E. Campbell, and P. A. Crowell, “Spin waves in an inhomogeneously magnetized stripe,” *Physical Review B*, vol. 69, no. 13, p. 134401, 2004.
- [128] C. Wang, Y.-T. Cui, J. A. Katine, R. A. Buhrman, and D. C. Ralph, “Time-resolved measurement of spin-transfer-driven ferromagnetic resonance and spin torque in magnetic tunnel junctions,” *Nature Physics*, vol. 7, no. 6, pp. 496–501, 2011.
- [129] P. Li, A. Chen, D. Li, Y. Zhao, S. Zhang, L. Yang, Y. Liu, M. Zhu, H. Zhang, and X. Han, “Electric field manipulation of magnetization rotation and tunneling magnetoresistance of magnetic tunnel junctions at room temperature,” *Advanced Materials*, vol. 26, no. 25, pp. 4320–4325, 2014.
- [130] Z. Zhao, M. Jamali, N. D’Souza, D. Zhang, S. Bandyopadhyay, J. Atulasimha, and J. P. Wang, “Giant voltage manipulation of MgO-based magnetic tunnel junctions via localized anisotropic strain: A potential pathway to ultra-energy-efficient memory technology,” *Applied Physics Letters*, vol. 109, no. 9, p. 092403, 2016.
- [131] H.-C. Wang, S. Fleming, and Y.-C. Lee, “Simple, all-optical, noncontact, depth-selective, narrowband surface acoustic wave measurement system for evaluating the Rayleigh velocity of small samples or areas,” *Appl Opt*, vol. 48, no. 8, pp. 1444–1451, 2009.
- [132] A. Neubrand and P. Hess, “Laser generation and detection of surface acoustic waves: Elastic properties of surface layers,” *Journal of Applied Physics*, vol. 71, no. 1, pp. 227–238, 1992.
- [133] D. Schneider and T. Schwarz, “A photoacoustic method for characterising thin films,” *Surface and Coatings Technology*, vol. 91, no. 1-2, pp. 136–146, 1997.
- [134] D. Veysset, A. A. Maznev, I. A. Veres, T. Pezeril, S. E. Kooi, A. M. Lomonosov, and K. A. Nelson, “Acoustical breakdown of materials by focusing of laser-generated Rayleigh surface waves,” *Applied Physics Letters*, vol. 111, no. 3, p. 031901, 2017.

- [135] C. L. Chang, A. M. Lomonosov, J. Janusonis, V. S. Vlasov, V. V. Temnov, and R. I. Tobey, “Parametric frequency mixing in a magnetoelastically driven linear ferromagnetic-resonance oscillator,” *Physical Review B*, vol. 95, no. 6, p. 060409, 2017.
- [136] D. G. Cahill and F. Watanabe, “Thermal conductivity of isotopically pure and Ge-doped Si epitaxial layers from 300 to 550 K,” *Physical Review B*, vol. 70, no. 23, p. 235322, 2004.
- [137] G. W. Farnell and E. L. Adler, *Elastic Wave Propagation in Thin Layers*, vol. 9. ACADEMIC PRESS, INC., 1972.
- [138] R. D. McMichael and B. B. Maranville, “Edge saturation fields and dynamic edge modes in ideal and non-ideal magnetic film edges,” *Physical Review B*, vol. 74, no. 2, p. 024424, 2006.
- [139] J. Janušonis, C. L. Chang, P. H. Van Loosdrecht, and R. I. Tobey, “Frequency tunable surface magneto elastic waves,” *Applied Physics Letters*, vol. 106, no. 18, p. 181601, 2015.
- [140] M. Bombeck, A. S. Salasyuk, B. A. Glavin, A. V. Scherbakov, C. Brüggemann, D. R. Yakovlev, V. F. Sapega, X. Liu, J. K. Furdyna, A. V. Akimov, and M. Bayer, “Excitation of spin waves in ferromagnetic (Ga,Mn)As layers by picosecond strain pulses,” *Physical Review B*, vol. 85, no. 19, p. 195324, 2012.
- [141] J. V. Jäger, A. V. Scherbakov, T. L. Linnik, D. R. Yakovlev, M. Wang, P. Wadley, V. Holy, S. A. Cavill, A. V. Akimov, A. W. Rushforth, and M. Bayer, “Picosecond inverse magnetostriction in gallenol thin films,” *Applied Physics Letters*, vol. 103, no. 3, p. 032409, 2013.
- [142] E. Schlömann, “Generation of phonons in high-power ferromagnetic resonance experiments,” *Journal of Applied Physics*, vol. 31, no. 9, pp. 1647–1656, 1960.
- [143] S. Garzon, L. Ye, R. A. Webb, T. M. Crawford, M. Covington, and S. Kaka, “Coherent control of nanomagnet dynamics via ultrafast spin torque pulses,” *Physical Review B*, vol. 78, no. 18, p. 180401, 2008.
- [144] D. Bossini, S. Dal Conte, Y. Hashimoto, A. Secchi, R. V. Pisarev, T. Rasing, G. Cerullo, and A. V. Kimel, “Macrospin dynamics in antiferromagnets triggered by sub-20 femtosecond injection of nanomagnons,” *Nature Communications*, vol. 7, p. 10645, 2016.
- [145] J. W. Kim, M. Vomir, and J. Y. Bigot, “Controlling the spins angular momentum

in ferromagnets with sequences of picosecond acoustic pulses,” *Scientific Reports*, vol. 5, p. 8511, 2014.

List of Figures

1.1	Main results. (a) A schematic viewgraph of the interaction of the MTJ with the laser pulses. The study contains two relevant excitation source: heat pulses and acoustic pulses. (b) The measured time resolved resistance traces of MTJs for the case in which heat transport from the surface to the MTJ takes place after the laser pulses. A large difference has been found when the MTJ is the AP and P states, which is due to the temperature dependence of resistance of the MTJ in the two states. (c) The time resolved temperature of the MTJ for different laser heating powers converted from (b). (d) Magnetization dynamics traces at various external magnetic fields excited by the SAWs. (e) Coherent control of magnetization dynamics with two laser pulses.	3
2.1	A schematic of the two current model for spin dependent transport in MTJs for (a) the P state and (b) the AP state. Electrons can only tunnel to the sub-band of the same spin direction. With the same bias voltage, more electrons can tunnel through the barrier in the P state than in the AP state (left side of the figure). The conductance of the MTJ is proportional to the product of the electron density of states (DOS) of the FM1 and FM2 layers, see right side of the figure.	6
2.2	Tunneling density of state (DOS) for the majority spin when the Fe(001)/MgO(001)/Fe(001) junction is in the P state. Δ represents different symmetries of Bloch states. The Bloch state with Δ_1 symmetry shows a very slow decay in the MgO barrier. The figure is from reference [19]. ©American Physical Society	8
2.3	(a) Conductance versus bias voltage measured at room temperature and low temperature for a Co/Al ₂ O ₃ /Ni ₈₀ Fe ₂₀ junction. The figure is from reference [23]. ©American Physical Society (b) Temperature dependence of R_{AP} and R_P for Co ₇₀ Fe ₃₀ /MgO/Co ₈₄ Fe ₁₆ . The figure is taken from reference [20]. ©2004, Springer Nature	9

2.4	(a) Typical MTJ stack. (b) Easy axis magnetoresistance (MR) loop due to magnetization reversal of the FL and the RL layer with uniaxial anisotropy. The minor MR loop results from the FL and the major loop refers to the RL.	11
2.5	The Stoner-Wohlfarth astroid. When the applied magnetic field H_{ex} sweeps from the right to the left (blue arrow), the magnetization orientation (red arrows) of the particle for each magnetic field value (A and B are representative values of H_{ex} being applied outside and inside of the astroid) can be extracted from the astroid.	12
2.6	Magnetization dynamics described by the Landau-Lifshitz-Gilbert-Slonczewski equation.	14
2.7	A schematic of femtosecond laser pulse generated heat current and SAW.	19
3.1	(a) A schematic of cross section for the layer structure of the MTJ nanopillars fabricated at INL. (b) Microscope image of one MTJ sample. The yellow dot marks the position of the MTJ nanopillar.	24
3.2	(a) Optical pump and probe technique. The Al layer on the surface serves as a transducer. (b) A schematic of pump and probe setup for TDTR and BDD. PBS : polarized beam splitter, BBO: Beta-Barium borate, AOM: acoustic optic modulator	26
3.3	(a) Illustration of the fitting algorithm using measurement data obtained from the multilayer (100 nm Al/ 600 nm SiO ₂ / Si substrate) at a modulation frequency of 1 MHz. The fit starts 0.1 ns after the pump pulse hit the surface. At this time, electrons and phonons have the same temperature. The obtained interface thermal conductances and thermal conductivity are shown in the figure, values in the brackets are taken from literature [81]. (b) Surface temperature changes after femtosecond laser excitation extracted from the TDTR method. Inset: The peaks occurring after the maximum are reflections of the strain pulse.	27
3.4	(a) Mechanism of beam distortion detection technique (BDD). (b) The left side of the figure shows the measured SAWs as a function of distance between pump and probe beam (0, 5.3, 8.9, 13.4 and 14.7 μm). The right side of the figure shows the image of the pump and probe spots from the CCD camera.	28
3.5	Setup used for electrical resistance measurement. It mainly consists of three parts. From left to the right, they are the optical part, the heating part and the detection part.	29

3.6	(a) Setup used for magnetoresistance (MR) measurement. (b) Typical MR loop measured when the magnetic field sweeps along the nominal easy axis ($\theta = 0^\circ$) of the MTJ without bias magnetic field. H_C^+ and H_C^- are the coercivity field of the FL when its magnetization switches from the high resistance state (AP state) to the low resistance state (P state) and vice versa, respectively. (c) Extracted astroid (hollow green circles) extracted from MR loops, which are measured at bias magnetic fields along the nominal hard axis. The filled green circles represent the switching points extracted from the figure (b).	31
3.7	Schematic of the setup used for time resolved resistance measurement. Two excitation sources: laser pulse or voltage pulse. For laser pulse excitation, the pulse generator is not connected. With voltage pulse excitation, a power splitter (PS) is inserted between the bias tee and the oscilloscope so that half of the generated voltage goes into MTJ and the other half to oscilloscope. A voltage inverter (IVT) is used to change the polarity of the voltage pulse.	32
3.8	(a) Voltage traces $V_{\text{scope}}(t)$ measured by a sampling oscilloscope when $\pm I_{\text{dc}}$ are applied through the MTJ with a 5 ns voltage pulse excitation. (b) The obtained voltage trace $V_{\text{MTJ}}(t)$ of the MTJ after subtraction of the two voltage traces $V_{\text{scope}}(t)$ shown in figure (a).	33
3.9	Setup used for time resolved resistance measurement results from temperature effects in the MTJ.	34
4.1	Schematic sketch of the experimental setup and MTJ sample. FL: free layer, SyAF: synthetic antiferromagnet, AF: antiferromagnet.	36
4.2	(a) MR loops measured at different currents at $T_0 = 32.7^\circ\text{C}$. (b) Conductance in the AP state as a function of the bias voltage. The red curve is a quadratic fit.	38
4.3	(a) MR loops for different temperatures obtained from electric heating at $I_{\text{dc}} = 0.2\text{ mA}$. (b) Resistance difference between AP and P state versus temperature change obtained from electric heating at $I_{\text{dc}} = 0.2\text{ mA}$ and 2 mA	39
4.4	(a) MR loops for different laser powers at $I_{\text{dc}} = 0.2\text{ mA}$. The insets show the resistance change in the P state for $+0.2\text{ mA}$ and -0.2 mA , respectively. (b) Resistance difference between AP and P state versus laser power at $I_{\text{dc}} = 0.2\text{ mA}$ and 2 mA . The scales on the right-hand side show the corresponding temperature increase in the MTJ deduced from the ΔR versus ΔT curves in Fig. 4.3(b) at $I_{\text{dc}} = 0.2\text{ mA}$ (black scale) and 2 mA (red scale).	40

4.5	Time-resolved resistance change of the MTJ after laser pulse excitation for $I_{\text{dc}} = 2$ mA in the (a) AP and (b) P states.	41
4.6	Time-resolved temperature changes for different laser powers and for (a) $I_{\text{dc}} = 0.4$ mA and (b) 2 mA, respectively. To obtain the absolute temperature the value $T_0 = 32.7$ °C has to be added to the ΔT values.	42
4.7	Simulation of the time-resolved temperature change of the MTJ for an optical power of 100 mW. The maximum temperature occurs 3.5 ns after laser pulse heating (dashed line). The inset of figure shows the temperature change of the Al layer measured by TDTR method used for the simulations.	43
4.8	(a) Simulated temperature distribution of every layer in the two dimensional cross-section of the sample at 2.5 ns after laser pulse heating. A large temperature difference can be found between the upper and the lower interface of MgO barrier when $\kappa_{\text{MgO}} = 0.2$ W m ⁻¹ K ⁻¹ is used in the simulation. (b) Extracted temperatures for each layer of the MTJ samples from the red dashed line shown in the cross-section of the sample. (c) and (d) Simulated time resolved temperature drop $\Delta' T_{\text{MgO}}(t)$ across the MgO barrier after laser pulse excitation assuming a thermal conductivity of MgO of 4 W m ⁻¹ K ⁻¹ and of 0.2 W m ⁻¹ K ⁻¹ , respectively.	45
4.9	(a) Easy axis themovoltage loops under different laser heating powers. The themovoltage is measured by a high impedance nanovoltmeter. (b) The thermovoltage V_{TP} as a function of the laser power. The scale on the right-hand side shows the corresponding temperature $T = \Delta T + 29.1$ (°C) of the MTJ calculated from the temperature coefficient of the resistance.	47
4.10	(a) MR loops for different laser powers at $I_{\text{dc}} = 0.05$ mA. (b) MR loops for different electric heating temperature at $I_{\text{dc}} = 0.05$ mA. The loop on the left side of dashed line shows the magnetization switching of the FL and the loop on the right side shows switching of the SyAF layer.	48
4.11	Swiching field changes of SyAF ($-\Delta H_{\text{C}}^{\text{SyAF}+}$) versus laser power and electric heating temperature at $I_{\text{dc}} = 0.05$ mA when the magnetization switches from the AP to the P state. The scale on the top shows the corresponding temperature increase in the MTJ for different laser heating powers deduced from the electric heating result.	49

- 4.12 The two figures on the left side show MR loops of the FL measured at different (a) temperatures and (b) laser heating powers at $I_{dc} = 0.05$ mA. While in (a) only a temperature effect occurs, in (b) a temperature and a temperature gradient effect might be present. The right two figures show MR loops of the FL measured at different bias currents (c) positive bias current (+ electrons flow from the RL to the FL) and (d) negative bias current (-). The arrows represent the shift of the switching field due to effects of the temperature T , temperature gradient ΔT_{MgO} and charge induced spin transfer torque STT. 50
- 4.13 The measured astroids of the (a) the FL and (b) SyAF as a function of the laser heating power and the electric heating temperature, respectively. 51
- 5.1 (a) Schematic sketch of the MTJ as a buried nanoscale temperature sensor. (b) Typical MR loop with a magnetic field applied along the easy axis of the MTJ. The minor loop corresponds to the magnetization reversal of the free layer (red arrow), whereas the major loop corresponds to the magnetization reversal of the reference layer in the SyAF (upper blue arrow). The green arrows mark the three most important properties of the MR loop: tunnel resistance change ΔR , coercivity of the FL H_C^{FL} , and coercivity of the reference layer of the SyAF H_C^{SyAF} 54
- 5.2 Resistance change ΔR of the MTJ as a function of laser power (bottom scale) and as a function of temperature change due to electric heating (top scale). Due to the overlap of the curves, the upper axis directly shows the temperature rise of the MTJ for different laser excitation powers. 56
- 5.3 (a) MR loops with the magnetic field applied along the easy axis for different temperatures obtained from electric heating at $I_{dc} = 0.01$ mA. (b) MR loops for different laser powers at $I_{dc} = 0.01$ mA. Note that the resistance change due to a thermovoltage has been eliminated in (b). . . 57
- 5.4 Coercivity change ΔH_C^{FL+} (red) and resistance change ΔR (black) of the MTJ's free layer as a function of laser excitation power (bottom scale) and temperature change due to electric heating (top scale). For clarity, the zero values of the right and left axis are vertically shifted. Otherwise most of the data points would perfectly overlap diminishing the readability. Due to the identical slope of all curves, the upper axis directly shows the temperature rise of the MTJ for different laser excitation powers. . . 58

5.5	(a) MR loops and (b) Stoner-Wohlfarth astroids measured for electric and laser heating both of which are supposed to lead to the same temperature. For a certain magnetic field angle $\Delta H_C^{\text{FL}+}$ obtained from both heating conditions might be different (a), yet, averaging over the magnetic field angle nearly identical average values $\overline{\Delta H_C^{\text{FL}}}$ are obtained (b). The terms Magnetic Field and Bias Field denote magnetic fields applied along the easy and hard axis of the MTJ, respectively.	59
5.6	(a) Measured MR loops for the magnetic field applied along the easy axis of the MTJ at $I_{\text{dc}} = 0.05$ mA. (b) Switching points for the FL and the SyAF extracted from MR loop measurements at various magnetic fields applied along the hard axis, referred to as Bias Field in the figure. . . .	60
5.7	Averaged coercivity changes $\overline{\Delta H_C^{\text{FL}}}(T)$ (black) and $\overline{\Delta H_C^{\text{SyAF}}}(T)$ (red) as a function of laser power (bottom scale) and temperature change due to electric heating (top scale). For clarity, the zero values of the right and left axis are vertically shifted. Due to the identical slope of the measurements the upper axis directly shows the temperature rise of the MTJ for different laser excitation powers.	61
6.1	Schematic sketch of the experimental setup for SAW driven magnetization dynamics in the MTJ. The setup is also used for study the STT induced magnetization dynamics in the MTJ with voltage pulse instead of laser pulse.	66
6.2	(a) Time-domain reflectance measurements of SAWs induced by femtosecond laser pulses for three different distances ($5.3 \mu\text{m}$, $8.9 \mu\text{m}$, and $13.4 \mu\text{m}$) between pump and probe pulse. The dashed vertical lines denote the minimum of the SAWs used to calculate the SAW velocity. (b) Microscope image of the electrical contacts above the MTJ nanopillar with two different laser heating positions (orange dots) and orientation of the MTJ's nominal easy axis as well as the externally applied in-plane magnetic field.	67

6.3	(a) Experimental geometry. A metal surface (yellow) is excited with an ultrashort optical pulse, generating different time-dependent strain tensor components ε_{ij} . The strain tensor components might interact with the magnetization of the magnetic layer, thereby inducing time-dependent magnetization dynamics. The dynamics can be described in the 1, 2, 3 coordinate system with the 3-direction being equal to the equilibrium magnetization \mathbf{m}_3 and the 2-direction lying in the plane of the magnetic layer. (b) Three most prominent acoustic waves and the corresponding strain tensor components and velocities. SP: strain pulses, SSLW: surface skimming longitudinal waves, SAW: surface acoustic waves.	69
6.4	Time-resolved voltage change across the MTJ for different excitation conditions and magnetic fields. (a) Optical excitation right above the MTJ nanopillar and (b) 10 μm away from the nanopillar. The black and red traces correspond to parallel (P, $H_{\text{ex}} = -150$ Oe) and antiparallel (AP, $H_{\text{ex}} = 120$ Oe) alignment of the MTJ for $\theta = 85^\circ$. In (b) the red curve is shifted by -0.2 mV for clarity.	71
6.5	(a) Optical excitation right above the MTJ and different magnetic field amplitudes for $\theta = 85^\circ$. All curves are shifted along the y axis for clarity. (b) Contour map of magnetization traces when the magnetic field is swept from the AP to the P state for $\theta = 85^\circ$ and a laser pulse energy of 15 nJ.	72
6.6	(a) Optical excitation right above the MTJ and a magnetic field amplitude of $H_{\text{ex}} = 120$ Oe but for different field angles θ . The black and blue curves are shifted along the y axis for clarity. (b) Spectrum of magnetization dynamics when the magnetic field is applied at different field angles θ with a laser pulse energy of 15 nJ.	73
6.7	(a) Contour map of magnetization traces when the magnetic field sweeps from AP to P state for $\theta = 85^\circ$ with laser pulse energy of 3 nJ. (b) Precession frequency versus applied magnetic field amplitude along the hard axis for two different optical excitation energies (black dots for 7.5 nJ and red dots for 15 nJ.	74
6.8	(a) and (b) show contour plots of the precession frequency spectra versus magnetic fields along the hard axis driven by 80-ps-long current pulses (electric STT) and SAWs. (c) Magnetization dynamics traces induced by electric STT at different magnetic field amplitudes for $\theta = 85^\circ$. All curves are shifted along the y axis for clarity. (d) Extracted precession frequency versus applied magnetic fields from (a) and (b).	75

6.9	(a) Simulated frequency of the free precession in the free layer versus applied magnetic field amplitude. (b) Upper part: Simulated equilibrium configuration of the magnetization component in the y direction in the FL for an applied magnetic field amplitude of 225 Oe. Lower part: Dynamical changes of the magnetization component in the y direction in the FL for an applied magnetic field amplitude of 225 Oe. The oscillations occur near the edges (blue region).	77
6.10	Schematic sketch of the experimental setup for coherent control of magnetization dynamics in the MTJ by two femtosecond laser pulse. The second laser beam is time delayed with the first beam, the maximum delay time up to 2 ns. The second laser beam can excite the sample at same positions and different positions with first laser beam.	78
6.11	Coherent control of magnetization dynamics using two time-delayed laser pulses B1 and B2 being focused onto the same position of the upper contact approximately 10 μm away from the MTJ stack. Upper plot: only pulse B1 (black) or B2 (blue), middle plot: constructive interference between B1 and B2, lower plot: destructive interference between B1 and B2. (b) Contour plot of the magnetization dynamics versus time delay between B1 and B2. The horizontal lines correspond to the two lower plots of (a).	79

Own publications

Journal publications

1. H. F. Yang, X. K. Hu, T. Boehnert, J. D. Costa, M. Tarequzzaman, R. Ferreira, S. Sievers, M. Bieler, and H.W. Schumacher, “Magnetic tunnel junction as a temperature sensor,” [submitted]
2. H. F. Yang, X. K. Hu, T. Boehnert, J. D. Costa, M. Tarequzzaman, R. Ferreira, S. Sievers, M. Bieler, and H.W. Schumacher, “Coherent control of phonon-induced magnetization dynamics in magnetic tunnel junctions,” *Applied Physics Letters*, vol. 113, no. 7, p. 072403, 2018.
3. H. F. Yang, X. K. Hu, N. Liebing, T. Boehnert, J. D. Costa, M. Tarequzzaman, R. Ferreira, S. Sievers, M. Bieler, and H. W. Schumacher, “Electrical measurement of absolute temperature and temperature transients in a buried nanostructure under ultrafast optical heating,” *Applied Physics Letters*, vol. 110, no. 23, p. 232403, 2017.

Conference presentations

4. H. F. Yang, X. K. Hu, N. Liebing, T. Boehnert, J. D. Costa, M. Tarequzzaman, R. Ferreira, S. Sievers, M. Bieler, and H. W. Schumacher, “Coherent control of acoustic-wave-induced magnetization dynamics in magnetic tunnel junctions,” in *CPEM 2018*, (Paris, Germany), 8-13 July 2018.
5. H. F. Yang, X. K. Hu, S. Sievers, M. Bieler, and H. W. Schumacher, “Phonon-pulse-induced magnetization dynamics in magnetic tunnel junctions,” in *DPG Fruehjahrstagung*, (Berlin, Germany), 11-16 March 2018
6. H. F. Yang, X. K. Hu, N. Liebing, T. Boehnert, J. D. Costa, M. Tarequzzaman, R. Ferreira, S. Sievers, M. Bieler, and H. W. Schumacher, “Electrical measurement of absolute temperature and temperature transients in a buried nanostructure under ultrafast optical heating,” in *Spin Caloritronics 8*, (Regensburg, Germany), 12-16 June 2017

7. H. F. Yang, X. K. Hu, N. Liebing, T. Boehnert, J. D. Costa, M. Tarequzzaman, R. Ferreira, S. Sievers, M. Bieler, and H. W. Schumacher, “Quantitative measurement of optically induced temperature transients in magnetic tunnel junctions,” in *Intermag 2017*, (Dublin, Ireland), 24-28 April 2017
8. H. F. Yang, X. K. Hu, N. Liebing, T. Boehnert, J. D. Costa, M. Tarequzzaman, R. Ferreira, S. Sievers, M. Bieler, and H. W. Schumacher, “Study of switching in MTJs in the presence of laser-induced temperature gradients,” in *Spin Caloritronics 7*, (Utrecht, Netherlands), 11-15 July 2016
9. H. F. Yang, X. K. Hu, N. Liebing, T. Boehnert, J. D. Costa, M. Tarequzzaman, R. Ferreira, S. Sievers, M. Bieler, and H. W. Schumacher, “Influence of laser heating on switching fields of synthetic antiferromagnets in magnetic tunnel junctions,” in *DPG-Frühjahrstagung*, (Regensburg, Germany), 6-11 March 2016
10. H. F. Yang, M. Bieler, and H. W. Schumacher, “Time domain thermalreflectance measurement of magnetic multilayers,” in *Spin Caloric Transport (SPP 1538)*, (Bad Honnef, Germany), 2-3 February 2015
11. H. F. Yang, M. Bieler, and H. W. Schumacher, “Time domain thermalreflectance measurement of magnetic multilayers,” in *DFG-priority program SPP1538 Spin-Caloric Transport*, (Irsee, Germany), 14-18 July 2014

Acknowledges

The thesis can not be finished without the support of other people. First I would like to express my sincere gratitude to PD. Dr. Hans W. Schumacher and Dr.-Ing. Mark Bieler for the opportunity to perform these studies, professional guidance and their confidences in me. PD. Dr. Hans W. Schumacher is an outstanding scientist having rigorous research attitude and always coming up new ideas, his encouragement accompanied with me through difficult times. Meanwhile, Dr.-Ing. Mark Bieler can always give me constructive advices after numerous discussions. I learnt a lot from him in and outside the lab. I am also grateful to Prof. Dr. Michael Oestreich for acting as my second supervisor of my dissertation and giving the opportunity to present and discuss my work.

I would like to thank Dr. Xiukun Hu for valuable discussions and suggestions. Her wisdom, her knowledge of the heat transport make my work smooth.

My sincere thanks goes to Dr. Christian B. Schmidt. He spent a lot of time in helping me build optical setup and tried to give me best solution of the problem.

I also would like to acknowledge Dr. Niklas Liebing and Dr. Sibylle Sievers for the guidance in the electric measurement and the combination of the electric heating setup and the optical setup. Without their helps, I can not finish my work.

I would like to thank the collaborators from the INL, Prof. Ricardo Ferreira, Dr. Tim Böhnert et al, who gave us nice MTJ samples. I would like to thank Dr. Felipe Garcia Sanchez from IRAM for the simulation.

I am lucky that I can work with wonderful people in the optical and nanomagnetism groups. Here I also want express sincere thanks to Dr. Heiko Fuser, Mr. Paul Struszewski, Mr. Alexander Fernández Scarioni, Ms. Manuela Gerken, Mr. Tobias Wenz and our secretaries Ms. Christina Becker and Ms. Katrin Volkmer.

Last but not least, I want to thank my wife Xiani Huang and my parents for the unlimited support. The experience of the study in Germany is the most valuable treasures in my life.

Curriculum vitae

Education

- 2014–now **PhD**, *Physikalisch-Technische Bundesanstalt, PTB*, Braunschweig, Germany, *Working group 2.52 - Femtosecond measurement technology and nanomagnetism*.
(Dr. Ing. M. Bieler, PD. Dr. H. W. Schumacher, Prof. Dr. M. Oestreich)
- 2010–2013 **Master of Engineering**, *China Jiliang University*, Hangzhou, China, *Working group – Materials Science and Engineering*.
(Dr. P. Y. Zhang, Prof. H. L. Ge)
- 2006–2010 **Bachelor of Science**, *China Jiliang University*, Hangzhou, China, *Applied Physics*.
- 2003–2006 **High School**, *Yinzhou High School*, Ningbo, China.
- 2000–2003 **Middle School**, *Fuming middle School*, Ningbo, China.

Experience

- 2013–2014 **Guest scientist**, *Physikalisch-Technische Bundesanstalt, PTB*, Braunschweig, Germany.
- 2010–2010 **Production helper**, *Permanent magnetic material*, Hangzhou, China.

Rewards

- 2013 **Excellent paper**, *China Jiliang University*, Hangzhou, China.
- 2009 **National Inspirational Scholarship**, *China Jiliang University*, Hangzhou, China.
- 2008 **First class award**, *China Jiliang University*, Hangzhou, China.
- 2007 **Second class award**, *China Jiliang University*, Hangzhou, China.